Using bottom pressure to quantify tidal form drag on a sloping headland

Sally J. Warner

A dissertation
submitted in partial fulfillment of the
requirements for the degree of

Doctor of Philosophy

University of Washington

2012

Reading Committee:

Parker MacCready, Chair

Matthew Alford

LuAnne Thompson

Program Authorized to Offer Degree:
Oceanography

University of Washington

Abstract

Using bottom pressure to quantify tidal form drag on a sloping headland

Sally J. Warner

Chair of the Supervisory Committee:
Professor Parker MacCready
Oceanography

Bottom pressure is used to quantify and understand form drag induced by tidal currents as they flow over and around Three Tree Point (TTP), a sloping headland in Puget Sound, WA that is typical of topography found in high latitude, coastal regions. By dividing the bottom pressure field into parts that are due to different physical processes, it can be determined how inertia, internal waves and eddies all contribute to form drag. In chapter 2, idealized numerical models of vertical-walled headlands are combined with theory to show how the oscillatory nature of the flow can increase the magnitude of the form drag, but cannot increase the magnitude of the tidally averaged work done on the flow. In chapter 3, an array of seafloor pressure sensors is deployed across the topography to directly measure total form drag for the first time in the ocean. It is found that form drag is much larger than frictional drag, and that a linear wave drag law is a better parameterization of form drag than a bluff body drag law. The form drag is estimated to convert 0.2 W m^{-2} of tidally averaged power away from the barotropic tides. In chapter 4, a numerical model of TTP is used to investigate the tilted eddies and internal lee waves that are generated at this site. It is found that the sea surface and isopycnal perturbations tend to counteract each other within the eddy, but work in tandem in the internal lee wave. Therefore, despite the large sea surface depression in the eddy, the eddies and the internal lee waves remove the same amount of energy from the barotropic tides. Through this thesis, it is shown that form drag — not frictional drag — is the dominant mechanism for removing energy from the tides at TTP. Steps are made toward betters parameterizations of drag that may be implemented into larger scale models that do not resolve the scales important to form drag.

TABLE OF CONTENTS

Page

List of Figures iv

Chapter 1: Introduction 1
  1.1 Broader context 1
  1.2 Overview of thesis 5

Chapter 2: Dissecting the pressure field in tidal flow past a headland: When is form drag "real?" 11
  2.1 Introduction 11
  2.2 Theory 15
    2.2.1 An introductory example: Potential flow around a cylinder . . 15
    2.2.2 Potential flow around a headland: The inertial drag 18
    2.2.3 Total and residual form drags 22
  2.3 Methods 23
    2.3.1 Specifics of the ROMS model 23
    2.3.2 Nondimensional parameters and model runs 26
  2.4 Results 28
    2.4.1 Time series of inertial and separation drags 28
    2.4.2 Inertial drag: Amplitude 30
    2.4.3 Separation drag: Amplitude 33
    2.4.4 Separation drag: Phase and power 35
    2.4.5 Description of flow through a tidal cycle: What mechanisms create the separation drag and its phase? 38
  2.5 Conclusion 41

Chapter 3: Measurement of tidal form drag using seafloor pressure sensors . 42
- 3.1 Introduction . . . 42
- 3.2 Experiment details . . . 44
- 3.3 Bottom pressure anomalies . . . 47
  - 3.3.1 Calculating bottom pressure anomalies from Ppods . . . 47
  - 3.3.2 Fluctuations of bottom pressure anomalies . . . 52
- 3.4 Form drag from bottom pressure . . . 56
  - 3.4.1 Total form drag . . . 56
  - 3.4.2 Form drag from the shallow water momentum equation . . . 58
- 3.5 Bottom pressure and form drag from potential density . . . 60
  - 3.5.1 Internal lee waves . . . 60
  - 3.5.2 Form drag from potential density . . . 63
- 3.6 Turbulent kinetic energy dissipation rate . . . 66
- 3.7 Velocity surveys . . . 66
- 3.8 Inertial pressure and form drag . . . 70
- 3.9 Comparisons and parameterizations . . . 73
- 3.10 Conclusion . . . 78
- 3.11 Appendix A: Error analysis . . . 80
  - 3.11.1 Ppod pressure errors . . . 80
  - 3.11.2 Three form drag integration methods . . . 81

Chapter 4: The dynamics of pressure and form drag on a sloping headland: Internal waves versus eddies . . . 85
- 4.1 Introduction . . . 86
- 4.2 Methods . . . 88
  - 4.2.1 Model setup . . . 88
  - 4.2.2 Pressure decomposition . . . 91
  - 4.2.3 Calculating form drag . . . 93
- 4.3 Dissecting the pressure field: Physical mechanisms that create form drag . . . 94
  - 4.3.1 Eddies . . . 94
  - 4.3.2 Internal waves . . . 101

4.4 Implications for form drag and power 105
4.5 Conclusions 109
4.6 Appendix A: Model compared to observations 112
    4.6.1 Density 112
    4.6.2 Tidal currents 112
    4.6.3 Bottom pressure anomalies 113
    4.6.4 Form drag and power 115
4.7 Appendix B: Ppod abundance 117

Chapter 5: Conclusions 119

Bibliography 121

LIST OF FIGURES

Figure Number Page

1.1 Form drag vs. frictional drag 2

2.1 Three Tree Point schematic 14
2.2 Potential flow sea surface height 20
2.3 Tidal velocity, form drag, power and cumulative power 29
2.4 Amplitudes of inertial drag and separation drag 31
2.5 Real vs. theoretical inertial drag 32
2.6 Separation drag amplitude, phase and power 34
2.7 Histogram of drag coefficients 36
2.8 Sea surface height and vorticity throughout a tidal cycle 39

3.1 Location of field experiment 45
3.2 Conditions during the field experiment 46
3.3 Steps for processing Ppod pressure 51
3.4 Bottom pressure anomalies along the ridge transect 53
3.5 Bottom pressure anomalies from the headland transect 54
3.6 Pressure error 55
3.7 Time series of total form drag 57
3.8 Time series of bulk drag 59
3.9 Potential density and bottom pressure anomalies through one tidal cycle 62
3.10 Time series of internal form drag 65
3.11 Turbulent kinetic energy dissipation rate through one tidal cycle . . . 67
3.12 Time series of integrated turbulent dissipation 68
3.13 Velocity at ebb, slack and flood tides 69
3.14 Time series of inertial form drag 72
3.15 Form drag and power versus velocity 76

3.16 Average power 77
3.17 Piecewise-integration of form drag 82
3.18 Form drag calculated in 3 ways 83

4.1 Model domain and topography 90
4.2 Bottom pressure anomalies during flood tide 95
4.3 Bottom pressure anomalies during slack tide 96
4.4 Position of surface and bottom of a flood tide eddy 97
4.5 Flood tide eddy dynamics 98
4.6 Density and pressure along 4 transects and flood and slack tides . . . 102
4.7 Density and pressure along section 1 during flood tide 103
4.8 Internal, external and dynamic form drag and power 106
4.9 Average internal, external and dynamic power 109
4.10 Model vs. observed CTD 113
4.11 Model vs. observed bottom pressure anomalies 114
4.12 Model vs. observed form drag and power 116
4.13 How many Ppods needed to measure form drag? 118

ACKNOWLEDGMENTS

First and foremost, I would like to express my sincere appreciation to my advisor Parker MacCready. He has an endless supply of patience and knowledge. There have been countless times where I have gotten frustrated and flustered with my research, and Parker is always able to find my mistakes and set me on the right track. I would always walk out of meetings with him feeling confident and excited about my work. I have really enjoyed grad school and feel so grateful to Parker for making research fun, exciting, and rewarding.

I have received a lot of very useful advice and guidance from my committee: LuAnne Thompson, Matthew Alford, Andrea Ogston and Alberto Aliseda.

Jim Moum and Jonathan Nash have been excellent collaborators. They made the observational portion of this thesis possible and have helped me to become a better scientist.

David Darr has been instrumental in getting my ROMS models successfully running. In addition, the MUG group has been a great source of modeling advice and support. David Sutherland in particular helped with getting the Three Tree Point model nested within the MoSSea Model.

Many people played instrumental roles in making the field work successful in October 2010: Raymond Kreth, Zen Kurokawa, Jules Moritz, Aurélie Moulin, Liam Neeley-Brown, Mike Neeley-Brown, Cecilia Peralta-Ferriz, Alexander Perlin, Jamie Shutta, Uwe Stöber, David Sutherland, and the crews of the

R/V Barnes and R/V Wecoma. I would also like to thank Aurélie Moulin for the work that she did in the first step of processing of the Chameleon and Ppod data.

I would like to thank my officemates Tom, Nick and Noel for listening to countless practice talks, providing company during late nights at the office, and always being up for a mid-afternoon chat or an after-work beer. Cecilia, Alison, Sam, Lissa and Amy have also been a great source of support for all thing physical oceanography and beyond.

Finally, a huge thank you to my family who have always provided me with unconditional support and love.

DEDICATION

To Mr. Alan Levin, my 10th grade physics teacher, from whom I learned $F = ma$ and began a life-long love of physics.

Chapter 1

INTRODUCTION

1.1 Broader context

Primarily, this thesis aims to figure out how much energy is removed from tidal currents as they flow over and around undersea topography. This is an important question in oceanography, because it is unknown how and where the 3.5 TW of tidal power that is put into the ocean by the sun and moon is dissipated (Munk and Wunsch, 1998; Wunsch and Ferrari, 2004). We do not suggest that we have solved the ocean energy budget. Instead we have taken steps to understand the dynamics and energy conversion at one particular headland that is typical of topography found in high latitude, coastal settings. Even though the energy loss at this headland is only a tiny fraction of the total ocean energy budget, the physical processes that occur here — generation of internal waves and eddies — are common in the ocean.

The tool that we use to estimate tidal energy loss is form drag (also known as pressure drag). Form drag occurs when a fluid, such as air or water, flows past a three-dimensional object, which generates a pressure difference between the upstream and downstream sides (Kundu and Cohen, 2004). Form drag differs from frictional drag because it arises from pressure forces that act normal to the object's surface, as opposed to frictional drag which arises from shear forces that act tangentially to the object's surface (Fig. 1.1). In cases where the fluid separates from an object creating a lee wake, the form drag is most likely much larger than the frictional drag (Fox and

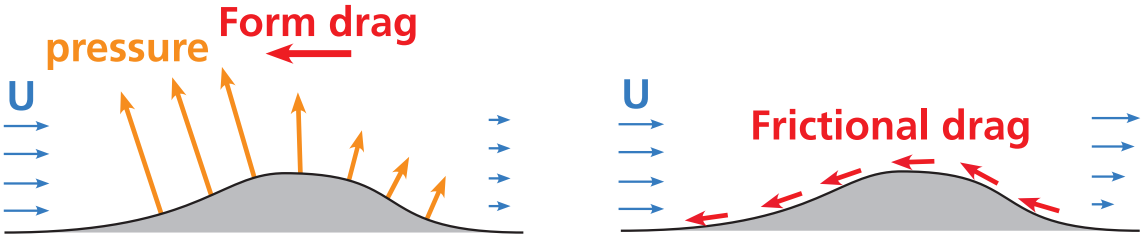

Figure 1.1: (Left) form drag is created by pressure differences that arise as fluid flows over an object. An integral of the pressure across the topography gives the form drag. It works to remove energy and momentum from the background flow. (Right) frictional drag is due to the tangential forces that act on the fluid in the bottom boundary layer.

McDonald, 1998). In the atmosphere, 50% of the total drag can be attributed each to form drag and to frictional drag (Baines, 1995), and in isolated locations in the ocean, form drag has been found to be as much as 50 times larger than the frictional drag (Edwards et al., 2004). Sometimes increasing the frictional drag can even drastically reduce the form drag, which is why golf balls with dimples fly twice as far as those without (Fox and McDonald, 1998).

Form drag can be calculated by taking an integral of the pressure, p, over the surface of the object:

$$D_{form} = \int_{\text{surface}} p\, dA \tag{1.1}$$

where A is the wetted area of the object's surface. Form drag is extremely useful because not only does it tell us how much force is exerted between a fluid and an object, but the product of form drag and velocity is power, so we can calculate how much energy is removed from the flow over time. In the ocean, if the form drag is known, the energy converted from the barotropic tides can be calculated.

Prior to this thesis, form drag had not been directly measured in the ocean using bottom pressure sensors. It had been estimated using other techniques such as determining pressure from vertical isopycnal (Edwards et al., 2004; Moum and Nash, 2000) or sea surface (McCabe et al., 2006) displacements. However, these only capture part of the pressure signal that creates form drag. Beyond the ocean, form drag due to air currents flowing over mountain ranges has been directly measured in the atmosphere (Bougeault et al., 1993). In chapter 3, we detail an experiment where an array of seafloor pressure sensors was used to directly measure form drag and estimate the energy conversion from the barotropic tides.

An eventual goal of the work presented here is to find better drag parameterizations for tide/topography interactions which can be implemented into larger scale numerical models that cannot resolve processes important for form drag. Engineers have experimentally calculated drag coefficients (C_D) for almost any object (Hoerner, 1965). Therefore, instead of measuring pressure and calculating form drag from Eq. 1.1, it can be estimated with the simpler bluff body drag law:

$$D_{BB} = \frac{1}{2}\rho_0 C_D A_p U^2 \tag{1.2}$$

where ρ_0 and U are the density and velocity of the fluid, respectively, and A_p is the projected frontal area of the object. Typical drag coefficients are $O(1)$. In oceanography, however, drag coefficients are generally unknown. Currently, crude form drag parameterizations — if any — are included in large scale numerical models (Donner and Large, 2008), and our lack of knowledge of the net effect of bottom drag is a key remaining issue preventing the closure of the ocean's energy budget (Wunsch and Ferrari, 2004). On the occasion that form drag parameterizations have been used in models, there has been a marked improvement in performance (Jayne and St. Laurent, 2001). In atmospheric science, various mountain drag parameterizations have been developed (Long, 1955; Wurtele et al., 1996; Garner, 2005), and their inclusion has improved the skill of weather models (Lott and Miller, 1997; Wood et al., 2001; Kim et al., 2003).

Determining drag coefficients in the ocean is more complicated than in most engineering applications because the ocean is stratified and therefore internal waves, in addition to eddies, can be generated as tidal currents flow over topography. Internal wave generation is a complex problem that depends not just on the magnitude of the currents (U) and the shape of the topography (L = along-flow e-folding length, W = across-flow width, and h = height) — which are the important parameters in unstratified cases — but also on the stratification (N), tidal frequency (ω), Coriolis frequency (f), and water depth (H). Garrett and Kunze (2007) define a non-dimensional parameter space based on these values that includes the ratio of tidal excursion distance to topographic length ($U/\omega L$), the ratio of topographic height to water depth (h/H), the ratio of topographic steepness to wave ray steepness ($\epsilon = h/L(\frac{\omega^2-f^2}{N^2-\omega^2})^{1/2}$), and the likeliness of nonlinearity blocking (Nh/U). Internal waves have been explored extensively in the oceanographic context: Baines (1995) details internal wave generation in steady flow cases, Vlasenko et al. (2005) explain many different types of internal tidal waves including nonlinear ones, and Garrett and Kunze (2007) review many cases of internal wave generation by tides in the deep ocean. In this thesis, rather than go in depth into the many different internal wave theories and wave drag parameterizations, we instead measure form drag using Eq. 1.1, and compare it to a linear wave drag law for steady flow over a linear, subcritical ridge (Baines, 1995):

$$D_{wave} = \frac{\pi}{8}\rho_0 N W h^2 U. \tag{1.3}$$

Overall, our goal is to deepen the understanding of form drag in the ocean. We directly measure form drag using seafloor pressure sensors and estimate how much energy is taken out of the barotropic tides as they flow over rough topography. We are also interested in the physical mechanisms that generate form drag. Using numerical models, we dissect the bottom pressure fields into various components to see the individual inputs to form drag of internal waves, eddies, and tidal acceleration. While we have not answered the question of where the 3.5 TW of tidal power eventually ends up in the ocean, we have provided a new method for determining energy conversion from tidal currents and quantified the physical mechanisms that create form drag at one typical headland.

1.2 Overview of thesis

The work in this thesis is based at Three Tree Point (TTP), a sloping headland in Puget Sound, WA, which has been studied extensively in the past. MacCready and Pawlak (2001) developed a theory for form drag generated by steady, stratified, non-rotating flow around ridges on a sloping side wall. Lab experiments were performed on oscillatory flow past similar topography by Pawlak and MacCready (2002). Observational studies were then performed at TTP. Pawlak et al. (2003) described the time evolution of the eddy, Edwards et al. (2004) described the internal wave structure and estimated the form drag due to these waves, McCabe et al. (2006) mapped out the eddies and estimated their contribution to form drag, and finally, Canals et al. (2009) described the isopycnal structure of the tilted vortices. These studies have given much insight into the dynamics and form drag at TTP. However, important questions remain. First, according to the model used by Edwards et al. (2004), it was found that a bluff body drag law (Eq. 1.2) needed a drag coefficient (C_D) of 8.7 to match the integrated form drag (Eq. 1.1). This is much larger than expected. What creates the extra form drag at TTP? Second, can the form drag at TTP be measured with bottom pressure sensors? If so, how big is it and can it be parameterized? Finally, do internal lee waves or eddies create more form drag at TTP?

Overall, the work presented in this thesis involves dividing the pressure field into parts that are due to different physical processes and determining how each one creates form drag. There are three parts of the pressure field that contribute to form drag:

the inertial, external and internal pressures. The inertial pressure is associated with the acceleration of the tides. It can create form drag but cannot due tidally averaged work on the flow (Warner and MacCready, 2009). The external pressure is due to local perturbations of the sea surface such as the depression in the center of eddies observed by McCabe et al. (2006). The internal pressure is due to local perturbations of isopycnals such as those created by internal waves (Edwards et al., 2004). This is not to say that eddies only affect the external pressure and internal waves only affect the internal pressure. Both physical processes can affect both isopycnals and the sea surface, but they do it in very different ways as is detailed in chapter 4. The sum of the internal and external pressures is the dynamic pressure (sometimes referred to as the "residual pressure" in chapter 2). They all correspond to similarly named parts of the form drag: internal form drag, external form drag, dynamic form drag, etc. In chapter 2, the theory behind the inertial pressure is developed and inertial pressure is separated from the dynamic pressure in a model of vertical-walled headlands. In chapter 3, the total and internal pressures are both directly measured at TTP using seafloor pressure sensors and a free-falling CTD, respectively. In chapter 4, a model of the TTP region of Puget Sound is used to dissect the total pressure field into all of its constituents in order to see how the internal waves and eddies are generated and create form drag.

The pressure decomposition used here is most appropriate for topography that generates both internal waves and eddies. This differs from other methods of decomposing pressure. Ertel potential vorticity theory decomposes the pressure into a barotropic part which has $p = p(\rho)$ and a baroclinic part where gradients of density and pressure are not parallel (Vallis, 2006). For internal waves, Kunze et al. (2002) describes a method of dividing the pressure into barotropic and baroclinic parts by calculating vertical isopycnal displacements. The baroclinic part includes all of the pressure fluctuations due to internal waves and has a zero vertical mean. Our use of “internal” and “external” pressures throughout this thesis should not be confused with baroclinic and barotropic pressures.

Chapter 2 describes how form drag in oscillatory flow situations can be much larger than for steady flow of the same magnitude. The theory arose from looking at engineering studies of wave flow around offshore structures. As Dean and Dalrymple (1984) describe:

> “Watching a wave impinge on a vertical pile, the complexity of the problem becomes immediately obvious. As the waves crest approaches the pile, a bow wave forms and run-up occurs on the front of the pile, while a wake develops at the rear. . . . As the wave crest passes and the trough reaches the pile, the flow field reverses and the previously formed wake may wash back past the pile as a new wake is formed.”

Therefore, there are two components of force exerted by the wave on the piling. The first is a steady flow term that is proportional to U^2 and is responsible for the wake in the lee. The second part of the force is due to inertia as the flow field reverses. It is proportional to $\frac{\partial U}{\partial t}$ and arises even in the absence of friction. Morison et al. (1950) show that the total wave force on a piling is therefore equal to the sum of the drag and inertia forces. In chapter 2, we show that the same theory holds for much larger cases, specifically when tidal waves flows past topography such as headlands. It is especially relevant when the tidal excursion distance is nearly equal to the topographic length.

However, our goal as oceanographers differs from that of engineers. They want to know how much force is exerted by waves on pilings so their structure does not collapse. As oceanographers, we care much more about how much energy is removed from the overlying flow by form drag. Since, the part of the drag that is due to the inertial force is in perfect quadrature with the velocity, it cannot do tidally averaged work on the flow. Therefore, in oscillatory flow situations around headlands, total form drag may be measured to be much larger than predicted by a bluff body drag, however, once the inertial drag is removed, the remaining drag is well-parameterized by a bluff body drag.

Chapter 3 details the results of an observational study at TTP where an array of seafloor pressure sensors was deployed across the topography to measure form drag. This is the first experiment to measure form drag in the ocean using seafloor pressure sensors. In addition to pressure, density and microstructure were also measured along a transect that crossed the topography. We show that the form drag is significantly larger than frictional drag over an equivalent area of flat bottom. Furthermore, it is found that a linear wave drag law (Eq. 1.3) does a better job of parameterizing the form drag than a bluff body drag law (Eq. 1.2). Along the ridge transect — where internal waves dominate the dynamics — we find that the internal drag makes up 80 percent of the dynamic drag. There are also elevated levels of turbulent kinetic energy dissipation within the topographic lee waves that reach magnitudes of 10^{-5} W kg^{-1} during maximum flood tide. This is much larger than what is found in the open ocean (Waterhouse et al., 2012), but an order of magnitude smaller than measured in the lee waves at Knight Inlet (Klymak and Gregg, 2004). The form drag is estimated to convert 0.2 W m^{-2} of tidally averaged power away from the barotropic tides, which is similar to the tidal conversion rates found by Kang and Fringer (2012) in Monterery Bay Canyon.

In chapter 4, a numerical model of TTP is used to further understand the dynamics of internal waves and eddies. The bottom pressure field is divided allowing the internal, external and dynamic pressures to be analyzed separately. During flood tide, a tilted eddy is generated. The horizontal distance between the top and bottom of the eddy is as big as three eddy diameters. Centripetal force causes the sea surface to depress at the eddy center. In the top half of the eddy, isopycnals undergo baroclinic adjustment and are raised to counteract the sea surface depression. Here, the internal and external pressures tend to counteract each other. In the bottom half of the eddy, the sea surface depression does not affect the pressure so the local centripetal force causes isopycnals to be lowered. Internal waves are also generated at TTP. These lead to downward displacements of isopycnals, but relatively small perturbations of the sea surface. Overall, even though the magnitude of the internal and external pressure perturbations from the eddy are much larger than pressure perturbations from the internal wave, the dynamic pressure for both are nearly equal. Therefore, the internal waves and the eddies at TTP both do similar amounts of work on the flow.

The work presented in this thesis contributes to our understanding of topographic form drag and tidal energy conversion. We establish that in oscillatory flow situations, the form drag may be much larger than predicted by a bluff body drag law, however, a large part of that drag may simply be due to the inertia and does not remove energy from the tides. We directly measure form drag using seafloor pressure sensors for the first time in the ocean, and develop a method that may become more widely used in oceanography to quantify form drag across topography. We show that due to the presence of both internal waves and eddies, the dynamic form drag at TTP is larger than both frictional drag and bluff body drag. We analyze the internal and external parts of the pressure field to demonstrate that eddies and internal waves both do similar amounts of work on the flow.

The three chapters included in this thesis were originally written as separate articles that have been published in or submitted to peer-reviewed journals. Therefore, there is some repetition between the chapters, especially in the introductions and theory sections. Chapter 2 is identical to Warner and MacCready (2009). Chapter 3 and 4 are still "in preparation." Chapter 3 is written with coauthors P. MacCready, J. N. Moum and J. D. Nash and chapter 4 is written with P. MacCready.

Chapter 2

DISSECTING THE PRESSURE FIELD IN TIDAL FLOW PAST A HEADLAND: WHEN IS FORM DRAG "REAL?"

In the few previous measurements of topographic form drag in the ocean, drag that is much larger than a typical bluff body drag estimate has been consistently found. In this work, theory combined with a numerical model of tidal flow around a headland in a channel gives insight into the mechanisms that create form drag in oscillating flow situations. The total form drag is divided into two parts: the inertial drag which is derived from a local potential flow solution, and the separation drag which accounts for flow features such as eddies. The inertial drag can have a large magnitude, yet it cannot do work on the flow because its phase is in quadrature with the velocity. The separation drag has a magnitude that is nearly equal to the bluff body drag and accounts for all of the energy removed from the flow by the topography. In addition, the dependence of the form drag on the tidal excursion distance and the aspect ratio of the headlands was determined with a series of numerical experiments. This theory explains why form drag can be so large in the ocean, and provides a method for separating the pressure field into the parts that can and cannot extract energy from the flow.

2.1 Introduction

Form drag is a force that results from pressure differences across obstacles in a flow field. In the ocean, form drag has been measured in a coastal setting on a ridge with hydraulically controlled flow (Moum and Nash, 2000; Nash and Moum, 2001), and in an estuarine setting on a headland with sloping side walls subjected to tidal currents (Edwards et al., 2004; McCabe et al., 2006). In these studies, the form drag was found to be at least twice (Nash and Moum, 2001) and up to 50 times (Edwards et al., 2004) larger than the frictional drag. The form drag was also assumed to be responsible for the creation of flow features such as internal lee waves and eddies and to contribute to increased mixing rates observed near these sites. The importance of form drag in the ocean is not just confined to coastal regions; on a global scale, the performance of a hydrodynamic model of the ocean's tides was improved by using a drag parameterization that accounted for the creation of internal waves over rough topography in the deep ocean (Jayne and St. Laurent, 2001). On much smaller scales, form drag due to surface waves has been shown to be a dominant force on benthic organisms in shallow regions (Lowe et al., 2005).

The motivation for this study comes primarily from observations of the tidal flow near Three Tree Point (TTP) in Puget Sound, Washington by Edwards et al. (2004) and McCabe et al. (2006). The Puget Sound is a tidal estuary with an average depth of 200 m and a width of 5 km near TTP. From above, TTP looks like a sharp triangular headland, about 1 km wide (across channel) and 1 km long (along channel) at its base. Beneath the surface, it is situated on a sloping side wall, and hence, behaves both like a headland that requires water to travel around it and a ridge that requires water to travel over it, as depicted in Fig. 2.1. Eddies and internal waves are both observed on the downstream side of the topography. A numerical model of the site (Edwards et al., 2004) matched the observations reasonably well. The average amplitude of the total form drag in the model, integrated over a 10 km segment of the tidal channel, was about 2×10^7 N (Edwards et al., 2004, Fig. 16). To get a better sense of the size of this measurement, we can compare it to a theoretical estimate of the steady bluff body drag,

$$D_{BB} = \frac{1}{2}\rho_0 C_D S U_0^2 \tag{2.1}$$

assuming the following values from Edwards et al. (2004, Figs. 4 and 9): the average density, $\rho_0 = 1023.5$ kg m^{-3}, the projected frontal area of the topography, $S = 200$ m $\times 1000$ m, and the amplitude of the tidal velocity, $U_0 = 0.15$ m s^{-1}. We find that in order to get the bluff body drag to match the measured drag, a drag coefficient, C_D, of 8.7 must be used, where a typical value is $O(1)$. The largest drag coefficient found in steady flow situations with Reynolds numbers greater than 10^3 is 2.3 which comes from flow around a concave C-shaped object (Hoerner, 1965). In a theoretical and numerical model study, MacCready and Pawlak (2001) found that drag coefficients for stratified, steady flow over ridges on sloping side walls were between 1 and 1.2. What creates the increased form drag at TTP? The results of this research suggest that the increased form drag is a result of the oscillating nature of the flow.

In order to simplify the problem of oscillating flow over TTP-like topography, we decided to look at eddy-generating headlands and internal wave-generating ridges separately (Fig. 2.1). This paper will focus just on the results from the headland study. The dynamics of eddy formation behind headlands, capes and islands have been studied in the laboratory (Boyer and Tao, 1987; Klinger, 1994; Cenedese and Whitehead, 1999), in numerical models (Black and Gay, 1987; Signell and Geyer, 1991), and in field experiments (Wolanski et al., 1984; Geyer, 1993). In this work, a numerical model was used to explore headlands of different sizes and shapes in a range of flow situations with the goal of isolating the mechanisms that create form drag. The total form drag was broken up into two parts: the inertial drag and the separation drag. The inertial drag is based on theoretical calculations of potential flow and the separation drag is the residual that remains after the inertial drag is subtracted from the total drag. It accounts for flow features such as eddies. In this

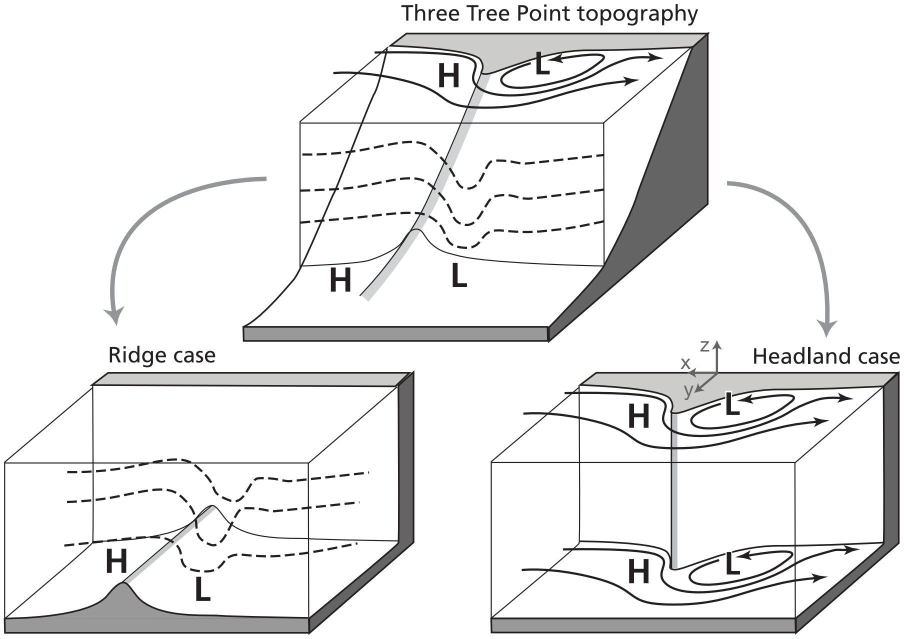

Figure 2.1: The diagram at the top is a schematic of the topography at Three Tree Point. It is shaped like a ridge on a sloping side wall and therefore generates both internal waves and eddies. In order to simplify the problem and more easily identify flow mechanisms contributing to form drag, the system was split into two cases: the internal wave generating ridge case and the eddy generating headland case. In this paper, only the headland case is discussed. The coordinate axes shown on the headland diagram align with the axes in the numerical model.

paper, we will first develop a theoretical basis for the inertial drag by looking at the case of oscillating potential flow around a cylinder (section 2.2.1). We will then expand this theory to include the case of a headland in a channel (section 2.2.2). The numerical model is explained in section 2.3. In section 2.4, the relative amounts of inertial and separation drag from each model run are examined and compared to the bluff body drag. The abundance and strength of flow mechanisms that make up the separation drag are explained in the latter part of section 2.4. The findings of this study are summarized in section 2.5.

2.2 Theory

2.2.1 An introductory example: Potential flow around a cylinder

A lot of insight into tidal flow around headlands can be gained by looking at oscillating flow around circular cylinders. This is not a new problem. Engineers were motivated to study the details of this flow field because they wanted to calculate the hydrodynamic forces due to waves on off-shore cylindrical structures (Faltinsen, 1990). An analytical theory for oscillating flow around cylinders at low Reynolds numbers was developed by Wang (1968). Laboratory (Bearman et al., 1985; Obasaju et al., 1988) and numerical (Justesen, 1991) studies have been conducted with regard to this problem over a range of Keulegan-Carpenter (the ratio of drag forces to inertia) and Reynolds numbers. However, when it comes to flow around topography in the ocean, the Reynolds number can be of order 10^9 because the length scales are so large. None of these studies explored flow at such high Reynolds numbers except Jones et al. (1979) who studied flow around oscillating cylinders at high Mach numbers. An important difference between the motivation of these studies and the research discussed in this paper should be noted. Engineers care about the total drag force exerted on their structures, whereas in an oceanographic context, we are more interested in the energy that topography can remove from the tidal currents. The different objective has led us to focus on different aspects of the problem.

To begin our theoretical analysis, we start by looking at the 2-dimensional, inviscid, irrotational potential flow around a cylinder as detailed by Lamb (1945, Chapter 4, section 68). This approach of looking at the potential flow solution as a way to gain insight into the different parts of the form drag is similar to that explained by Dean and Dalrymple (1984, Chapter 8). The velocity potential, ϕ, for a cylinder is defined as,

$$\phi = U(t)\left(r + \frac{a^2}{r}\right) cos\theta \tag{2.2}$$

Here, $U(t)$ is the free-stream velocity, a is the radius of the cylinder, and r and θ are the polar coordinates. By definition, the gradient of the velocity potential is equal to the velocity around the cylinder, $\nabla\phi = \mathbf{u} = (u, v)$. In order to calculate the pressure, p, on the surface of the cylinder, start with the inviscid, Boussinesq, irrotational momentum equation,

$$\frac{\partial \mathbf{u}}{\partial t} + \nabla \frac{1}{2}\mathbf{u}\cdot\mathbf{u} = -\frac{1}{\rho_0}\nabla p. \tag{2.3}$$

Replace $\frac{\partial \mathbf{u}}{\partial t}$ with $\nabla\frac{\partial \phi}{\partial t}$ and solve for the pressure,

$$\nabla\left(\rho_0\frac{\partial \phi}{\partial t} + \frac{1}{2}\rho_0\mathbf{u}\cdot\mathbf{u} + p\right) = 0 \tag{2.4}$$

$$p = C(t) - \frac{1}{2}\rho_0\mathbf{u}\cdot\mathbf{u} - \rho_0\frac{\partial \phi}{\partial t}. \tag{2.5}$$

This is the unsteady irrotational Bernoulli's equation, and $C(t)$ appears as a time dependent constant of integration. Making use of the relations $\frac{\partial \phi}{\partial t}\Big|_{r=a} = U_t\, 2a\, cos\theta$ and $\mathbf{u}\cdot\mathbf{u}\Big|_{r=a} = 4U^2 sin^2\theta$, which can be calculated from Eq. 2.2, we can solve for the pressure on the surface of the cylinder,

$$p\Big|_{r=a} = C(t) - 2\rho_0\, U^2 sin^2\theta - \rho_0\, U_t\, 2a\, cos\theta. \tag{2.6}$$

The first term in Eq. 2.6 represents a constant pressure offset around the whole cylinder that is a function of time. The middle term defines low pressure regions on the sides of the cylinder that lie tangent to the background velocity. Its magnitude is greatest when the velocity is maximum. The third term represents a horizontal pressure gradient across the cylinder. This gradient is strongest when the velocity is zero and the acceleration, U_t, is maximum.

The drag force per unit length of cylinder δz, $D/\delta z$, resulting from this pressure field can be calculated by integrating the pressure 2.6 over the surface of the cylinder,

$$\frac{D}{\delta z} = \int_0^{2\pi} -p\Big|_{r=a} cos\theta \, a \, d\theta \tag{2.7}$$

$$\frac{D}{\delta z} = \int_0^{2\pi} - \left[C(t) - 2\rho_0 U^2 sin^2\theta - \rho_0 U_t \, 2a \, cos\theta\right] \, cos\theta \, a \, d\theta \tag{2.8}$$

$$\frac{D}{\delta z} = 2\pi a^2 \rho_0 U_t. \tag{2.9}$$

It is interesting to compare the size of this drag force (Eq. 2.9) to the bluff body drag (Eq. 2.1). To do this, it is assumed that in Eq. 2.1 the drag coefficient is 1 and the projected frontal area of the cylinder is $2a\delta z$. Taking the flow to be oscillatory with the form,

$$U(t) = U_0 \, sin \, \omega t \tag{2.10}$$

where ω is the frequency of oscillation, it can then be assumed that U_t scales like ωU_0. Hence, the ratio of this drag force to the bluff body drag is,

$$\frac{D/\delta z}{D_{BB}/\delta z} = \frac{2\pi a^2 \rho_0 U_t}{\frac{1}{2}\rho_0 C_D (2a) U_0^2} = \frac{2\pi a \omega}{U_0} = \frac{4\pi a}{L_T} \tag{2.11}$$

where $L_T = 2U_0/\omega$ is the tidal excursion distance and we have assumed $C_D = 1$. For a short tidal excursion distance this ratio is large, so the drag associated with the potential flow is expected to be much larger than the bluff body drag. When the tidal excursion distance is long, the drag from the potential flow will be small compared the bluff body drag. This makes sense because a long tidal excursion distance is approaching the steady limit, and by definition steady potential flow does not exert a force on a body (Kundu and Cohen, 2004, p. 166-167).

This potential flow example can be taken one step farther by calculating the work that the drag can do on the flow. The work, W, is the time integral of the power, P, over an oscillation period, and the power is the product of drag (Eq. 2.9) and the velocity (Eq. 2.10),

$$W = \int_0^{\frac{2\pi}{\omega}} P\,dt = \int_0^{\frac{2\pi}{\omega}} D\,U\,dt = 2\pi a^2 \rho_0 \delta z U_0^2 \omega \int_0^{\frac{2\pi}{\omega}} sin(\omega t)\,cos(\omega t)\,dt = 0. \tag{2.12}$$

Hence, the drag associated with potential flow around a cylinder cannot do work on the flow. Although this is a seemingly obvious result that has been shown in places like Batchelor (1967, p. 355) and Dean and Dalrymple (1984), using the same theoretical basis for flow around a headland will help us dissect the pressure field into the parts that can and cannot do work on the flow.

2.2.2 Potential flow around a headland: The inertial drag

The framework that was developed in section 2.2.1 will now be applied to the case of potential flow around a headland in a channel. By doing this, the part of the pressure field that cannot do work on the flow can be isolated. This will be referred to as the potential flow pressure field and the corresponding form drag will be called the inertial drag.

The first step to calculating the inertial drag, is to find the two-dimensional, incompressible, irrotational streamfunction around a headland in a channel. Conveniently, the streamfunction, ψ, for potential flow satisfies the Laplace equation,

$$\nabla^2 \psi = \frac{\partial^2 \psi}{\partial^2 x} + \frac{\partial^2 \psi}{\partial^2 y} = 0. \tag{2.13}$$

The boundary conditions are defined such that the velocity far from the headland is equal to the free stream velocity from Eq. 2.10, $\frac{\partial \psi}{\partial y} = U(t)$, and the velocity normal to a solid surface is zero, $\frac{\partial \psi}{\partial s} = 0$, where s defines the along-stream coordinates of the boundary. Eq. 2.13 can be solved numerically using the method described by Kundu and Cohen (2004, p. 182-187). A typical streamfunction around a headland looks like the black contours in the left-hand panels of Fig. 2.2. Throughout the tidal cycle, only the magnitude of the the streamfunction changes, not the shape.

Similar to the case of flow around a cylinder, to get the pressure field, integrate the inviscid, irrotational, Boussinesq momentum Eq. 2.3 along streamlines from a point, $\mathbf{x_A} = (x_0, y_A)$, at the entrance of the domain to any point on the same streamline within the domain, $\mathbf{x_B} = (x_B, y_B)$,

$$\int_{\mathbf{x_A}}^{\mathbf{x_B}} \frac{\partial u_s}{\partial t}\, ds + \left[\frac{1}{2}u_s^2 + \frac{p}{\rho_0}\right]_{\mathbf{x_A}}^{\mathbf{x_B}} = 0 \tag{2.14}$$

where s is the streamwise direction and u_s is the streamwise velocity whose magnitude is $\sqrt{u^2+v^2}$. To get the potential flow pressure field, we solve Eq. 2.14 for p,

$$p_{\text{potential}} = p\Big|_{\mathbf{x_B}} = \underbrace{p\Big|_{\mathbf{x_A}}}_{\text{offset}} \underbrace{-\frac{1}{2}\rho_0\left[u_s^2\right]_{\mathbf{x_A}}^{\mathbf{x_B}}}_{\text{dip}} \underbrace{-\rho_0\int_{\mathbf{x_A}}^{\mathbf{x_B}} \frac{\partial u_s}{\partial t}\, ds}_{\text{tilt/jump}}\,. \tag{2.15}$$

The potential flow pressure field is made up of three parts, each of which have different physical impacts on the flow. The "offset" is a change in the pressure field over the whole domain with respect to time. Theoretically, it should be the pressure at the entrance to the channel, however, the choice of its value does not affect the inertial form drag because it is constant throughout the domain.

The second part of the potential flow pressure field is the "dip". This part results from the fact that water must travel faster as it goes through a constriction, and by Bernoulli's formula, faster moving fluid must be at a lower pressure. The dip is most prominent when the tidal velocities are maximum. The dip part of the potential flow pressure field can be seen in Fig. 2.2a, where the sea surface height is obtained by dividing the pressure in Eq. 2.15 by $\rho_0 g$. The dip is symmetric across the axis of the headland, and hence, the inertial form drag associated with the dip is zero; any pressure changes created by the dip on the left hand side of the topography are balanced by equal pressure changes on the right hand side. Although this term does not contribute to the inertial form drag, by removing it from the total pressure field we are better able to visualize the residual pressure field.

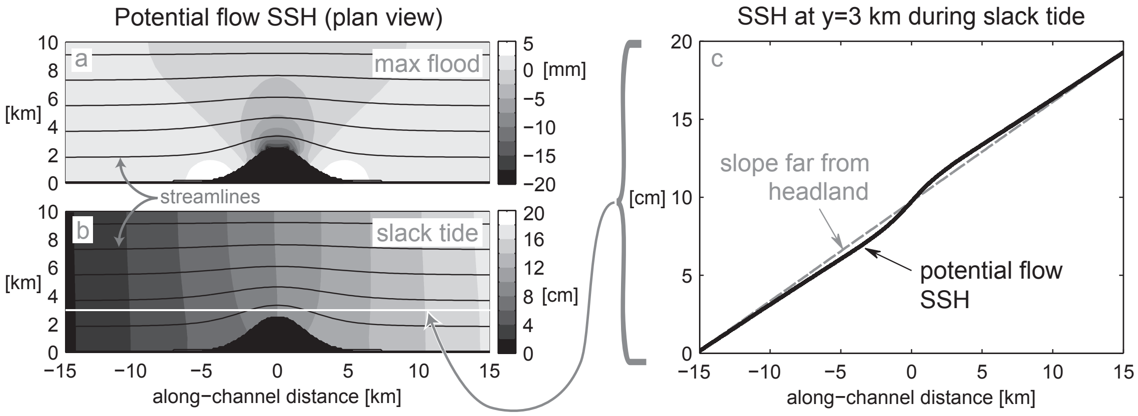

Figure 2.2: The left-hand panels show plan views of the potential flow sea surface height (SSH) calculated from the potential flow pressure field, such that $SSH = p/\rho_0 g$. The black contours show the potential flow streamlines. At maximum flood and ebb tides, the pressure field has the shape shown in (a) with a region of low pressure at the tip of the headland. At slack tide, when the acceleration is greatest, the sea surface height is tilted as shown in (b). This tilt is constant throughout the channel except near the headland, where the slope deviates slightly from the background slope as seen in (c). This extra tilt increases the magnitude of the inertial drag.

The third part of the potential flow pressure field is the "tilt/jump" as seen in plan view in Fig. 2.2b and in side view in Fig. 2.2c. The sea surface height has a constant slope near the beginning and ends of the domain in regions where the channel's cross sectional area is constant. We refer to this slope as the "tilt", but it is often simply called the pressure gradient. Close to the headland, the actual slope deviates from the background value and we refer to this part as the "jump". This is the pressure perturbation classically associated with the "added" or "apparent" mass (Lamb, 1945). In cases where the across-channel headland width is equal to the along-channel, e-folding length of the headland, the relative contributions to the form drag from the jump and the tilt are nearly equal. As the across-channel width of the headland increases, the relative size of the jump also increases. For a more gentle constriction the tilt term would dominate. Of the three terms in Eq. 2.15, the tilt/jump term is the only one that can contribute to the inertial form drag because it is the only one that is not symmetric across the axis of the headland. At slack tide, velocities are zero, but accelerations are maximum and the pressure difference between the left and right sides of the headland has its greatest magnitude.

The most important thing to realize about the inertial drag is that it cannot do work on the flow. The only part of the potential flow pressure field that can contribute to the inertial drag is the tilt/jump term. Since this term has a phase that scales with the time derivative of the streamline velocities, by construction, the phase of the inertial drag will always be in quadrature with the with the phase of the velocity. This means that although the amplitude of the inertial drag may be significant, the tidally averaged power of the inertial drag is always zero.

Additionally, we must make note of the limitations and errors associated with this calculation. The streamfunction and its associated pressure field are calculated assuming that the channel has a rigid lid and that flow in the channel is 2D, having no z-variation. In both the real ocean and in the numerical model, the sea surface height changes and hence pressure fluctuations at the entrance of the channel will take time to propagate down the channel. In the above pressure field calculation in contrast, fluctuations at the entrance of the channel are immediately "felt" throughout the length of the channel. In this study's numerical model, the surface gravity wave speed is approximately 44 m s^{-1} which means that a tidal wave will take about a minute and a half to travel the length of a 4 km headland. This is much faster than other variations in the sea surface height field which occur at the tidal frequency, ω. Hence the sea surface height change associated with the wave does not create a significant amount of form drag. Another limitation that should be noted is that the potential flow pressure field found with the above method is not the exact same pressure field that would result from isolating the irrotational parts of the flow in the model. The basic characteristics would be the same, however, certainly the presence of eddies changes the shape of the irrotational flow field in the model. Despite these limitations, we decided to use the above method to calculate the potential flow pressure field because it has a theoretical basis that is very useful in explaining the different parts of the flow field, and is found to account for much of the form drag created by the headland that previous studies such as Edwards et al. (2004) could not explain.

2.2.3 Total and residual form drags

The method for computing the inertial drag was explained in section 2.2.2, but this only accounts for the irrotational, inviscid part of the flow. The total form drag is commonly thought of as the area integral of the bottom pressure times the bottom slope. It can be derived from the three-dimensional, Boussinesq momentum equation (e.g. McCabe et al. (2006)). In our case, there is no bottom slope, so we rederived the form drag equation to account for the flat bottom and curving side walls. The resulting expression for form drag around a headland is,

$$D_{\text{form}} = -\int_{A_p} p\xi_x \, dA \tag{2.16}$$

where A_p is the area of the wall containing the headland, projected onto the x-z plane, p is the pressure on that wall, ξ is the headland extent in the y-direction, and ξ_x is the slope of the headland in the x-direction. Fig. 2.1 shows the directions of the axes. The negative sign appears in this equation because the form drag removes momentum from the flow.

The separation drag is simply the difference between the total form drag and the inertial drag at each time step,

$$D_{\text{separation}} = D_{\text{form}} - D_{\text{inertial}}. \tag{2.17}$$

This is known as the Morison Equation (Dean and Dalrymple, 1984), and has been used in previous studies as a useful way to divide up the form drag (Lowe et al., 2005). Similarly, the residual pressure field can be obtained by subtracting the potential flow pressure field from the total pressure field. The separation drag can either be calculated with Eq. 2.17 or directly from the residual pressure field using Eq. 2.16. The most important thing to note about the separation drag is that since the inertial drag is nondissipative, the tidally averaged power removed by the total form drag and the separation drag are equal.

2.3 Methods

2.3.1 Specifics of the ROMS model

In order to investigate the form drag due to oscillating flow around headlands, a series of numerical experiments were performed using ROMS, the Regional Ocean Modeling System (Shchepetkin and McWilliams, 2005). ROMS is a three-dimensional, free surface, hydrostatic, terrain-following-coordinate model that solves the baroclinic and barotropic momentum equations separately. Although our model was not intended to accurately model the dynamics near Three Tree Point, the physical dimensions and stratification of our idealized setup were chosen to roughly resemble the Main Basin of the Puget Sound where Three Tree Point is located. The channel in the model was 100 km long, 10 km wide and 200 m deep with closed sides and open ends. The salinity at the surface was 30 and increased linearly to 32 at depth, which resulted in a buoyancy frequency of 0.01 s^{-1}. Although the model was stratified, there were vertical side walls and barotropic tides, so most of the flow outside the frictional boundary layer remained barotropic. Compared to a model run in a channel without stratification, the separation drag changed by only 1.7%.

The tides were modeled as propagating waves in the shape of simple sinusoids, oscillating at the M2 frequency. The maximum tidal velocity and amplitude varied for each run as will be explained in section 2.3.2. In order to force the tides, both the sea surface height and the barotropic velocity oscillated at the same period and phase on the left open boundary of the channel. The tidal wave was allowed to freely propagate downstream at a shallow water wave speed of 44.3 m s^{-1}. The open boundary conditions were set so that both mass, momentum and waves are allowed to leave the domain. Specifically, this meant that the free surface had Chapman boundary conditions, the barotropic momentum had Flather boundary conditions, and both the baroclinic momentum and the tracers had radiation boundary conditions. (For an overview of boundary conditions in ROMS, see Marchesiello et al. (2001).) Nudging of the tracers toward background values and the baroclinic momentum equation toward zero was necessary in 15-km long regions at each end of the domain. This prevented any possible numerical waves reflection off of the open boundaries. The time scale of the nudging was set to be about 2 hours for the tracers and 12 hours for the baroclinic momentum equation. Analysis was done only in the region 30 km upstream and downstream from the headland crest, which ensured that the results were not influenced by the nudging regions at either end.

The horizontal grid of the model was stretched in the along-channel direction, however, this stretching did not affect the analysis region where the grid size was 100 m in both the along- and across-channel directions. Exceptions to this were made for two of the cases with particularly pointy headlands where the grid size had to be reduced to 50 m. With this resolution, there were always at least 10 grid points in the along-channel direction on each headland. There were 20 vertical grid boxes, spaced to provide more resolution near the top and bottom of the domain.

The headlands were Gaussian-shaped. Their across-channel extent, ξ, was defined at every x-coordinate by the equation,

$$\xi(x) = \Delta * exp\left\{-\left(\frac{x - x_{mid}}{L}\right)^2\right\} \tag{2.18}$$

where Δ is the across-channel headland width, L is the along-channel e-folding length of the headland, and x_{mid} is the coordinate in the middle of the domain where the headland crest is located. Numerically, the headlands were simulated using a masking region in the shape of Eq. 2.18.

The model used a generic length scale mixing scheme within the domain. The bottom boundary used a quadratic drag law with a drag coefficient of 3×10^{-3}. The side boundaries were set to have free-slip conditions. The effect of no-slip versus free-slip boundaries was tested. Only very small changes were detected when no-slip side boundaries were used instead of free-slip side boundaries. The lack of change is thought to be due to the fact that the headland itself does not have a perfectly smooth shape since it is defined only to the resolution of the grid. This somewhat jagged nature to the shape of the headland makes it act as if there were no-slip side walls even though they were set to be free slip.

The Coriolis force within the model was set to zero. The decision not to include the Coriolis force was justified by the fact that the Rossby number at Three Tree Point is about 10. Since the effect of the Coriolis force would be minimal, it was decided to leave it out in order to more clearly focus on the dominant mechanisms in the flow. In cases with larger headlands, such as in Freeland (1990) and Magaldi et al. (2008), the Coriolis force is an essential part of flow dynamics.

The model was run for ten full tidal cycles in order to get the domain “spun up” to a tidally-steady state. The analysis was performed on the data from the eleventh and twelfth tidal cycles. Throughout this paper we use the time scale lunar hours (3726 sec) for consistency with the forcing frequency. In order to avoid breaking the Courant-Friedrichs-Lewy (CFL) condition, the model’s time step was 29.8 s, except in the two cases with smaller grids where $\Delta t = 7.5$ s was used. Data was saved once per lunar hour.

2.3.2 Nondimensional parameters and model runs

The goal of this series of numerical experiments was to test how different headland shapes and flow conditions affected the form drag. To do this, a "base run" was created that had dimensions somewhat close to those found at TTP. We then identified two nondimensional and one dimensional parameter that we thought would affect the form drag. Each parameter was systematically varied to cover a range of parameter space, with the other two held constant at their base values. The first nondimensional parameter was the tidal excursion distance divided by the along-channel headland length,

$$\lambda = \frac{\text{tidal excursion distance}}{\text{total headland length}} = \frac{2U_0/\omega}{2L} = \frac{U_0}{\omega L} \tag{2.19}$$

which is equal to the Keulegan-Carpenter number (mentioned briefly in section 2.2.1) divided by a factor of π. The second parameter was the aspect ratio of the headland,

$$\alpha = \frac{\text{across-channel headland width}}{\text{along-channel, e-folding headland length}} = \frac{\Delta}{L} \tag{2.20}$$

which defined how sharp or streamlined each headland was. The final parameter was the expected bluff body drag (D_{BB}) from Eq. 2.1, with $C_D = 1$. These three parameters form a system of equations that can be solved for the maximum tidal velocity (U_0), the headland e-folding length (L) and the headland width (Δ). All other model variables such as the forcing frequency (ω), the depth (H), the channel width and the stratification remained constant. The final parameter that had to be determined was the tidal amplitude, which is related to the tidal velocity in the following way,

$$\eta_0 = \frac{U_0 H}{c} \tag{2.21}$$

Table 2.1: The specifics for all of the numerical experiments. The experimental parameters which characterized each model run were the bluff body drag estimate (D_{BB}), the aspect ratio of the headland (α), and the tidal excursion distance divided by the headland length (λ). The model parameters that were then calculated were the across-channel width of the headland (Δ), the along-channel, e-folding length of the headland (L), the amplitude of the tidal velocity (U_0), and the tidal height (η_0).

run name	$D_{BB} = \frac{1}{2}\rho_0 C_D H \Delta U_0^2$ [N]	$\alpha = \frac{\Delta}{L}$	$\lambda = \frac{U_0}{\omega L}$	Δ [m]	L [m]	U_0 [m/s]	η_0 [m]
base	3.5×10^7	0.9	1	2417.3	2685.9	0.376	1.698
2D	7.0×10^7	0.9	1	3045.6	3384.0	0.474	2.139
0.5D	1.75×10^7	0.9	1	1918.6	2131.8	0.299	1.348
2α	3.5×10^7	1.8	1	3837.2	2131.8	0.299	1.348
1.5α	3.5×10^7	1.35	1	3167.6	2346.3	0.329	1.483
0.5α	3.5×10^7	0.45	1	1522.8	3384.0	0.474	2.139
4λ	3.5×10^7	0.9	4	959.3	1065.9	0.597	2.695
3λ	3.5×10^7	0.9	3	1162.1	1291.2	0.542	2.448
2λ	3.5×10^7	0.9	2	1522.8	1692.0	0.474	2.139
1.5λ	3.5×10^7	0.9	1.5	1844.8	2049.7	0.430	1.944
0.5λ	3.5×10^7	0.9	0.5	3837.2	4263.6	0.299	1.348
0.25λ	3.5×10^7	0.9	0.25	6091.2	6768.0	0.237	1.070

where $c = \sqrt{gH}$ is the surface gravity wave speed. All of the experiments, including the relative size of the nondimensional parameters and headland dimensions, are listed in Table 2.1. Each experiment has been given a name based on the scaling of the parameters. For instance, run 2α has an aspect ratio that is twice as steep as the base run.

2.4 Results

2.4.1 Time series of inertial and separation drags

Before delving into the results from all of the model runs, it is important to understand how the different parts of the drag behave throughout the tidal cycle. In Fig. 2.3, the tidal velocity, drag and power from the base run are all plotted with respect to time over two tidal cycles. The velocity shown here and used in the power calculations is a spatial average of the velocity throughout the analysis region of the domain. The velocity and the three parts of the drag all have the same frequency, but their relative phases are offset from one another. At any point in time, the sum of the separation drag and the inertial drag equals the total drag. The same is true for the power and cumulative averaged power.

At slack tide, the inertial drag is applying its maximum force, and a quarter of a tidal cycle later, when the velocity is maximum, the inertial drag is zero. The power associated with the inertial drag has equal positive and negative parts, so its cumulative average is zero when calculated over even half of a tidal cycle. The phase of the separation drag leads the velocity. At slack tide, the separation drag is about three-quarters of a lunar hour past its zero, which is 22° ahead of the velocity. Since the separation drag and the velocity are close to being in phase with each other, throughout the tidal cycle, the power associated with the separation drag is mostly removing energy from the flow. This differs from the power associated with the total and inertial drags which have both positive and negative parts.

The most important thing to notice from Fig. 2.3 is that although the amplitude of the inertial drag is much larger than the amplitude of the separation drag, the separation drag accounts for all of the tidally averaged power loss.

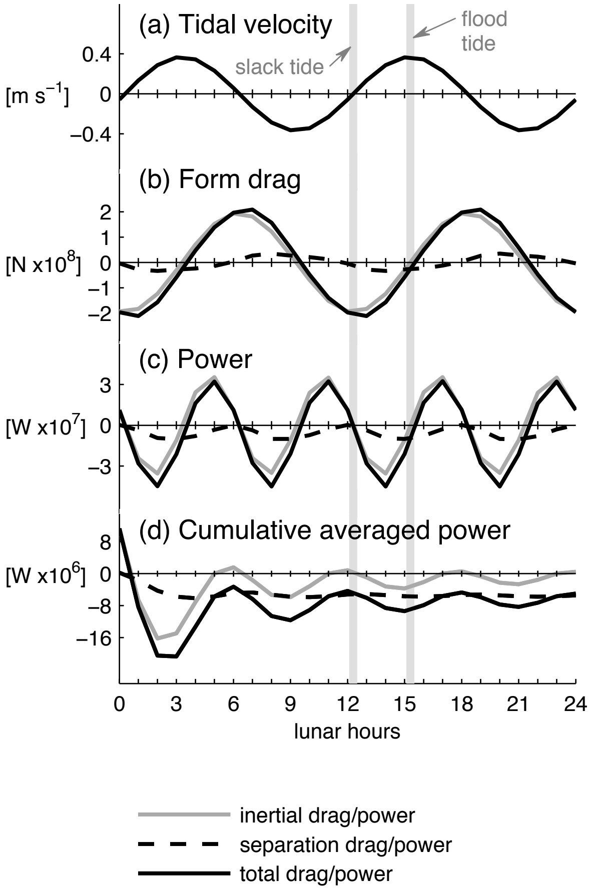

Figure 2.3: The tidal velocity with respect to time for two tidal cycles is plotted in (a). The total form drag (black), the inertial drag (gray) and the separation drag (dashed) are shown in (b) and the corresponding power in (c). The power is simply the product of the velocity and the drag. The cumulative average of the power is shown in (d). Over time, the cumulative — or running — average of the power is approaching an asymptote. Although the amplitude of the inertial drag is nearly as large as the amplitude of the total drag, the separation drag accounts for all of the cumulative power losses after a complete tidal cycle. These curves are from the base run. The relationship between the velocity, drag and power is similar for the other runs.

2.4.2 Inertial drag: Amplitude

The data discussed in the previous section from each model run is condensed into Fig. 2.4, which shows the amplitude of a sinusoidal fit to the separation drag (black bar) and the inertial drag (gray bar). The relative sizes change significantly, especially in the cases where λ was scaled. The estimate of the inertial drag by Dean and Dalrymple (1984) is

$$D_{\text{inertial}} = C_M \rho_0 V \frac{\partial U(t)}{\partial t} \tag{2.22}$$

where C_M is the inertial drag coefficient, V is the volume, and $U(t)$ is tidal velocity defined in Eq. 2.10. For an ellipsoid, the inertial drag coefficient may be shown analytically to be

$$C_M = 1 + \frac{b}{a} \tag{2.23}$$

where a and b are the along- and across-stream semi-major axis lengths of the ellipse (Dean and Dalrymple, 1984). For the Gaussian headlands used in this experiment, there is no analytical solution for C_M, so instead we approximate $a = L$ and $b = \Delta$, and the inertial drag coefficient becomes $C_M = 1 + \Delta/L$. The exact volume of a Gaussian headland is $\sqrt{\pi}\Delta L H$. Using these values for the inertial drag coefficient and the volume, give

$$D_{\text{inertial}} = \left(1 + \frac{\Delta}{L}\right) \rho_0 \sqrt{\pi} \Delta L H \frac{\partial U(t)}{\partial t} \tag{2.24}$$

as a prediction of the inertial drag for a Gaussian headland. The validity of Eq. 2.24 is seen in Fig. 2.5, where the actual inertial drag is compared to this estimate assuming $\frac{\partial U(t)}{\partial t}$ scales as $U_0\omega$. Eq. 2.24 overestimates the inertial drag slightly, as all but one of the runs fall slightly above the 1:1 line. This could be because Eq. 2.24 was derived for flow around a elliptical cylinder, not flow around a Gaussian-shaped headland in a channel, two shapes that have different flow patterns. The exception to this trend is the 0.25λ run which falls below the 1:1 line. This headland was the largest of any

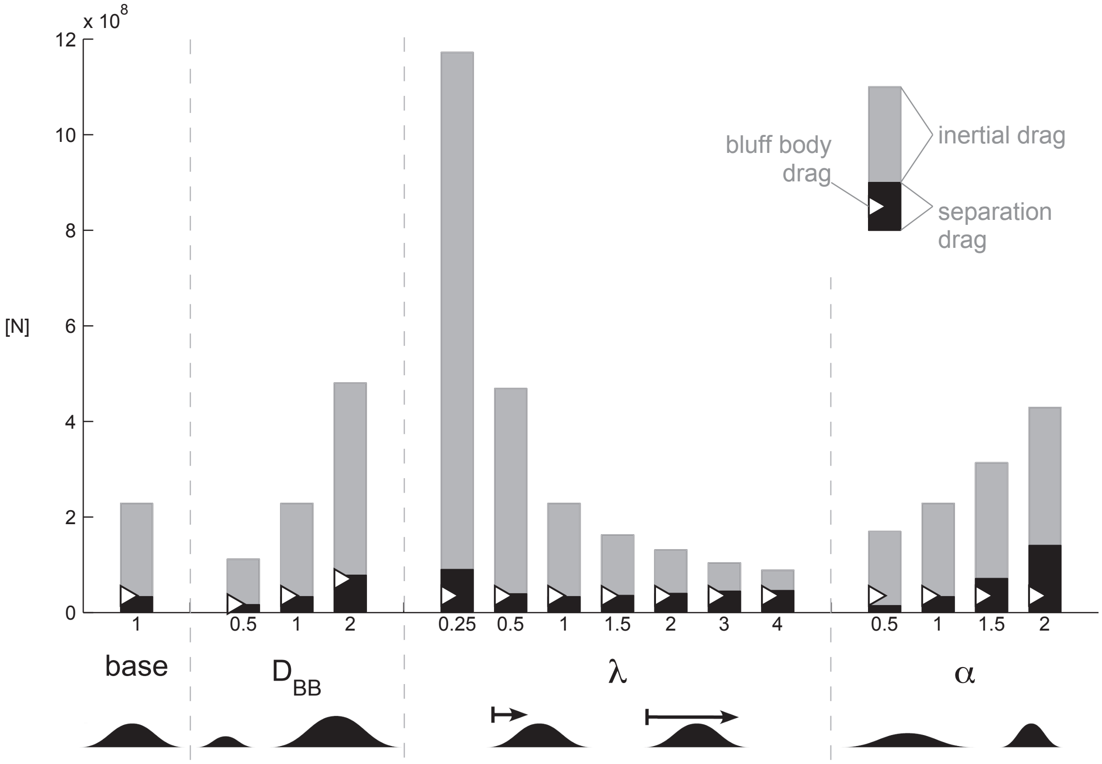

Figure 2.4: Each model run is represented by a bar in the above figure. The gray part of the bar is the amplitude of the inertial drag and the black part of the bar is the amplitude of the separation drag, both calculated with a sinusoidal fit to the data. Their sum is close to the amplitude of the total drag, but not exact due to phase differences between the separation and inertial drags. The white triangles point to the magnitude of the bluff body drag, assuming a drag coefficient of 1. The runs are organized from left to right starting with the base, then the runs where the bluff body form drag parameter (D_{BB}) was changed, then the runs where the tidal excursion distance divided by the along-channel headland length (λ) was changed, and last the runs where the headland aspect ratio (α) was changed. The magnitude of the inertial drag is generally much larger than that of the bluff body drag, and in most cases the magnitude of the separation drag is close to the bluff body drag.

of the headlands tested. Its across-channel width (Δ) was over half the width of the channel and nearly double the size of all of the other headlands. When we reran this

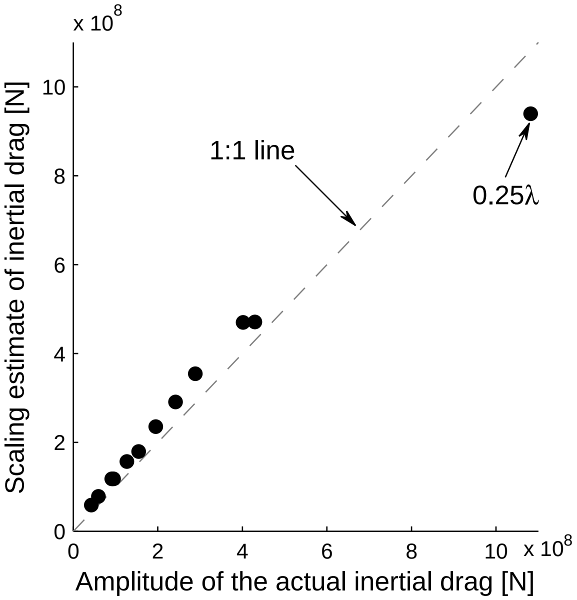

Figure 2.5: This figure shows the relationship between the actual inertial drag and the estimated inertial drag: $D_{\text{inertial}} = \left(1+\frac{\Delta}{L}\right)\rho_0 V U_0 \omega$, where the volume, $V = \sqrt{\pi}\Delta L H$. All of the runs, except the 0.25λ run, fall just above the 1:1 line, so their actual inertial drag is slightly less than the estimated inertial drag. This could be because the scaling relationship was derived for flow around an ellipse, not flow around a Gaussian-shaped headland.

model case in a channel that was twice as wide (20 km) we found that the inertial drag amplitude was much more in line with the trend found for the other runs. The opposite wall was having an effect on the flow patterns in this anomalous case.

Just as in section 2.2.1, Eq. 2.11, we will calculate the ratio of the inertial drag to the bluff body drag:

$$\frac{D_{\text{inertial}}}{D_{BB}} = \frac{\left(1+\frac{\Delta}{L}\right)\rho_0\sqrt{\pi}\Delta L H \frac{\partial U(t)}{\partial t}}{1/2\,\rho_0\,C_D\,\Delta\,H\,U_0^2} = \frac{4\sqrt{\pi}(\Delta+L)}{L_T}. \tag{2.25}$$

As before, we assume that the bluff body drag coefficient is 1 and the tidal excursion distance is $L_T = 2U_0/\omega$. As was found with the cylinder, when the tidal excursion distance is small, the inertial drag dominates over the bluff body drag, and as the tidal excursion distance becomes longer, the impact of the inertial drag wanes.

2.4.3 Separation drag: Amplitude

In order to see how the separation drag changed as λ, α and D_{BB} were scaled, the results from all of the model runs have been organized into Fig. 2.6. The amplitudes of the separation drag for all of the model runs are shown in the top row of panels. In the three cases where the bluff body drag (D_{BB}) was scaled, with λ and α held constant, the separation drag roughly followed the predicted value from Eq. 2.1, as is seen in Fig. 2.6a.

In the cases where the tidal excursion parameter (λ) was scaled, the separation drag stayed relatively constant and nearly equal to the bluff body drag as can be seen in Fig. 2.6b. Hence, the separation drag does not appear to depend on λ. The exception to this trend is the 0.25λ run. As discussed in the previous section, we found that the flow around this headland was significantly affected by the presence of the wall on the opposite side of the channel, which worked to increase both the separation and inertial drags. In the wider channel, the amplitude of the separation drag for this headland differed by only 6.4% from the bluff body drag.

In the four cases where α was scaled, the separation drag does not equal the bluff body drag as seen in Fig. 2.6c. A large α corresponds to a sharper headland, and the separation drag is significantly larger than the bluff body drag. When α is small, the headland is more streamlined and the separation drag is smaller than the bluff body drag. The reason for this discrepancy is because we assumed a drag coefficient of 1 when calculating the bluff body drag. It is expected though, that sharper headlands would have higher drag coefficients than more streamlined headlands. A histogram of the drag coefficients calculated using $C_D = \frac{D_{\text{separation}}}{1/2\rho_0 \Delta H U_0^2}$ is shown in Fig. 2.7. Eight of

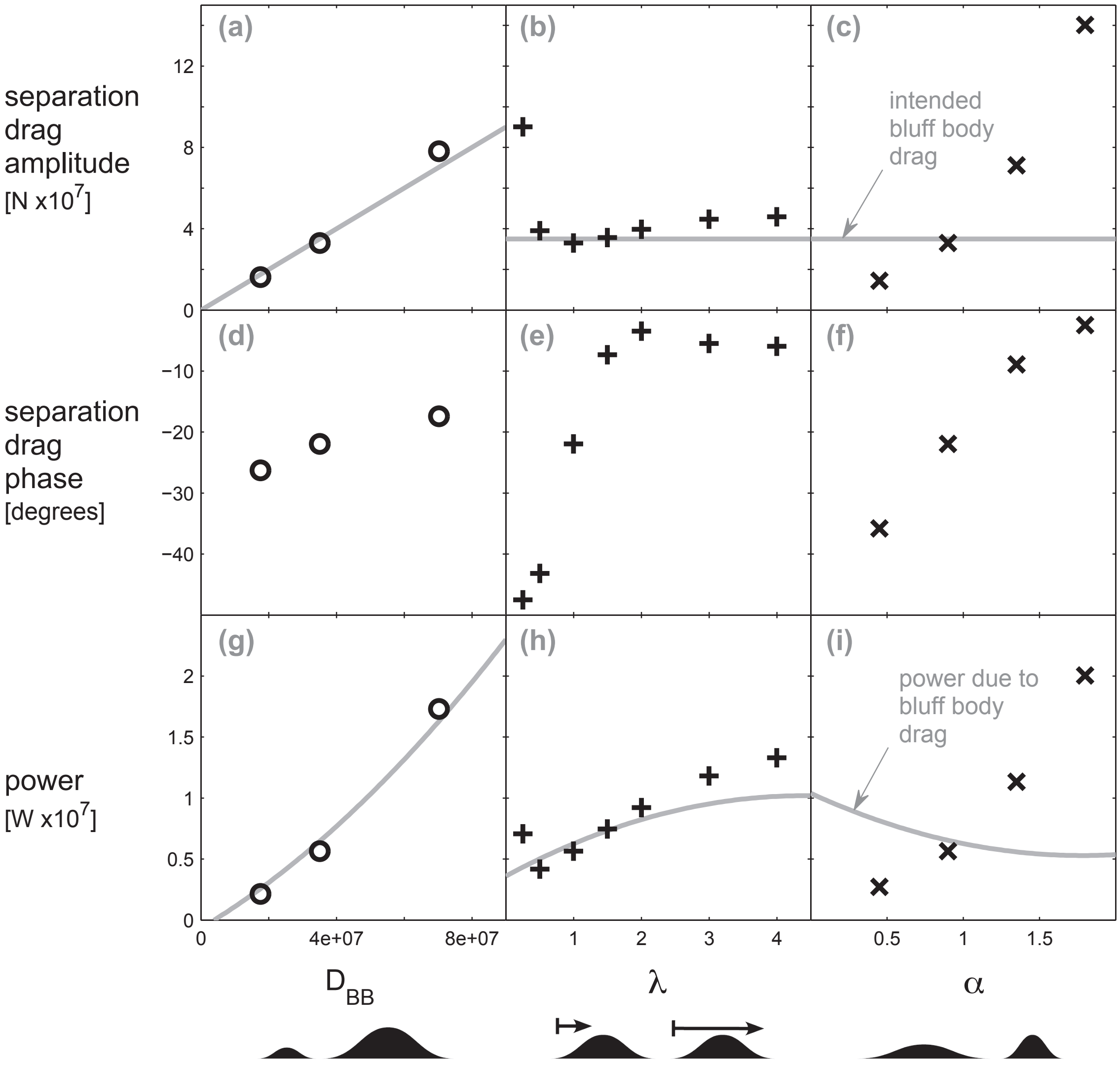

Figure 2.6: Each column of panels shows how the separation drag changed as the three experimental parameters (D_{BB}, λ and α) were scaled. Each row shows a property of the separation drag: the amplitude in Newtons at the top, the phase difference between the separation drag and the velocity in degrees in the middle, and tidally averaged power that the drag can remove from the flow in Watts on the bottom. The gray line in panels (a), (b) and (c) is the bluff body drag with a drag coefficient of 1. The gray line in panels (g), (h) and (i) is the tidally averaged power loss due to the bluff body drag, $< P >= \frac{1}{2}U_0 D_{BB}$.

the runs have drag coefficients that are close to 1. This corresponds well to Hoerner (1965)'s estimate of a drag coefficient of 1.17 for flow around a cylinder at a high Reynolds numbers. The exceptional runs are the three cases where α was scaled and the anomalous 0.25λ run. The case with the sharpest headland (run 2α) has the largest drag coefficient, and the case with the most streamlined headland (run 0.5α) has the smallest drag coefficient. A drag coefficient of 4 is surprisingly large. However, it is hard to compare this number to experimentally determined drag coefficients, which have only been found for steady flow conditions around objects of all shapes (Hoerner, 1965) and for cylinders in oscillating flow (Obasaju et al., 1988), but not for odd-shaped objects in a channel subjected to oscillating flow. The important point is that as the headland aspect ratio (α) increases, so does the drag coefficient.

From the trends that are observed in the top row of Fig. 2.6, we can say that the separation drag is proportional to the bluff body drag provided a reasonable drag coefficient is used.

2.4.4 Separation drag: Phase and power

The plots in the middle row of Fig. 2.6 show the phase of the separation drag in relation to the phase of the tidal velocity. In every case, the drag leads the velocity. Similar phase leads have been found in lab experiments of oscillating flow around a cylinder (Obasaju et al., 1988), and at Three Tree Point, where it was found that the phase of the drag led the tidal velocity by 1-2 hours (McCabe et al., 2006), which is between 30° and 60°.

The relationship between the tidal excursion distance parameter, λ, and the phase of the separation drag is shown in Fig. 2.6e. When the tidal excursion distance is shorter than the headland length — cases of small λ — the drag leads the velocity by about 45°. An analogy may be drawn to the description by Batchelor (1967, p.

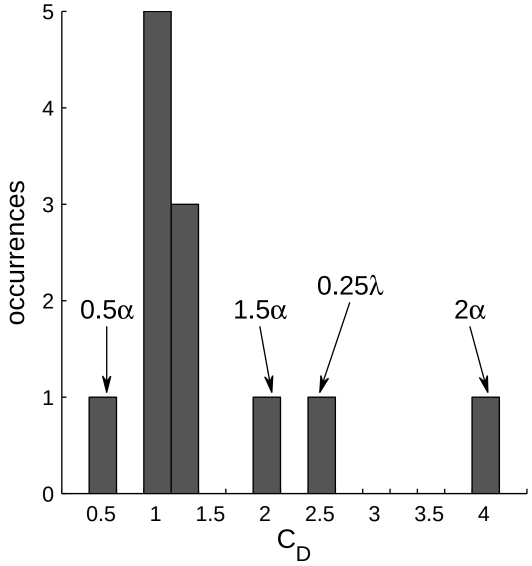

Figure 2.7: Histogram of drag coefficients for the separation drag for all of the runs. Most of the runs fall on or just above a typical drag coefficient of 1. The exceptions are the cases where α was changed to create a sharper or more streamlined headland. The last exception is the anomalous 0.25λ run.

353-358) of a 45° phase lead of the frictional stress on an oscillating flat plate. On the other extreme, when the tidal excursion distance becomes longer than the headland length, the drag becomes nearly in phase with the velocity. This makes sense because as the tidal excursion distance gets longer, the flow is heading towards a quasi-steady state. So in general, when λ is less than one the phase lead of the drag will be about 45°, when λ is greater than 1 the drag and velocity will be in phase with each other, and when λ is close to 1 the phase difference will fall in a transitional region between 45° and 0°.

The bottom row of panels in Fig. 2.6 show the tidally averaged power that the separation drag can remove from the flow. This is equal to the power loss from the total drag, as explained in section 2.4.1. Recall, that power is the product of drag and velocity, so for two functions oscillating at the same frequency such as $U(t) = U_0 sin\, \omega t$ and $D(t) = D_0 sin(\omega t - \varphi)$ where φ is the phase difference between the two, the tidally averaged power is $< P >= \frac{1}{2} D_0 U_0 cos(\varphi)$. Now, looking at panels (b), (e) and (h) in Fig. 2.6, the relationship between the phase of the separation drag and the tidally averaged power can be seen. The gray line is the theoretical power of the bluff body drag, $< P >= \frac{1}{2} D_{BB} U_0$. Although the amplitude of the drag changes very little when λ is scaled (except for the 0.25λ run), the power loss more than doubles when λ is increased from 0.5 to 4. This is due partly to the phase change and partly to the increasing tidal velocity. Although knowing the amplitudes of the drag and the velocity will give a good indication of the expected power loss, the phase can also create changes in the total power loss.

In the cases where the aspect ratio of the headland changes, there is a distinct phase change as can be seen in Fig. 2.6f. For streamlined headlands, the phase is approaching the 45° limit that was observed for the small λ cases. However, unlike when the tidal excursion parameter changed and there was an abrupt jump from a 45° to 0° phase lead, here, the phase seems to increase in a nearly linear fashion. It is possible, that there are limits near 0° and 45° for this parameter too. The experimental range of α is more limited than the range of λ, so possibly the aspect ratio all of our runs fell in the transitional-phase region between 45° and 0°. As expected, since the amplitude and the phase of the separation drag are both increasing as α gets larger, the power in panel (i) is also increasing substantially.

For the cases where the bluff body drag was scaled, there is a 10° change in phase as the drag increases, Fig. 2.6d, but this variation is small compared with the other two cases. Since the phase shift is small, the change in power is due more to the increasing separation drag amplitude and tidal velocity than to the change in phase between the drag and the velocity.

2.4.5 Description of flow through a tidal cycle: What mechanisms create the separation drag and its phase?

To gain intuition about the mechanisms that create the separation drag, it is useful to look at the residual pressure field and contours of relative vorticity over half of a tidal cycle. Fig. 2.8 shows an ebb tide for the base case. The residual pressure field is found by simply subtracting the potential flow pressure from the total pressure. The form drag depends on the pressure right next to the headland's edge, especially in regions where the headland has a steep angle, ξ_x. The greatest form drag occurs when there is a high pressure on one side of the headland and a low pressure on the other.

Looking at the six panels depicting the ebb tide of the base case in Fig. 2.8, two prominent mechanisms that create form drag can be seen: low pressure regions associated with eddies and high pressure regions resulting from water "piling up" behind the headland and the eddies. In the first panel, at slack tide just before the tide begins to ebb, there is an eddy left over from the previous flood and there is also a high pressure region just to the right of the eddy. Since the low pressure and the high pressure regions are both on the same side of the headland, the form drag is nearly zero at this time step. As the tide begins to ebb (flow to the left) during the next two lunar hours, the strength of the eddy dipole increases. However, its direct contribution to the form drag is weakened as it is pushed toward the tip of the headland. At the same time, the high pressure region on the upstream side of the headland is growing in size and magnitude. Not only are the eddies blocking the ebb tide from getting around the headland, but their circulation pushes more water back upstream. The separation drag reaches is maximum two lunar hours after slack tide,

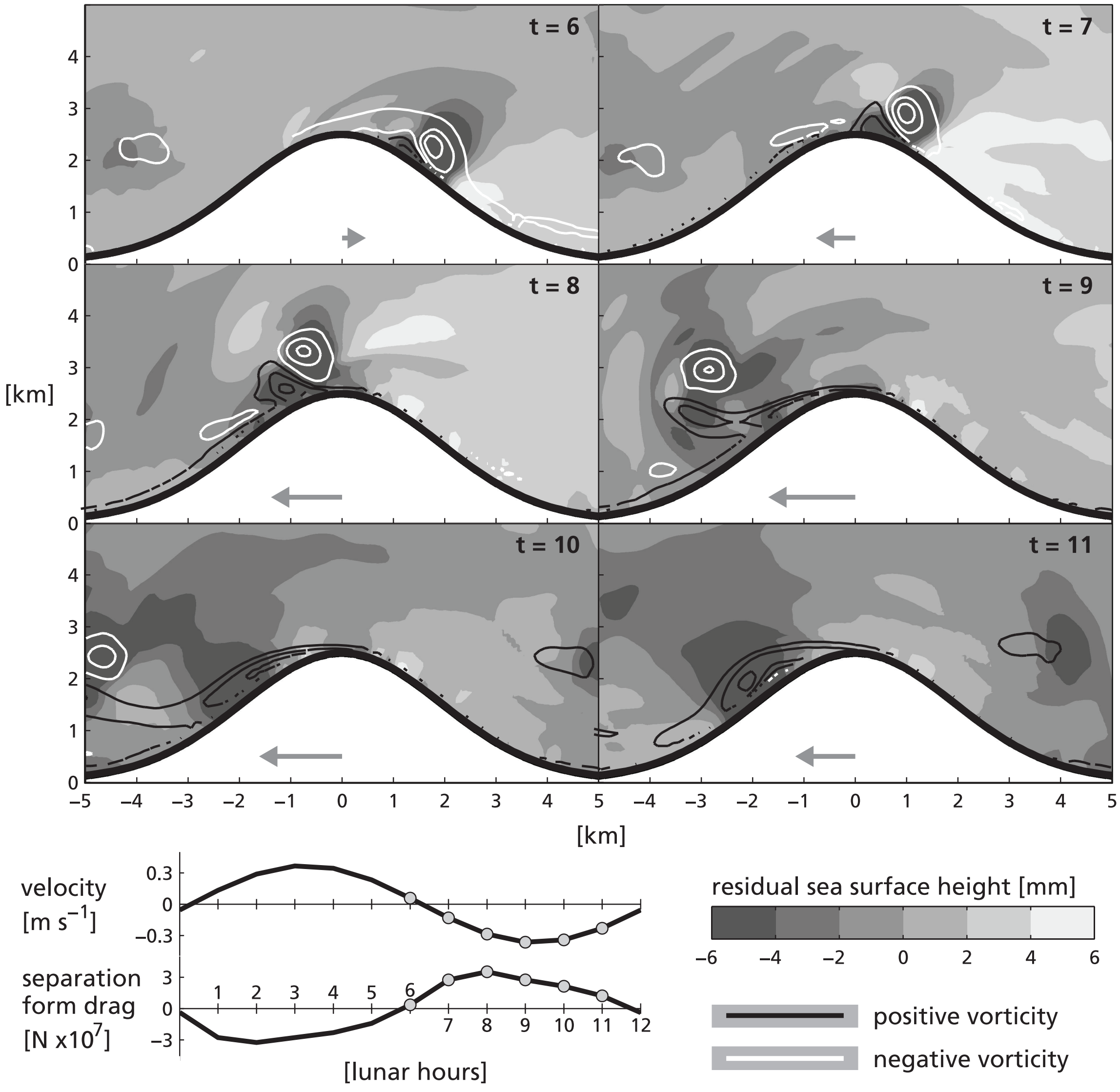

Figure 2.8: Top view snapshots of the headland during the last 6 time steps of a tidal cycle for the base case, showing the evolution of the residual sea surface height and associated vorticity field throughout an ebb tide.

at $t = 8$ when there is the most water piled up on the upstream side of the headland.

At the following time step, the tidal velocity reaches its maximum and the eddy dipole begins to move downstream away from the headland. Not all the vorticity travels with the dipole. Some remains on the leeward side of the headland for the next four lunar hours until the tide changes direction and begins to flood. At the same time, the water that was piled up on the upstream side of the headland is slowly making its way to the left around the headland. However, even though the high pressure on the upstream side is waning, the low pressure on the downstream side associated with the eddy is increasing in strength, so a substantial amount of form drag is still present all the way through the remainder of the ebb tide. The form drag only takes two lunar hours to go from zero to its maximum, but then takes four lunar hours to return back to zero. After the ebb tide, the currents switch and the pattern repeats itself in the opposite direction. There is very little difference in the magnitude of the eddies or the separation drag between the flood and ebb tides.

All of the other runs have basically the same mechanisms creating the form drag as the base run. There are some small differences that can be noted. For instance, in cases with sharp headlands, the eddies are larger and stronger, and hence there is more separation drag. The drag is also more in phase with the velocity because when the dipole eddy is shed downstream, a greater amount of vorticity remains on the headland than in the base case and it takes longer for the piled up water to flow around the headland. Therefore, the maximum form drag and the maximum velocity occur at nearly the same time. In general, for all of the runs, the eddies create low pressure regions in their vicinity and block the flow in nearby areas to create high pressure regions. This creates the separation drag. The position and timing of the eddies' release determines the phase of the drag.

2.5 Conclusion

In this study of form drag generated by oscillating flow in a channel around headlands, the drag was divided into two portions. The inertial portion was derived by numerically solving for the pressure field associated with the irrotational, inviscid part of the flow. The inertial drag can have a significant amplitude, however it cannot do work on the flow since its phase is in quadrature with the velocity. The other part of the form drag is the separation drag associated with flow features such as eddies. The power that can be extracted from the flow by the separation drag is equal to the power associated with the total drag.

Headlands with different sizes and flow characteristics were tested with a numerical model. These experiments confirmed the results of Edwards et al. (2004): in oscillating flow situations when the tidal excursion distance is nearly equal to the topographic length, the total drag will be larger than the bluff body drag due to the added impact of the inertial drag. Furthermore, we showed that in cases where the tidal excursion distance was shorter than the topographic length, the inertial drag was larger than the separation drag and the separation drag led the velocity by about 45°. As the tidal excursion distance becomes longer, the inertial drag becomes smaller and the separation drag and the velocity become more in phase. The magnitude of the separation drag was close to the bluff body drag estimate provided the aspect ratio of the headland was close to 1, otherwise, sharper headlands have higher drag coefficients and hence more separation drag than streamlined headlands.

Chapter 3

MEASUREMENT OF TIDAL FORM DRAG USING SEAFLOOR PRESSURE SENSORS

As currents flow over rough topography, the pressure difference between the up- and downstream sides results in form drag — a force that opposes the flow. An array of bottom pressure sensors was used to measure the tidal form drag on a 1 km-long, 200 m-deep headland with sloping side walls in Puget Sound, WA. The form drag reached 1×10^4 N m^{-2} during peak flood tides (0.2 m s^{-1}). The average power removed from the barotropic tidal currents by the form drag was 0.2 W m^{-2}, which is 30 times larger than the power losses due to friction. Drag estimated from the shallow water momentum equation compares well to the form drag calculated from bottom pressure. The form drag is best parameterized by a linear wave drag law as opposed to a bluff body drag law because both internal waves and eddies are generated on the sloping topography and play a role in the production of form drag. Maximum turbulent kinetic energy dissipation rates of 5 $\times 10^{-5}$ W kg^{-1} were measured with a microstructure profiler. This study provides an example of form drag generation over topography in a strongly tidal, coastal setting revealing that frictional drag parameterizations are not sufficient in places where form drag is the dominant dissipation mechanism.

3.1 Introduction

The energy in ocean currents is partly dissipated through friction as currents flow over flat sea beds, but also through form drag where currents in stratification encounter rough topography. Often form drag has a magnitude that is much larger than frictional drag (Edwards et al., 2004), however, form drag is patchy because it only occurs in regions of rough topography. Frictional drag usually acts only on the fluid in the bottom boundary layer, whereas form drag leads to mixing and turbulence throughout the water column and creates eddies and internal waves that carry energy away from the topography (Polzin et al., 1997; Jayne and St. Laurent, 2001; Rudnick et al., 2003; Garrett and Kunze, 2007). The magnitude of frictional drag is relatively well-parameterized, whereas the creation of a general drag parameterization is difficult since much less is known about the magnitude and spatial distribution of form drag despite some recent advances (Nikurashin and Ferrari, 2011).

An eventual goal of form drag research is to improve drag parameterizations in large-scale numerical models. Models often neglect form drag because they do not resolve the scales at which form drag occurs, which can lead to over-prediction of velocities (Oke et al., 2002). Better drag parameterizations will likely improve ocean models just as they did for atmospheric weather prediction models (Lott and Miller, 1997; Wood et al., 2001; Kim et al., 2003).

Total form drag — due to bottom pressure anomalies — has not previously been measured in the ocean. Only the parts related to changes in isopycnal height ("internal" form drag) (Moum and Nash, 2000; Nash and Moum, 2001; Edwards et al., 2004) and perturbations of the sea surface ("external" form drag) (McCabe et al., 2006) have been quantified. In this experiment, total form drag was measured with pressure sensors in a similar way to mountain drag in the atmosphere (Bougeault et al., 1993). Precise bottom pressure sensors (Ppods) (Stöber and Moum, 2011) were deployed across Three Tree Point (TTP), a headland in Puget Sound, Washington that is subjected to predictable tidal currents. TTP has been studied extensively in the past: Edwards et al. (2004) and McCabe et al. (2006) quantified the internal and external form drag, respectively, Canals et al. (2009) described the tilted eddies present there, and Warner and MacCready (2009) (WM09) showed with a numerical model that there is an additional part of the form drag that arises in oscillatory flow situations (“inertial” form drag). In this study, total form drag from bottom pressure sensors, “bulk” drag from the shallow water momentum equation, internal form drag, inertial form drag, frictional drag, and turbulent dissipation are all quantified.

There are three goals of this paper: first, to develop a method for measuring form drag on undersea topography using bottom pressure gauges, second, to parameterize form drag in terms of existing drag laws, and finally, to determine what physical mechanisms create form drag at TTP. Our field observations are described in section 3.2. Bottom pressure measurements are discussed in section 3.3. In section 3.4, form drag is calculated from bottom pressure anomalies. The density, microstructure and velocity measurements and their implications for form drag are described in sections 3.5, 3.6, and 3.7. The inertial drag is discussed in section 3.8. Finally, the results of this study are compared to form drag parameterizations in section 3.9.

3.2 Experiment details

Three Tree Point is a triangular headland located in a relatively straight section of the Main Basin of Puget Sound (Fig. 3.1). At the surface, it is just over 1 km wide in the along-channel direction at its base and it juts out by 1.5 km into the 5 km wide channel. The mean depth in this region is 200 m. TTP has very steep side walls with a slope of 1:5.

The field experiment took place from October 25, 2010–November 1, 2010. Eight autonomous Ppods were deployed along two transect lines (Fig. 3.1b-d). They are modified Paroscientific pressure sensors which have a precision of 1.4 Pa and take measurements every second (Moum and Nash, 2008). Seven bottom landers, each

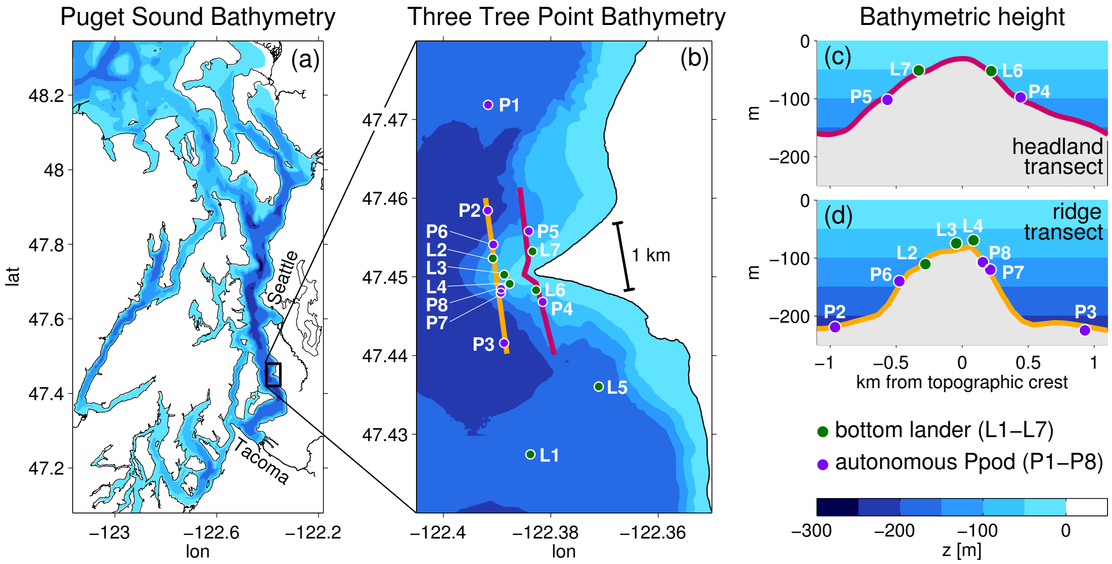

Figure 3.1: (a) Puget Sound bathymetry. Three Tree Point is located between Seattle and Tacoma in a relatively straight section of the Main Basin. (b) TTP bathymetry. The location of the two ship transects (yellow and magenta lines), bottom landers (green markers), and autonomous Ppods (purple markers) are shown. (c) The bathymetric height and instrument locations along the headland transect. The transect is oriented as if the viewer is looking from the center of the channel towards land with north to the left and south to the right. In this orientation, flood tides flow from left to right. (d) The bathymetric height and instrument locations along the ridge transect.

equipped with an upward looking RDI ADCP (150 kHz, 300 kHz or 1200 kHz, depending on depth), a SBE Microcat, a Ppod, and an acoustic release were also deployed. For stability, the landers had to be placed on relatively flat areas, therefore L3 and L4 were positioned slightly off the transect lines. L5 was placed on the south side of the topography to observe the lee eddies during flood tides. Both the ADCP and the Ppod on lander 7 failed, and subsequently were not used in the analysis (Appendix A).

Two ships took measurements along the transects (Figs. 3.1b and 3.2e). Along

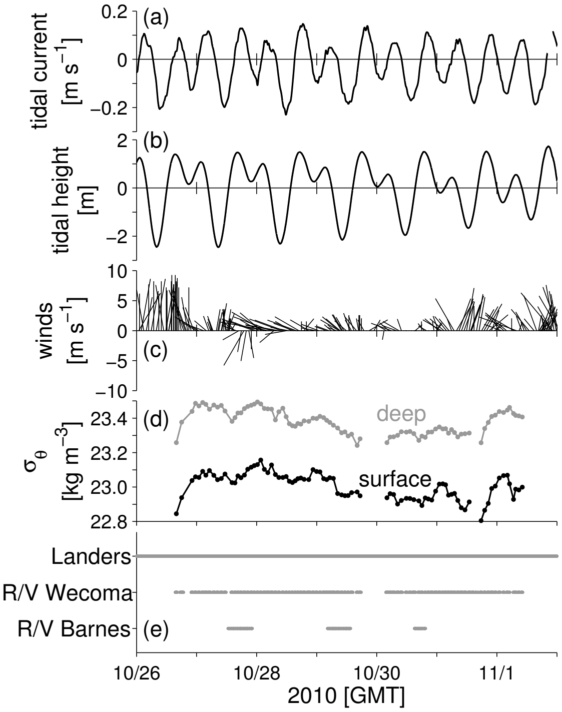

Figure 3.2: (a) Tidal currents. Floods tides are negative because they flow to the south. (b) Tidal height. (c) Wind speed and direction. The wind was blowing from the south throughout the majority of the experiment. (d) Potential density for surface waters (less than 20 m) and deep waters (greater than 20 m). (e) Periods of instrument deployment and ship transects.

the ridge transect, the R/V Wecoma collected continuous ship-mounted ADCP and echosounder data. A Chameleon profiler (Moum et al., 1995) was yo-yoed from the stern measuring salinity, temperature and microstructure. The Chameleon was dropped until it hit the bottom or to 160 m, whichever was shallower, allowing at least 10 casts per transect. Between October 26 and November 1, 90 transects were completed each taking about an hour to go southward while taking Chameleon measurements and a half hour to return back to the start. Along the headland transect, the R/V Barnes collected ship-mounted ADCP velocities for 10 hours on October 27, for 9 hours on October 29, and for 5 hours on October 30. The schedule was chosen to capture the flow patterns during strong flood and ebb tides. There were four CTD stations along the headland transect that were performed with a SBE 19 SEACAT Profiler.

In Puget Sound, the tides are mixed semidiurnal with flood tides flowing to the south (Fig. 3.2a, b). The flood currents are faster than the ebbs at TTP due to the topographic siphoning of the ebb currents through Colvos Passage rather than through the channel where TTP is located (Bretschneider et al., 1985). The experiment took place during neap tide, therefore, it is likely that our estimates for form drag are lower than they would be at the height of spring tide. The background tidal velocity (u_0) was found by vertically averaging the ADCP velocity from the L1 lander and using principle component analysis (Emery and Thomson, 2004) to find the dominant current direction. It was then lowpass filtered with a 60-minute Hanning window to get a smooth tidal velocity signal. The winds were from the south and always less than 10 m s^{-1} (Fig. 3.2c). They were especially weak during the time of the ship transecting. The potential density changed slightly throughout the experiment, but the stratification remained relatively constant (Fig. 3.2d).

3.3 Bottom pressure anomalies

3.3.1 Calculating bottom pressure anomalies from Ppods

Form drag (D_{form}) is defined as the spatial integral of the bottom pressure times the bottom slope. A detailed derivation of form drag from the momentum equation can be found in McCabe et al. (2006),

$$D_{form}(t) = -\int_{A_0} p'_{bot}(x,y,t)\,\zeta_x\,dA_0 \tag{3.1}$$

where A_0 is the projected horizontal area of the bottom, p'_{bot} is the bottom pressure anomaly, ζ is the bottom height, and ζ_x is the bottom slope in the along-channel direction. Form drag is negative because it removes momentum from the flow. The associated power, or energy conversion rate, is simply the form drag times the background tidal velocity, u_0.

Ppods measure the total pressure at the seafloor (p_{bot}). When calculating form drag, the bottom pressure anomaly (p'_{bot}) is used because the total pressure is dominated by the resting depth and tidal height variations. Assuming hydrostatic, p must obey

$$\frac{\partial p}{\partial z} = -\rho g \tag{3.2}$$

where $p = p(\mathbf{x}, t)$ is the total pressure that varies in all directions ($\mathbf{x} = (x, y, z)$) and in time (t), z is positive up, $\rho = \rho(\mathbf{x}, t)$ is the density, and g is gravity. The density can be broken into three parts, $\rho(\mathbf{x}, t) = \rho_0 + \overline{\rho}(z, t) + \rho'(\mathbf{x}, t)$ where $\rho_0 = 1023$ kg m^{-3} is a constant background density, $\overline{\rho}(z, t)$ is the background stratification, and $\rho'(\mathbf{x}, t)$ is the remaining density perturbation. Substituting into (3.2) and integrating vertically we obtain

$$p(\mathbf{x}, t) = g\rho_0(\eta(x, y, t) - z) + g\int_z^\eta \overline{\rho}(z, t)\, dz + g\int_z^\eta \rho'(\mathbf{x}, t)\, dz. \tag{3.3}$$

Next, we divide the sea surface height into three parts: $\eta(x, y, t) = \overline{\eta}(t) + \eta_{tilt}(x, t) + \eta'(x, y, t)$. Here, $\overline{\eta}(t)$ is a spatial average of the sea surface, $\eta_{tilt}(x, t)$ accounts for an along-channel tilt of the sea surface due to tidal acceleration, and $\eta'(x, y, t)$ is the remaining sea surface anomaly. Substitute into (3.3) to obtain hydrostatic pressure:

$$p(\mathbf{x}, t) = \rho_0 g\overline{\eta}(t) + \underbrace{\rho_0 g\eta_{tilt}(x, t)}_{\star} + \underbrace{\rho_0 g\eta'(x, y, t)}_{\star} - \rho_0 gz + g\int_z^\eta \overline{\rho}(z, t)dz + \underbrace{g\int_z^\eta \rho'(\mathbf{x}, t)dz}_{\star}. \tag{3.4}$$

Only the starred terms contribute to form drag in (3.4). The first term, $\rho_0 g\overline{\eta}(t)$, is due to the tides and is the same everywhere within the domain. The inertial form drag (WM09) is given by $\rho_0 g \eta_{tilt}(x,t)$ and will be discussed in detail in section 3.8. The third term, $\rho_0 g \eta'(x,y,t)$, accounts for local perturbations of the sea surface and can have a magnitude of a few centimeters at the center of eddies (McCabe et al., 2006). The fourth term, $-\rho_0 g z$, accounts for the depth of each pressure sensor. The fifth term, $g\int_z^\eta \overline{\rho}(z,t)\,dz$, is the pressure due to a spatially averaged stratification and does not vary horizontally within the domain. Finally, $g\int_z^\eta \rho'(\mathbf{x},t)dz$ accounts for vertical displacement of isopycnals, most obviously created by internal lee waves and eddies.

The pressure anomaly that is dynamically relevant to form drag includes the starred terms from Eq. 3.4 and an additional term to account for nonhydrostatic pressure (p_{nh}):

$$\underbrace{p'(\mathbf{x},t)}_{\text{dynamic pres.}} = \underbrace{\rho_0 g \eta_{tilt}(x,t)}_{\text{inertial pres.}} + \underbrace{\rho_0 g \eta'(x,y,t)}_{\text{external pres.}} + \underbrace{g\int_z^\eta \rho'(\mathbf{x},t)dz}_{\text{internal pres.}} + \underbrace{p_{nh}(\mathbf{x},t)}_{\text{nonhydro. pres.}} \quad . \tag{3.5}$$

The nonhydrostatic pressure is assumed to be small. It is included in Eq. 3.5 for completeness. This dynamic pressure anomaly — evaluated at the sea floor — is what will be used to calculate form drag with Eq. 3.1.

This pressure decomposition is most appropriate for topography that generates both internal waves and eddies. It differs from other pressure decompositions. Potential vorticity conservation defines a barotropic pressure with $p = p(\rho)$ and a baroclinic pressure with gradients of density and pressure that are not parallel (Vallis, 2006). For internal waves, Kunze et al. (2002) divides the pressure into barotropic and baroclinic parts by calculating vertical isopycnal displacements. The baroclinic pressure includes pressure fluctuations due to internal waves and has a zero vertical mean. Here, the use of “internal” and “external” pressures are used to highlight isopycnal and sea surface perturbations and are not equivalent to baroclinic and barotropic pressures.

To get the dynamic pressure anomaly (p'_{bot}) from the raw Ppod pressure the following steps are taken. We use P7 as an example because it was located on a very steep section of the topography and therefore prone to instabilities. The largest part of the Ppod pressure is the resting depth ($-\rho_0 g z$ in Eq. 3.4), which is about 130 dbar for P7 (Fig. 3.3a). The resting depth is calculated as an average of the raw pressure from each Ppod over the exact same time period, ensuring that the same tidal height variations are included equally for each Ppod. The second biggest part of the pressure signal comes from the tidal height ($\rho_0 g \overline{\eta}$ in Eq. 3.4) which has a range of 4 m. It is taken to be an average of the pressure from the two Ppods that were located far from the topography (L1 and P1). This avoids contamination of the background pressure with pressure perturbations occurring near the topography. The final term in Eq. 3.4 does not contribute to form drag is $g \int_z^\eta \overline{\rho}(z,t)dz$. This simplification is valid because $\rho_0 \gg \overline{\rho}$ so $g \int_z^\eta \overline{\rho}(z,t)dz$ is much smaller than $-\rho_0 g z$ and $\rho_0 g \overline{\eta}$, and since it does not vary spatially, it cannot affect form drag.

Distinct shifts are visible in the Ppod pressure anomaly (Fig. 3.3b). These occurred when the autonomous Ppods shifted or rolled on the steep topographic slopes. P7 moved downward by about 1 m over the duration of the deployment. A component of g-force from the accelerometer within the Ppod shows that when the pressure changed, the Ppod also moved (Fig. 3.3c). To fix these, the pressure anomalies before and after the sinks are aligned by eye. At times when the pressure could not be aligned visually, parts of the record had to be discarded. For instance, in the case of P7, there were numerous sinks before 10/28 and the periods of time between the sinks when the Ppod was stable were quite short, and the first 40 hours of data had to be discarded.

Further treatment of the dynamic bottom pressure anomalies included removing spikes and long term trends when necessary. All of the pressure anomalies were low-

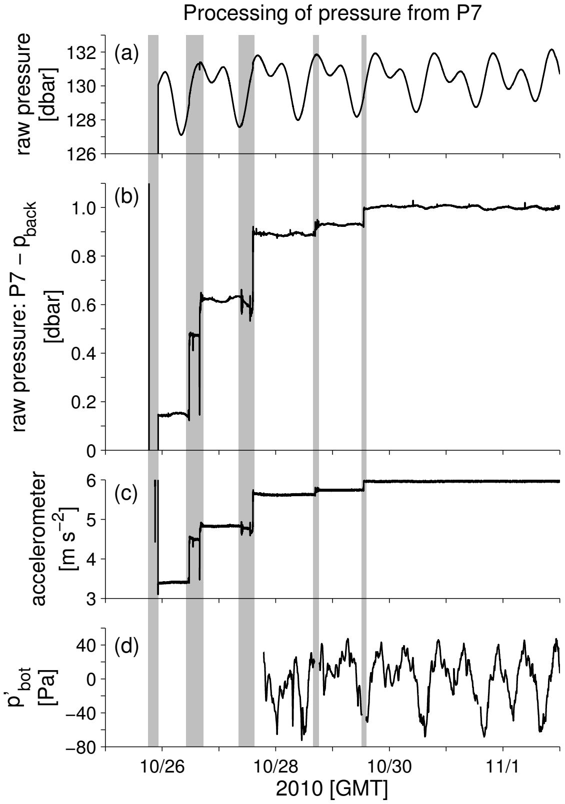

Figure 3.3: (a) Raw pressure from P7. Periods of time where the Ppod was sinking or rolling are highlighted by the vertical gray bars. (b) The pressure difference between p_{P7} and $\mathrm{p_{back}} = \frac{1}{2}(p_{L1}+p_{P1})$. The sinking or rolling of the instrument is clearly visible as abrupt changes in the pressure anomaly. (c) The first component of g-force from the accelerometer within the Ppod. (d) The final bottom pressure anomaly after the sinks and rolls had been corrected.

pass filtered with a 15-minute Hanning window to remove high frequency jaggedness and variability. After processing, the dynamic bottom pressure anomalies are 1000 times smaller than the raw pressure. Sources of error associated with calculating the bottom pressure anomalies are discussed in Appendix A.

3.3.2 Fluctuations of bottom pressure anomalies

When tides flow over and around TTP, the bottom pressure anomalies fluctuate (Figs. 3.4 and 3.5). Along the ridge transect, a difference can be seen in the size of the anomalies from one side of the topography compared to the other. The two Ppods on the north side of the headland (Fig. 3.4b,c) have smaller anomalies and more erratic variability than the two on the crest (Fig. 3.4d,e) and the two on the south side of the headland (Fig. 3.4f,g). The flood tides are faster than ebbs so larger pressure anomalies on the lee side of the topography during flood are expected. Furthermore, it is possible that the asymmetry of the headland topography itself — the south side is steeper than the north side — augments this difference in bottom pressure anomaly strength.

Repeated patterns of highs and lows that correspond to the tidal currents are visible in the zoomed-in view of the bottom pressure anomalies (Fig. 3.4i-n). The light gray vertical bar highlights a two-hour window spanning maximum flood tide. The Ppods at the headland crest and on the south (downstream) side of the topography show low bottom pressure anomalies with magnitudes greater than 50 Pa. The low anomaly starts at least an hour and a half before maximum flood tide and extends for another two or more hours after maximum flood tide. A lee wave is formed on the south side of the topography and is only released when the tides have slackened sufficiently. The pressure anomalies on the north (upstream) side of the headland are essentially zero throughout the same time period. This difference in pressure across the topography is what creates form drag. The pattern of bottom pressure anomalies during ebb tide is the opposite of flood. On the north (downstream) side of the headland and at the headland crest the bottom pressure anomalies are nearly zero. On the south (upstream) side, the bottom pressure anomalies are positive. The smaller pressure anomalies during ebb mean less form drag than during flood.

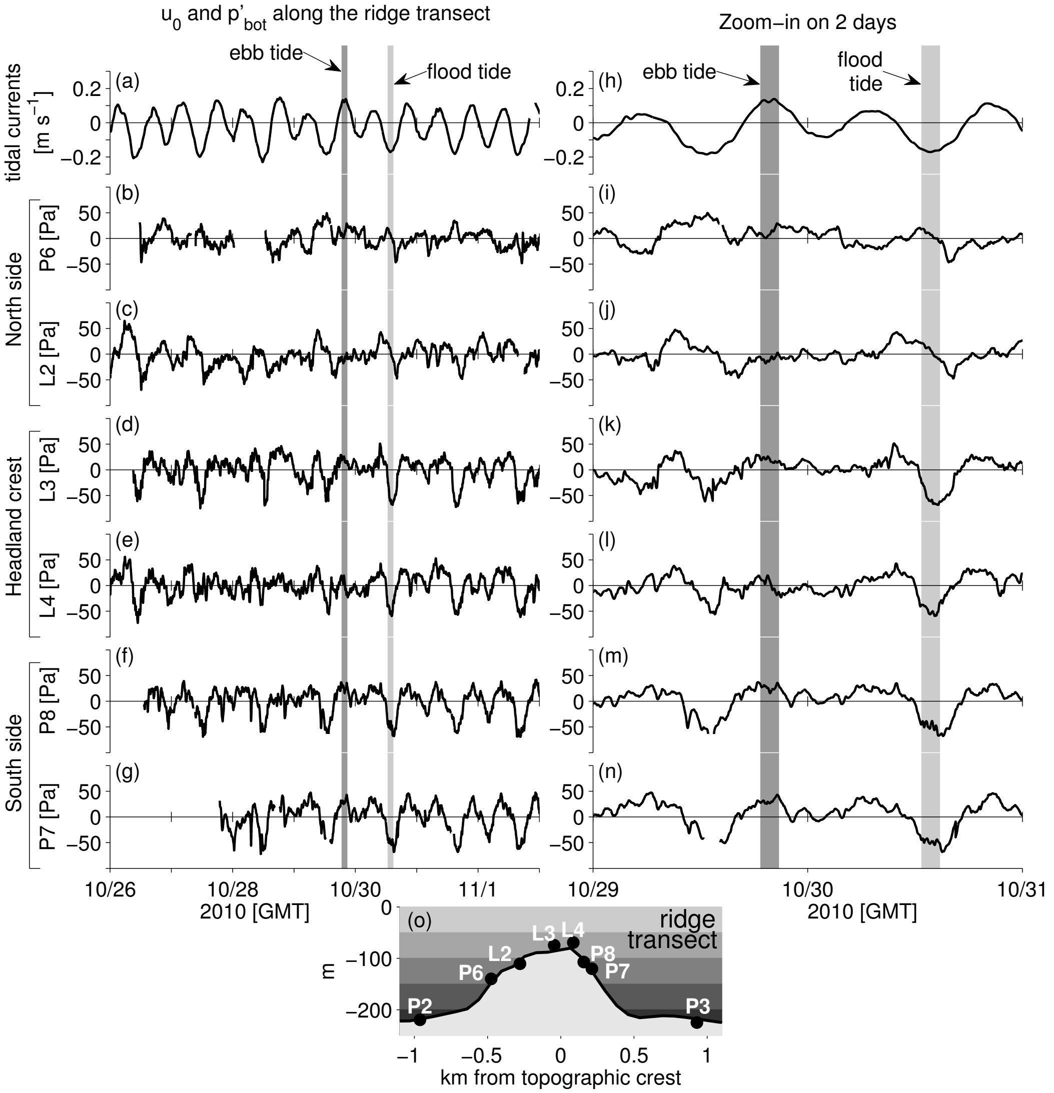

Figure 3.4: (a,h) Tidal currents. (b-g,i-n) Bottom pressure anomalies from the Ppods located along the ridge transect, arranged from north to south for the entire week-long deployment (b-g) and a zoom-in on two days (i-n). The dark (light) gray vertical line shows the time from one hour before to one hour after maximum ebb (flood) tide. (o) The locations of the Ppods.

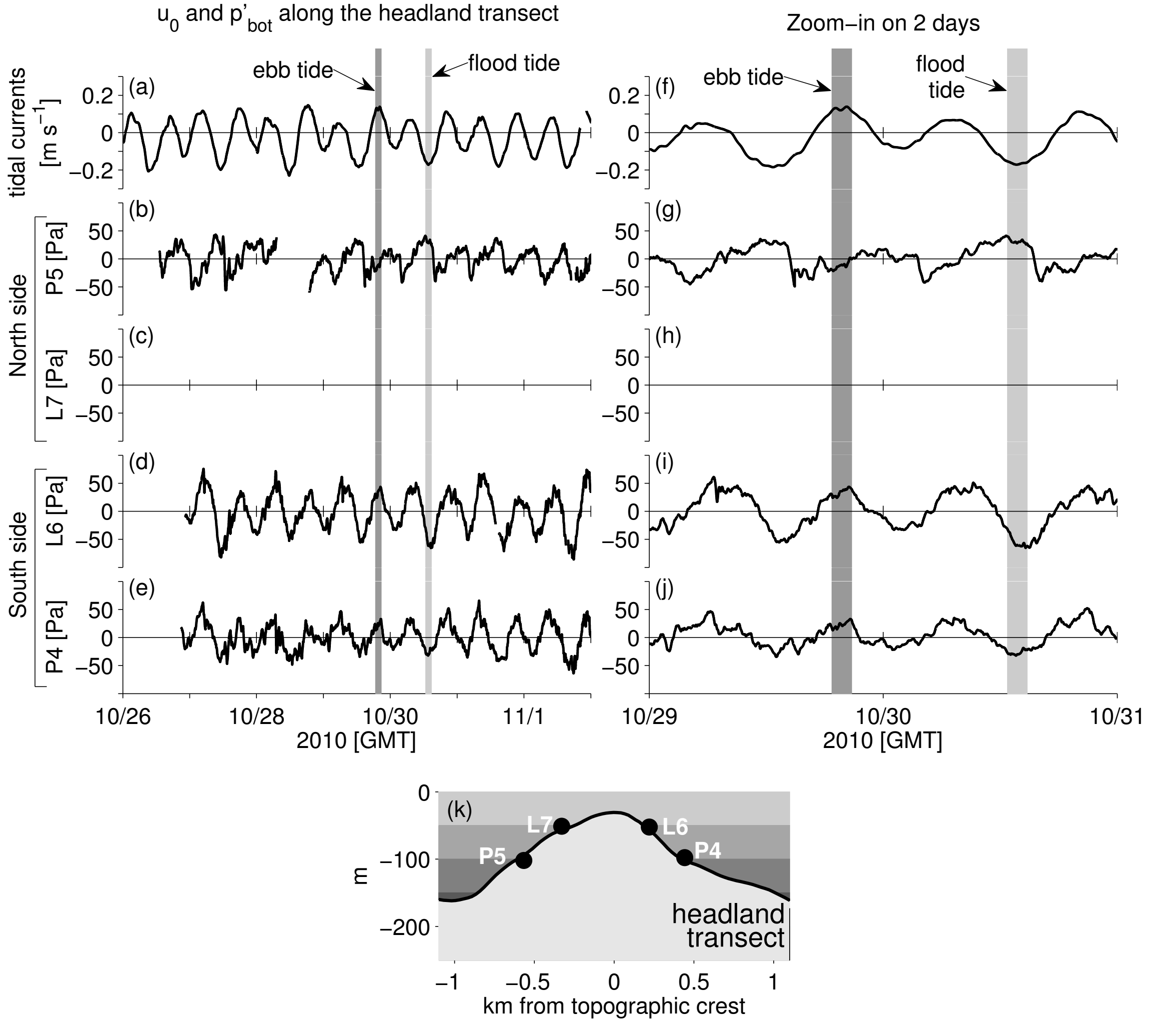

Figure 3.5: (a,f) Tidal currents. (b-e,g-j)Bottom pressure anomalies from the Ppods along the headland transect, from north to south for the entire week-long deployment (b-e) and a zoom-in on two days (g-j). The dark (light) gray vertical line shows the time period extending from one hour before to one hour after maximum ebb (flood) tide. The Ppod on lander 7 failed. (k) Locations of the Ppods.

Similar patterns of pressure anomalies are seen along the headland transect (Fig. 3.5) with high pressure on the upstream side and low pressure on the downstream

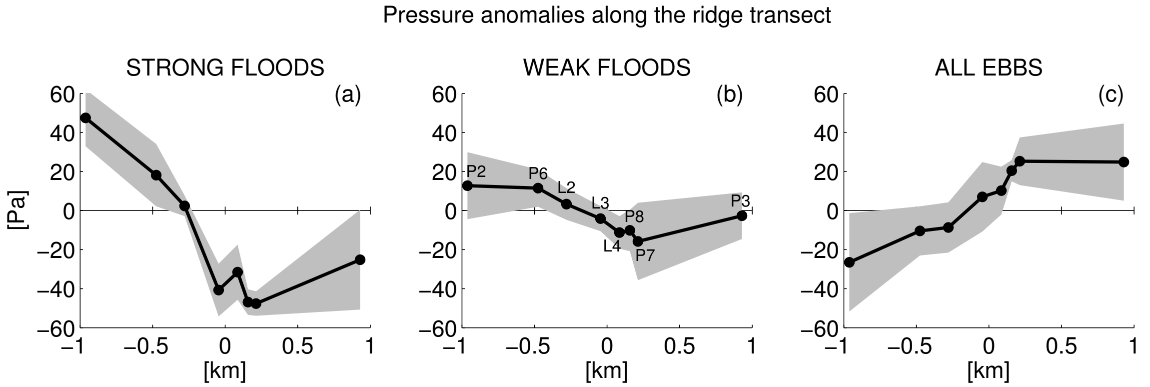

Figure 3.6: Average pressure anomalies at the Ppod locations along the ridge transect during 2-hour window spanning (a) maximum strong floods, (b) maximum weak floods, (c) and maximum ebb tides.

side of the topography.

When the bottom pressure anomalies from each Ppod along the ridge transect are plotted versus along-channel distance (Fig. 3.6), it is evident that the pressure anomaly is consistently positive on the upstream side and negative on the downstream side of the topography. Here, pressure anomalies from each Ppod are averaged over a 2-hour window spanning maximum tidal currents, and then the mean and standard deviation are calculated for the 7 strong flood, 6 week flood, and 13 ebb tides. During strong floods the difference in pressure is largest with a nearly 100 Pa drop from North to South across the topography (Fig. 3.6a). The mean pressure drops slightly in the along-channel direction during weak ebbs, but not enough to be statistically significant (Fig. 3.6b). There is an along-channel increase in pressure during ebb tides which is statistically significant (Fig. 3.6c).

3.4 Form drag from bottom pressure

3.4.1 Total form drag

Form drag can be calculated from bottom pressure anomalies using Eq. 3.1. Since the bottom pressure was only known in a few discrete locations, numerous ways of calculating the integral in Eq. 3.1 were attempted (Appendix A). Peak form drag occurs during the strong flood tides as highlighted for one tide with the vertical gray line (Fig. 3.7b,e). Along the both transects, the maximum form drag has a magnitude of 1×10^4 N m^{-1} cross-channel distance.

Power — or energy conversion rate away from the barotropic tides — is the product of form drag and tidal velocity, $P(t) = D_{form}(t)\, u_0(t)$. Large peaks in power occur during the strong flood tides with values as large as 2×10^3 W m^{-1} for both the ridge and headland transects (Fig. 3.7c,f). The average power along the ridge and headland transects is 248 W m^{-1} and 357 W m^{-1}, respectively. The power per unit area can be found by dividing the average power by the transect length. This is found to be approximately 0.2 W m^{-2} along both transects. This compares closely to the maximum barotropic to baroclinic conversion rate in a coastal canyon found by Kang and Fringer (2012). Averaged over the entire topography, an estimate for the total power is about 0.5 MW. Edwards et al. (2004) estimated an energy loss rate at TTP to be 0.72 MW. One reason for the difference between these two estimates is because this experiment was done during neap tides when there was a weak and a strong flood tide each day. During the Edwards et al. (2004) experiment, there were two strong floods each day. Since most of the drag and power loss occur during strong floods, the average power loss could double from 0.5 MW to 1.0 MW when there are twice as many strong flood tides. Furthermore, during spring tides, currents are faster which would also lead to an increased power loss.

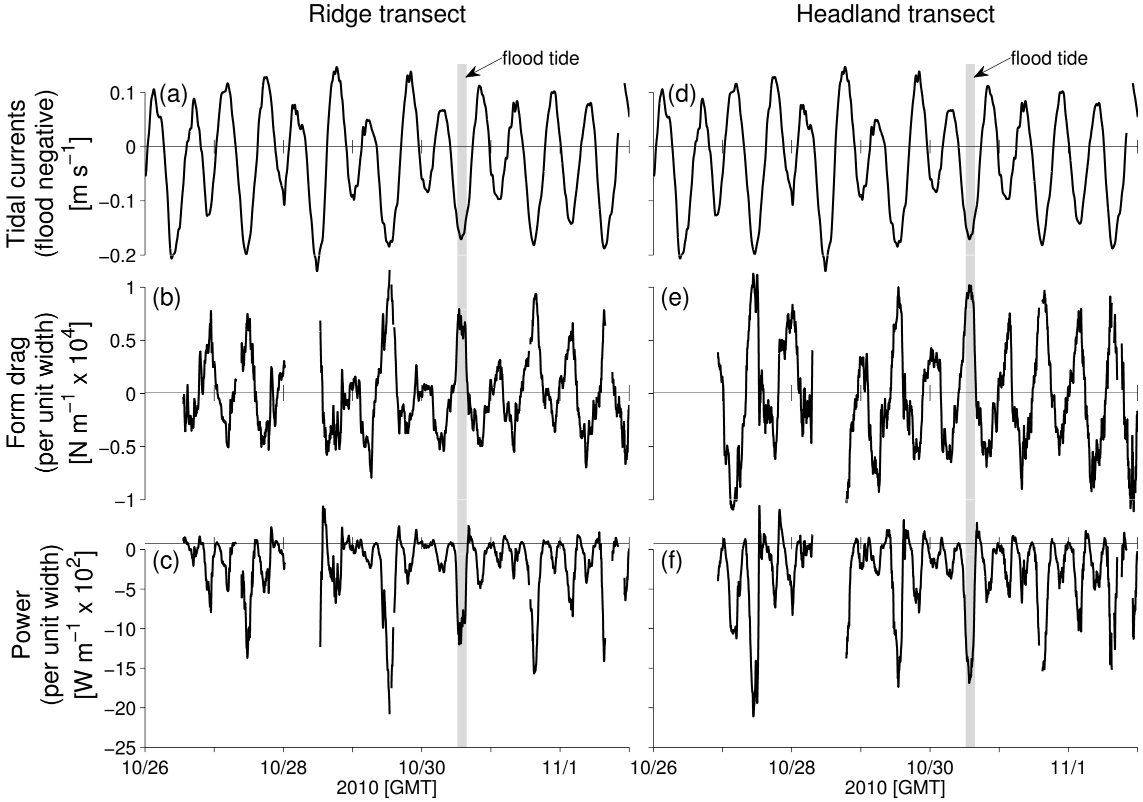

Figure 3.7: (a,d) Tidal velocity. (b,e) Form drag calculated from the Ppod bottom pressure anomalies. Form drag has units of Newtons per meter cross-channel width of the topography. Form drag has the opposite sign as the tidal currents because it is a force that opposes the flow. (c,f) Power. Power is negative because energy is being lost from the tidal currents through form drag. One of the flood tides is highlighted with the vertical gray bar. Both the form drag and power from the ridge (b,c) and headland (e,f) transects show large form drag and power during flood tides.

To put our average power estimate of 0.5 MW into context, it can be compared to the tidal energy flux calculations made by Lavelle et al. (1988) throughout Puget Sound. They estimated that the total tidal energy flux into Puget Sound is 733 MW, of which 5 MW are dissipated in East Passage, the region of Puget Sound where TTP is located. Therefore, energy losses at TTP make up 10 percent of the total losses in East Passage even though the area of TTP is only 0.6 percent of the total area of East Passage.

3.4.2 Form drag from the shallow water momentum equation

In the previous section, the form drag was calculated directly from bottom pressure anomalies. In this section, drag will again be calculated, but in a more indirect way that involves finding the drag coefficient from the shallow water momentum equation. We refer to this as the "bulk drag" as it includes both form drag and frictional drag.

To calculate the drag coefficient, C_D, start with the shallow water momentum equation in the along-channel direction with depth-integrated friction (Officer, 1976, section 3-4),

$$\frac{\partial u}{\partial t} - fv = -g\frac{\partial \eta}{\partial x} - \frac{C_D u|u|}{H}. \tag{3.6}$$

Assume no cross channel flow ($v = 0$ m s^{-1}) and an average depth ($H = 200$ m). Since this is a bulk calculation, use the background tidal velocity (u_0) for u, and calculate the sea surface height gradient with the two Ppods located at the far ends of the domain (L1 and P1). We then solve (3.6) algebraically at every time step for the drag coefficient, and then find an average drag coefficient over times when the magnitude of the velocity is greater than 0.1 m s^{-1}. This results in an average drag coefficient of $C_D = 9 \times 10^{-2}$, which is very large — about 30 times larger than the canonical frictional drag coefficient of 3×10^{-3}. However, this is not surprising because C_D includes both frictional and form drags at a location where form drag is substantially larger than frictional drag.

Using the drag coefficient $C_D = 9 \times 10^{-2}$, bulk drag and power can be calculated using a quadratic drag law

$$\frac{D_{bulk}}{W} = \frac{1}{2}\rho_0 C_D (x_{L1} - x_{P1}) u_0 |u_0| \tag{3.7}$$

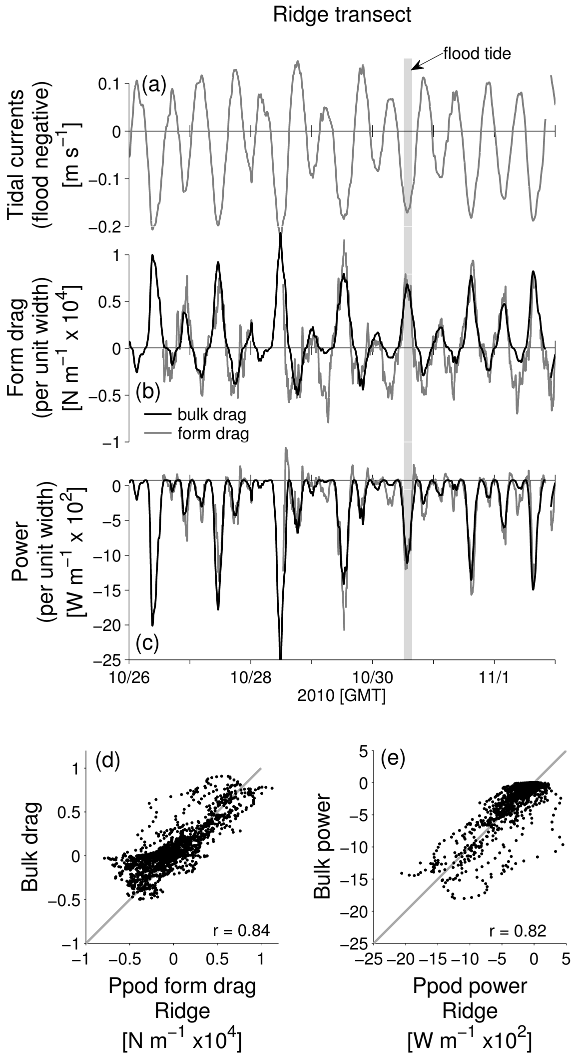

Figure 3.8: (a) Tidal velocity. (b) Form drag calculated from the Ppod bottom pressure anomalies along the ridge line (gray, same as Fig. 3.7) and the bulk drag (black). (c) Power. (d) Ppod form drag versus the bulk form drag from (b). (e) Ppod form drag power versus Bulk form drag power from (c).

where W is the cross-channel width, and x_{L1} and x_{P1} are the along-channel positions of the Ppods at the end of the domain. The total Ppod form drag and the bulk drag were calculated with completely different instruments and methods, but nonetheless they give quite similar results (Fig. 3.8). They have nearly identical magnitudes during flood and large ebb tides. During weak ebbs when the velocity is less than 0.1 m s^{-1}, the bulk drag misses some peaks. The average power for the bulk drag is 304 W m^{-1}, which agrees with the average power along the ridge and headland transects of 248 W m^{-1} and 357 W m^{-1}, respectively. The frictional drag has an average power of only 10 W m^{-1} so comparing the bulk drag to the form drag is a legitimate comparison. Despite some scatter, when the Ppod form drag and power are plotted versus the bulk drag and power most of the data falls along the 1:1 line (Figs. 3.7d,e).

In comparing the Ppod form drag to the bulk form drag, it gives us confidence that our Ppod form drag estimates are accurate. These are two independent measurements that employed different instruments and theory, but nonetheless the correlation of form drag and power between the two methods, especially during strong flood tides, is high.

3.5 Bottom pressure and form drag from potential density

3.5.1 Internal lee waves

As a comparison to the bottom pressure and form drag from the Ppods, bottom pressure and form drag can also be calculated from the Chameleon transects of potential density. This part of the pressure field is called the “internal” pressure and form drag. It gives a representation of whether the isopycnals are raised or lowered in particular parts of the domain and in certain times in the tide. First, the potential density is interpolated to a regular spatial grid. Unlike, for the Ppod bottom pressure anomalies where the background stratification in Eq. 3.4 was ignored, here it is calculated by averaging the density profiles from deep casts located far from the topography. The density anomaly (ρ') is simply the difference between the Chameleon density (ρ) and the background density ($\rho_0 + \overline{\rho}$). Then, pressure is calculated using the hydrostatic equation (Eq. 3.2), assuming zero pressure at the surface. The pressure anomaly in the deepest grid box is taken to be the internal bottom pressure anomaly.

Sections of potential density along the ridge transect for one full tidal cycle show lee waves on the downstream side of the topography (Fig. 3.9). Associated with these lee waves are low bottom pressure anomalies both from the Ppods and from vertical integrals of potential density. The bottom pressure anomalies from the Ppods were averaged over the time period of the Chameleon transect, which was approximately one hour long.

Examining the density and bottom pressure anomalies over a tidal cycle (Fig. 3.9) shows the evolution of the internal lee waves. The sequence starts at the very end of a small flood tide (Fig. 3.9a) when the tidal velocity is nearly zero. At this time, the Ppod bottom pressure anomalies are nearly zero and there is a slight tilt of the isopycnals with higher internal bottom pressure anomalies on the south side. At time 2 (Fig. 3.9b), the currents have started to ebb (flow to the north). There are slightly higher Ppod bottom pressure anomalies on the south side of the headland (P8 and P7), but there is little change in the density field. At time steps 3 and 4 (Fig. 3.9c,d), the flow is strongly ebbing and the isopycnals show a lee wave that is situated above the topography just to the north of the topographic crest. At both of these time steps, the Ppod bottom pressure anomalies show a higher pressure on the upstream side of the topography (L4, P8 and P7) than on the downstream side (P6 and L2). The internal bottom pressure anomalies have a much larger magnitude than the Ppod bottom pressure anomalies. This discrepancy is likely due to sea surface height displacements which are accounted for by the Ppods but not by the density. By time step 5 (Fig. 3.9e), the ebb tide has slackened, but some residual signals

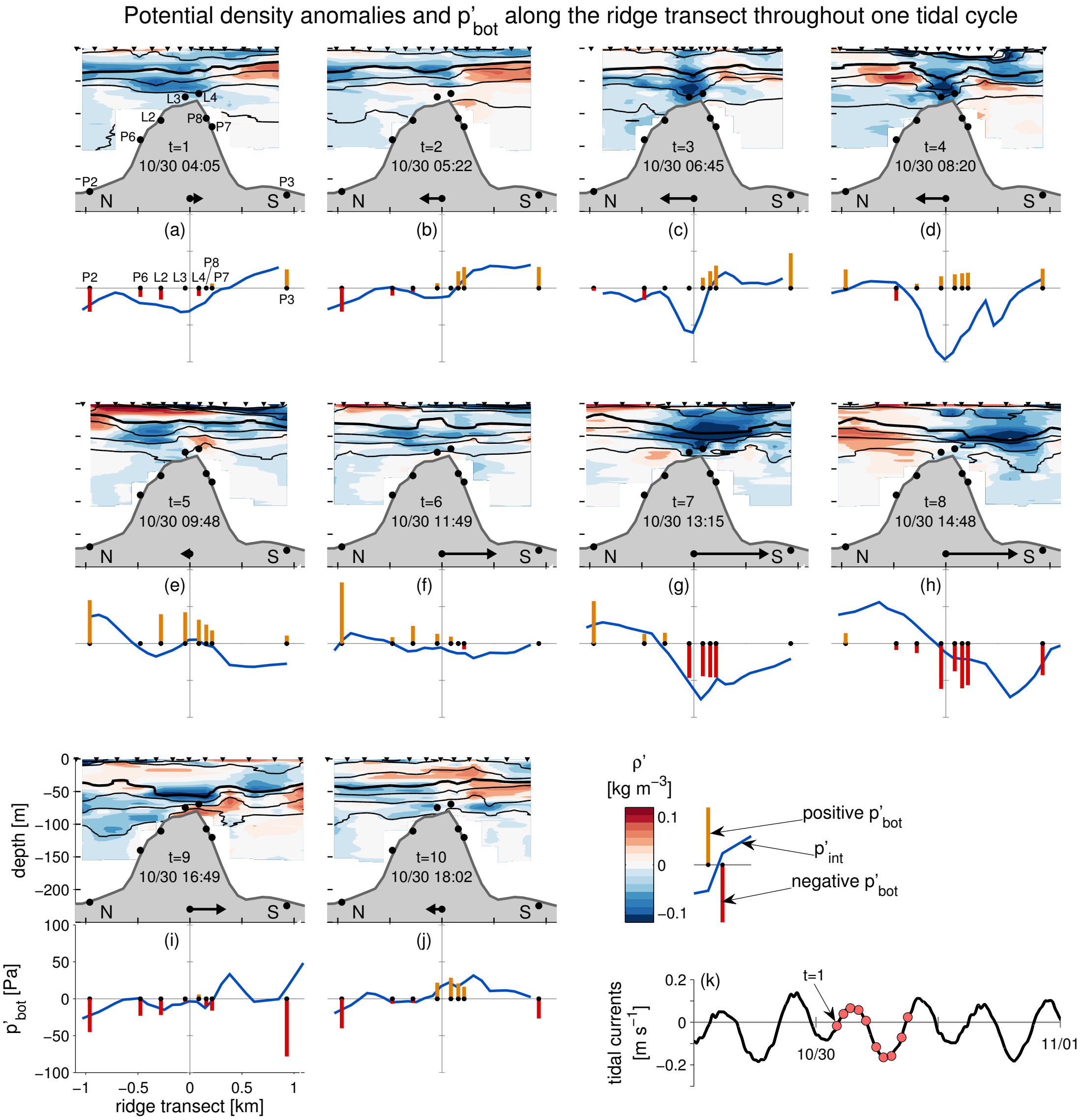

Figure 3.9: (a–j top) Potential density anomalies (red/blue gradient) overlaid with contours of density at intervals of 0.1 kg m^{-3} with the 1023 kg m^{-3} isopycnal in bold. Also shown are Ppods (black dots), Chameleon drops (black triangles), and tidal currents (black arrows). (a–j bottom) Bottom pressure anomalies from Ppods and density. (k) Tidal currents highlighting the 10 time-steps (red dots).

remain.

The tide is flooding in time steps 6 through 9 (Fig. 3.9f-h). In time step 6, however, there are almost no bottom pressure perturbations either from the Ppods or the potential density. The large bottom pressure anomaly at P2 is most likely caused by a sea surface height perturbation traveling away from the topography. In time steps 7 and 8 (Fig. 3.9g,h), there is a large pressure difference across the topography both from the Ppods and potential density. Just as was seen in Fig. 3.4, the two Ppods on the crest of the topography (L3 and L4) and the two on the downstream side (P8 and P7) all have large negative pressure anomalies at maximum flood tide. Internal lee waves can be seen in the potential density section. By time step 9 (Fig. 3.9i), the flood tide has slackened. At time step 10 (Fig. 3.9j), the tide has begun to ebb again and the cycle will repeat itself. Throughout the experiment, similar patterns to these 10 time steps are seen at flood, ebb and slack tides.

Differences between the total (Ppod) and internal (Chameleon density) bottom pressure anomalies in Fig. 3.9 are caused by a number of factors. First, the Ppods include external and nonhydrostatic pressure perturbations whereas the Chameleon density does not. This is the sources of the largest discrepancies. Additionally, the Chameleon density profiles only go to 160 m, missing as much as 40 m of the water column in the deep parts of the transect. Time variability may also create small differences. In Fig. 3.9, the Ppod pressure anomalies have been averaged over the hour it took to complete the transect, whereas each individual Chameleon profile takes only 5–10 minutes.

3.5.2 Form drag from potential density

The internal form drag can be calculated from the potential density bottom pressure anomalies (Fig. 3.10). A continuous integration method (Appendix A) is used to integrate the internal bottom pressure anomalies across the topography.

On the ridge transect, the internal form drag and power peak during strong flood tides just as seen for the total form drag and power. The average power from the internal drag is 209 W m^{-1} (0.16 W m^{-2}), which accounts for about 80 percent of the total power along the ridge transect (248 W m^{-1} or 0.21 W m^{-2}).

Scatter plots of Ppod form drag and power versus internal form drag and power (Fig. 3.10g,h) show a good correlation between the two data sets. However, the strong correlation between Ppod form drag and internal form drag only exists during flood tides ($r = 0.79$ during flood tides, $r = 0.29$ during ebb tides).

Along the headland transect, a CTD was used to collect density data at four stations along the transect. This was not enough spatial coverage to resolve isopycnal height variations. The internal form drag and power do not correlate with the total form drag and power (Fig. 3.10e, f, i, j).

This discrepancy between internal and total form drag along the headland transect highlights the importance of a CTD that continually samples like the Chameleon profiler. A sensitivity test was performed to determine how many CTD casts are necessary to get an accurate estimate of the internal form drag by subsampling the Chameleon profiles. For instance, if only half the Chameleon casts are used to calculate internal form drag, the results are essentially the same as if every cast is used. However, if every fourth cast is used, the results start to deviate, and if fewer are used, the results become meaningless. It also matters where the casts are taken. If a cast is made in the middle of an internal wave, the results will be good, but if big features like that are missed, the final result could be erroneous.

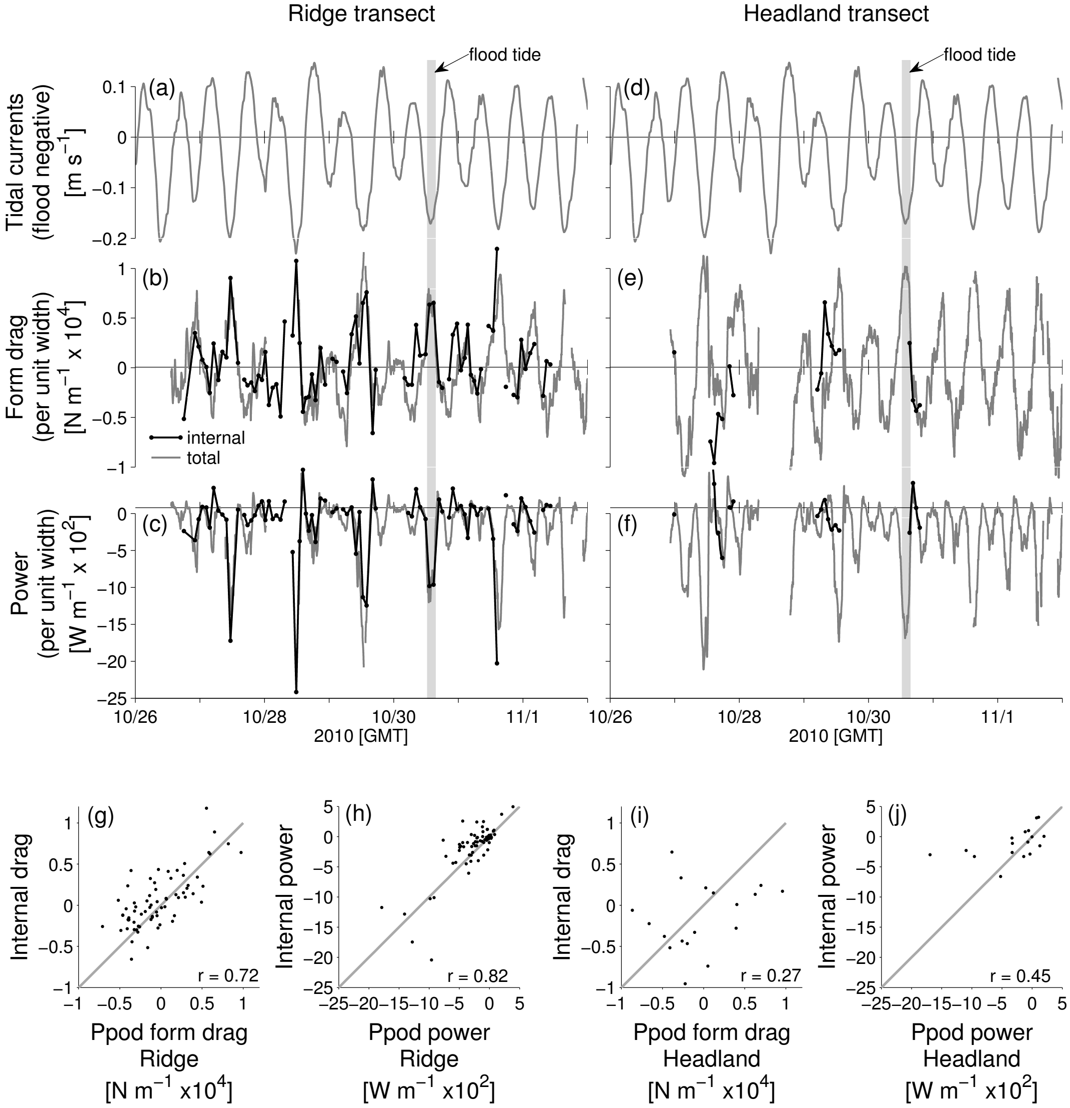

Figure 3.10: (a,d) Tidal velocity. (b,e) Total form drag from Ppod bottom pressure anomalies (gray) and internal form drag from potential density sections (black). Each Chameleon transect is indicated with a black dot. (c,f) Power. (g-j) Scatter plots comparing internal form drag (g,i) and power (h,j) to the total form drag along the ridge (g,h) and headland (i,j) transects.

3.6 Turbulent kinetic energy dissipation rate

The Chameleon profiler also measures turbulent kinetic energy dissipation rate (Fig. 3.11). During both flood (Fig. 3.11f-h) and ebb tides (Fig. 3.11c,d), increased dissipation is seen on the lee side of the topography. Maximum energy dissipation rates of 5×10^{-5} W kg^{-1} were measured during peak flood tides (Fig. 3.11g). The dissipation is quite patchy. It was found that ninety percent of the dissipation occurs in only 20-30 percent of the volume. It is also obvious from the microstructure measurements that form drag causes dissipation throughout the water column, unlike frictional drag which only dissipates energy in the bottom boundary layer.

Dissipation can be spatially integrated along the ridge transect at each time step, which can be compared to the total power from the Ppods (Fig. 3.12a). The form drag power has distinct peaks at flood tides, whereas peaks in dissipation rate are not nearly as large. This discrepancy is also visible when viewed as a scatter plot (Fig. 3.12b). At peak floods, the spatially integrated dissipation is only 25-50 percent as big as the total power. This confirms that not all of the energy is dissipated locally, but instead is carried away from the topography by internal waves and eddies.

3.7 Velocity surveys

Shipboard and bottom lander ADCP velocities were collected along the two transects (Fig. 3.13). At ebb tide (Fig. 3.13a), the background tidal current flows from the SSE. Along the ridge transect, the currents on the south side of the headland are deflected towards the center of the channel by the topography, and on the headland transect, the currents are even deviated somewhat southward. Currents reach speeds of 0.5 m s^{-1} on the south side of the topography, with the strongest velocities at 20 m depth. On the north side of the topography during ebb tide, the currents are weak. The velocities close to TTP are much faster than tidal currents in the center of the

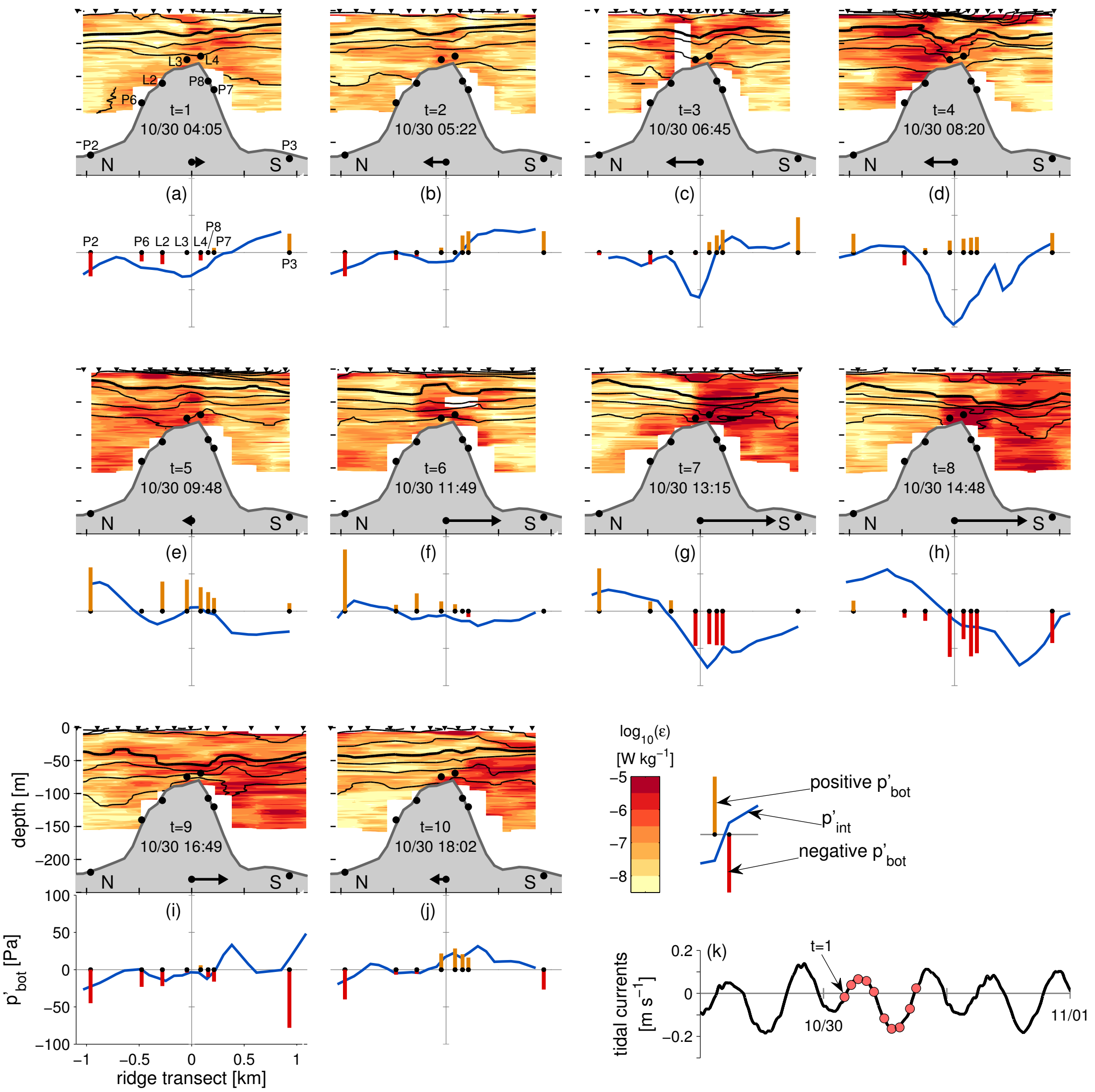

Dissipation and p'_{bot} along the ridge transect throughout one tidal cycle

Figure 3.11: (a–j top) Turbulent kinetic energy dissipation rate (red/orange gradient) at the same times as Fig. 3.9. Isopycnals are shown with black contours at intervals of 0.1 kg m^{-3} with the 1023 kg m^{-3} isopycnal in bold. (a–j bottom) Total and internal bottom pressure (Fig. 3.9). (k) Tidal currents highlighting the 10 time-steps (red dots).

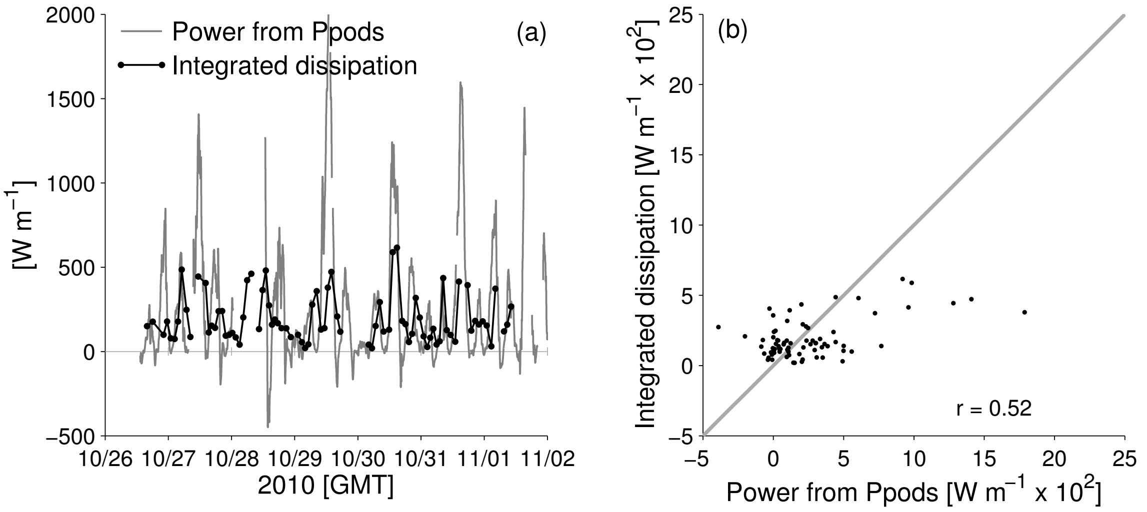

Figure 3.12: (a) Spatial integral of turbulent kinetic energy dissipation rate (black line and dots) compared to the total power (gray line, negative of Fig. 3.7c). Both are in units of W m^{-1} cross-channel distance. (b) Scatter plot comparing the total power (x-axis) to the integrated dissipation (y-axis).

channel which reach speeds of only 0.2 m s^{-1} during the strongest flood tides.

The currents near TTP never completely stop due to the presence of lingering eddies and other local dynamics. At slack tide (Fig. 3.13b), the currents are weaker than those at flood or ebb, but are still nearly 0.2 m s^{-1} which is as fast as the tidal current at maximum flood.

At flood tide (Fig. 3.13c) when the background current is flowing from the NNW, the currents near TTP are deflected strongly by the topography. On the north side of the headland along the ridge transect, the currents are deflected towards the center of the channel at all depths. On the south side of the topography, the evidence of an eddy can clearly be seen (Fig. 3.13c). At the very south ends of the two transects, the currents are deflected strongly to the east. Just south of the tip of TTP along the headland transect, the currents are flowing back towards the west. This flow pattern

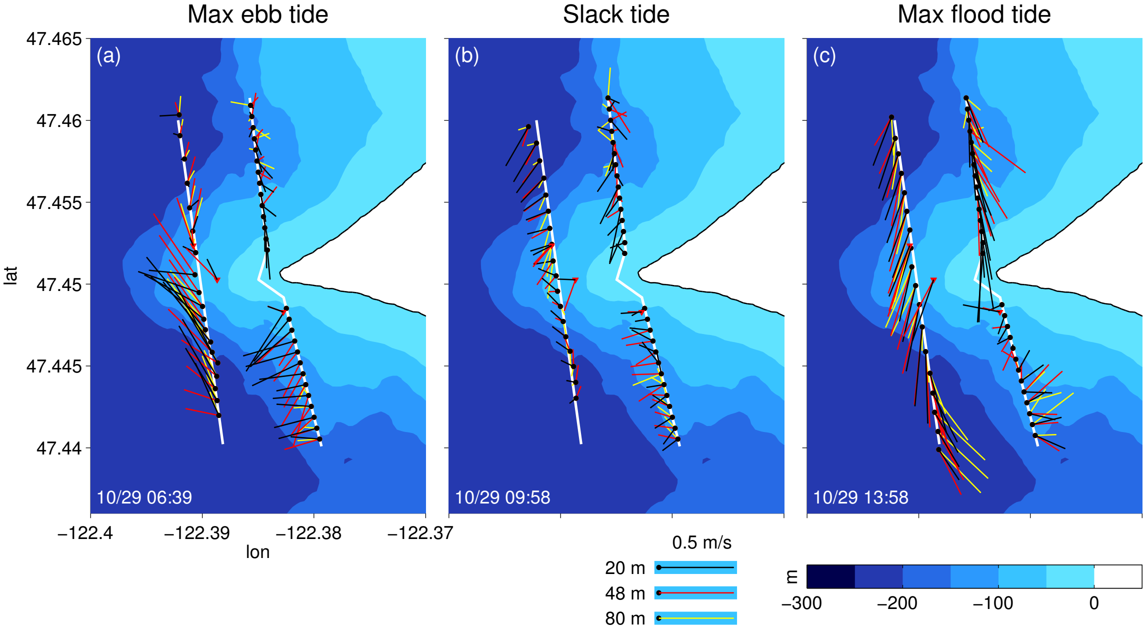

Figure 3.13: Plan views of velocity at three depths (20m, 48m, and 80m) at maximum ebb (a), slack (b), and maximum flood (c) tides.

has the distinct characteristics of a lee eddy that is spinning counterclockwise.

The sea surface height deformation associated with this eddy can be estimated. For simple, rotational flow, the frictionless, steady shallow water momentum equation can be written in polar coordinates as,

$$-\frac{u_\theta^2}{r} - fu_\theta = -g\frac{\partial\eta}{\partial r} \tag{3.8}$$

where u_θ is the angular velocity, r is the radius of the eddy, and $\frac{\partial\eta}{\partial r}$ is the gradient of sea surface height in the radial direction. Assuming that $u_\theta \approx 0.3$ m s^{-1} at $r \approx 500$ m, then the sea surface height difference between the center of the eddy and the edge is 10.5 mm (105 Pa), with the center being lower than the edge. On the north side of the headland where the eddy spins in the clockwise (anticyclonic) direction, the sea surface height deformation would be only 7.5 mm because the Coriolis force term has the opposite sign as the centripetal acceleration term. These sea surface deformations are of the same order of magnitude as the pressure perturbations measured by the Ppods.

3.8 Inertial pressure and form drag

In (3.5), the dynamic bottom pressure anomaly measured by the Ppods is divided into internal, external, inertial and nonhydrostatic parts. The inertial pressure was included as a separate term in (3.5) because it arises from different physical processes than the external and internal pressures. WM09 showed that when the flow is unsteady, form drag is not only created by flow separation which leads to the generation of internal waves and eddies, but it is also created simply by the oscillatory nature of the flow.

We can gain insight into the inertial part of the pressure field by thinking about potential flow (Dean and Dalrymple, 1984). By definition, steady potential flow does not create form drag because it is reversible; there is no flow separation. Oscillatory potential flow is also reversible, but form drag is created by an along-channel pressure gradient that accelerates the flow. In an estuary, this manifests itself as a slope, or “tilt”, of the sea surface. At flood and ebb tides, the sea surface is essentially flat, whereas at slack tide, the sea surface is sloped downwards in the direction of tidal acceleration. This creates a pressure difference across the topography which results in form drag even without flow separation. Inertial drag will be most important in cases where the tidal excursion distance is nearly the same as the topographic length (WM09). It should be noted that the sea surface slope is related to the acceleration of the flow and not when high and low tides occur. Therefore, the theory for inertial drag is the same whether the estuary has a tidal wave that is progressive or standing.

In this study, since the domain is only a few kilometers long, the sea surface slope associated with tidal acceleration is assumed to be linear. The sea surface height at a given location is calculated from the tidal acceleration:

$$\eta_{tilt}(x,t) = \frac{1}{g}\frac{\partial u_0}{\partial t}(x - x_0) \tag{3.9}$$

where u_0 is the background tidal velocity, x_0 is a reference location, and x is the along-channel distance from the reference location. To calculate the inertial pressure, Eq. 3.9 can be substituted into Eq. 3.5. It makes most sense to choose the reference location at the center of the topography, however, when calculating form drag using Eq. 3.1, as long as the same reference location is always used, it does not matter where it is located. Alternately, if pressure sensors are located upstream and downstream of the topography, η_{tilt} can be calculated from the along-channel pressure gradient:

$$\eta_{tilt}(x,t) = \frac{1}{\rho_0 g}\frac{p_A - p_B}{x_A - x_B}(x - x_0) \tag{3.10}$$

where A and B indicate locations of pressure sensors up- and downstream of the topography. In a frictionless system, this would give the exact same answer as Eq. 3.9. We choose to define η_{tilt} as in Eq. 3.9 so that the inertial form drag is in perfect quadrature with the velocity. Therefore, even though η_{tilt} creates form drag, it does not do tidally-averaged work on the flow. All of the form drag that does tidally-averaged work on the flow is contained within the external and internal pressure anomalies (Eq. 3.5).

WM09 found that on headlands comparable to the size of TTP, the inertial form drag can be comparable in size to the form drag caused by flow separation. Therefore, it is important to calculate it in this oscillatory tidal case.

The local sea surface height associated with the background tilting of the sea surface is calculated at each Ppod location with Eq. 3.9. That height is converted to a bottom pressure anomaly using Eq. 3.5. Then the inertial form drag is calculated

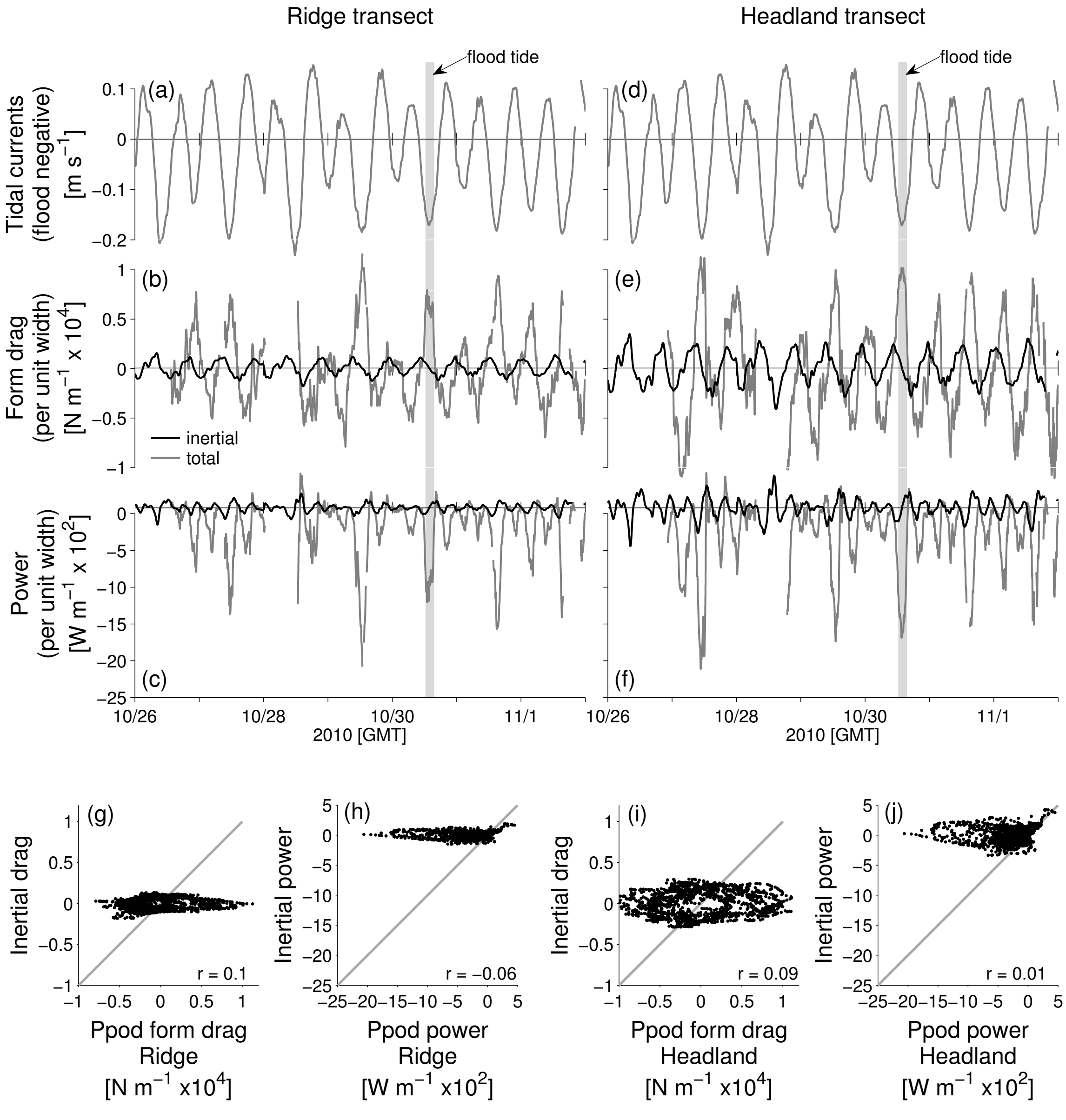

Figure 3.14: (a,d) Tidal velocity. (b,e) Total form drag (gray) and inertial form drag (black). (c,f) Power. (g-j) Ppod form drag and power (x-axes) versus inertial form drag and power (y-axes).

from Eq. 3.1 in the piecewise integration method (Appendix A). At maximum flood and ebb tides, the inertial form drag is zero, but at slack tide, when the acceleration is biggest, the inertial form drag has its maximum value (Fig. 3.14).

The amplitude of the inertial form drag is significantly smaller than the amplitude of the total form drag along both the ridge (Fig. 3.14b) and headland transects (Fig. 3.14e). This contrasts the results of WM09, but was not entirely unexpected because their study was for headlands with vertical side walls which is not the case for TTP. Inertial drag for a ridge is not expected to be as large as the inertial drag for a headland because the topographic slope ratio for a ridge is usually only 1:10 (rise:run) whereas for a headland it is more like 1:1 (across-channel extent:along-channel extent).

Most importantly, even though the inertial form drag and instantaneous power are not zero, the average power of the inertial drag *is* zero (Fig. 3.14c, f). The inertial drag does no net work on the flow. There is almost no correlation between the inertial form drag and power and total form drag and power along either transect (Fig. 3.14g-j).

3.9 Comparisons and parameterizations

TTP is complex because it generates both internal waves like a ridge and eddies like a headland as tidal currents flow over and around it. For the most part, in oceanography, the flow dynamics over ridges and around headlands have been investigated separately.

For the headland case, WM09 found that the form drag on idealized headlands was well predicted by a bluff body drag law:

$$D_{BB} = \frac{1}{2}\rho_0 C_D A_P u_0 |u_0| \tag{3.11}$$

where C_D is an $O(1)$ drag coefficient. The projected frontal area of the headland can be written as $A_P = W h_0$, where W and h_0 are the topographic width and height, respectively. Bluff body drag is commonly used to estimate form drag on a wide variety of objects in non-stratified flow for which drag coefficients have been experimentally found (Fox and McDonald, 1998, chap. 9).

Stratified flow over ridges is a complex problem that has been studied extensively. Gill (1982, chapters 6 & 8) and Baines (1995) explain variations of the steady case in their books. Garrett and Kunze (2007) review oscillatory flow over ridges in the deep ocean. They define a non-dimensional parameter space that is based on the steepness ($\epsilon = kh_0/(\frac{\omega^2-f^2}{N^2-\omega^2})^{1/2}$), tidal excursion ($kU_0/\omega$), nonlinearity ($Nh_0/U_0$), and height ($h_0/H$). To get an idea of where TTP fits within this parameter space, the following physical dimensions are used: buoyancy frequency ($N = 1.5 \times 10^{-2}$ s^{-1}), Coriolis frequency ($f = 1 \times 10^{-4}$ s^{-1}), amplitude of the tidal velocity ($U_0 = 0.2$ m s^{-1}), frequency of the M2 tides ($\omega = 1.4 \times 10^{-4}$ s^{-1}), water depth ($H = 200$ m), and height of the topography along the ridge transect ($h_0 = 115$ m). For an isolated ridge like TTP, we follow Legg and Huijts (2006) and define the topographic wavenumber as $k = 1/L = 1.5 \times 10^{-3}$ m^{-1} where $L = 660$ m is the Gaussian e-folding length of the topography. It is found that TTP has a steepness parameter of $\epsilon = 40$ which means the topographic slope is supercritical with respect to the wave ray slope. The tidal excursion parameter, $kU_0/\omega = 2.1$, which means that the flow in this region is likely to produce quasi-steady lee waves. The nonlinear parameter, $Nh_0/U_0 = 8.6$, which means that the flow over TTP could be blocked by the topography. Finally, the height parameter, $h_0/H = 0.58$, which means that the channel depth is comparable with the topography. It should also be noted that the flow at TTP is not likely hydraulically controlled as its Froude number $U_0/(N(H - h_0)/\pi) = 0.49$.

The values of these nondimensional parameters puts TTP in a case of being quasi-steady, finite depth, supercritical slope, and nonlinear. This part of parameter space is likely to be common in high-latitude coastal regions. Similar ridges have been studied with nonhydrostatic models (Nakamura et al., 2000; Legg and Huijts, 2006) and by observations of two-layer, hydraulically-controlled ridges (Armi, 1986; Farmer and Armi, 1999a). Due to the nonlinearity of this ridge case, no theories have been developed which can predict the wave drag that should be seen at TTP. Comparisons can be made to steady theory (Gill, 1982; Baines, 1995), oscillatory theory for subcritical slopes in infinite depths (Bell, 1975a,b), theories with adjustments for finite depth (Khatiwala, 2003), theories with adjustments for steep topography (Balmforth et al., 2002; Llewellyn Smith and Young, 2003; St. Laurent et al., 2003; Pétrélis et al., 2006), and theories for steady flow over corrugated slopes and isolated ridges on a slope (Thorpe, 1992, 1996; MacCready and Pawlak, 2001). However, since none of these theories are for topography in the same parameter space as TTP, in this paper, a simple wave drag parameterization for an isolated "Witch of Agnesi" ridge with small Nh_0/U_0 in infinite depth fluid will be used (Baines, 1995, p. 245):

$$D_{wave} = \frac{\pi}{8}\rho_0 N u_0 W h_0^2. \tag{3.12}$$

It is advantageous to use a simple theory as opposed to a more complicated one because if it can be validated, it can then be more easily implemented into larger scale numerical models.

Using these two drag parameterizations (Eqs. 3.11 and 3.12), the size of the drag at TTP can be put into perspective (Fig. 3.15). Here, the mean and standard deviation of form drag and power have been calculated over velocity bins of 0.01 m s^{-1}. The bluff body drag ($C_D = 1$) under-predicts the form drag and power. The linear wave drag does a better job. A more complicated wave drag law that takes into consideration the oscillatory nature of the flow and the relative shallow depth of the water might be more appropriate, but as a first approximation, this simple parameterization in (3.12) does quite well over the range of velocities observed at TTP.

In previous experiments at TTP, the form drag was found to be as much as seven

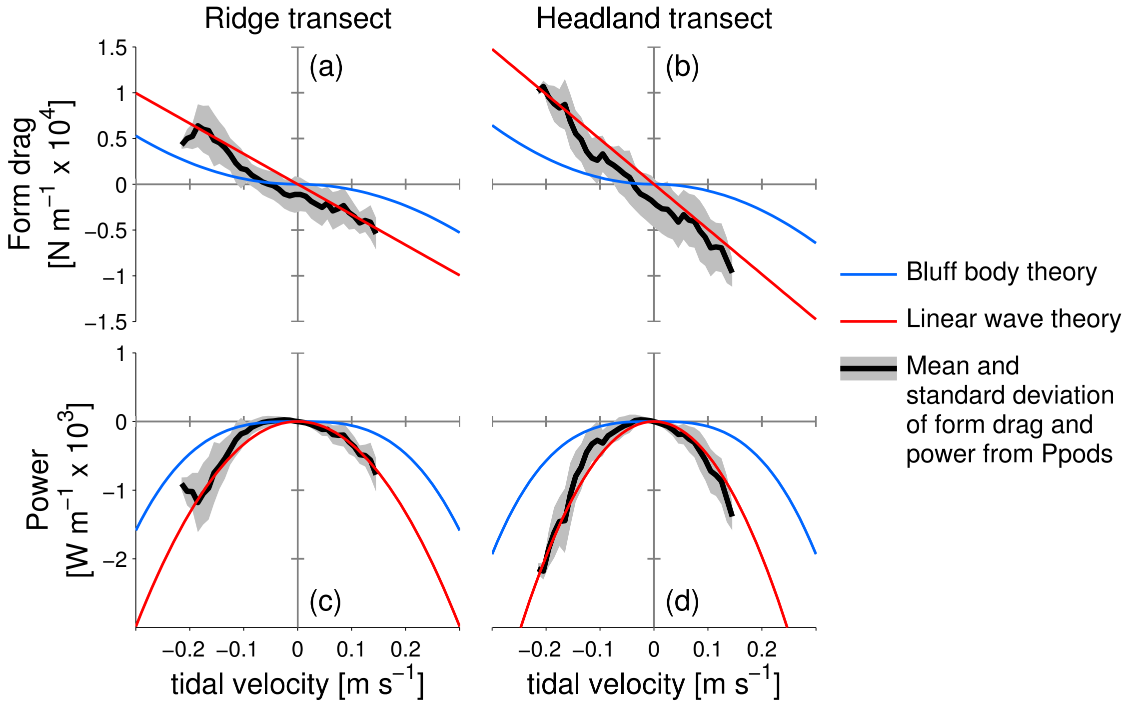

Figure 3.15: Scatter plots that show the correlations between tidal velocity and form drag (a-d) and power (e-h) along the two transects for both the total and internal form drags. Theoretical parameterizations of drag and power from the bluff body drag law (light gray line) and from the linear wave drag theory (dark gray line) are shown in each subplot.

times larger than predicted by bluff body drag with an $O(1)$ drag coefficient (Edwards et al., 2004; McCabe et al., 2006). It was hypothesized that TTP was incredibly good at generating drag, possibly due to its shape or the fact that the tidal excursion distance is nearly the same as the topographic length. WM09 suggested that the increased drag was due to the oscillatory nature of the flow creating inertial drag. In this study, we again show that the form drag at TTP is much larger than predicted by bluff body drag. However, now we conclude that it is not due to the inertial drag which was shown to be quite small in section 3.8. Nor is it due to the tidal

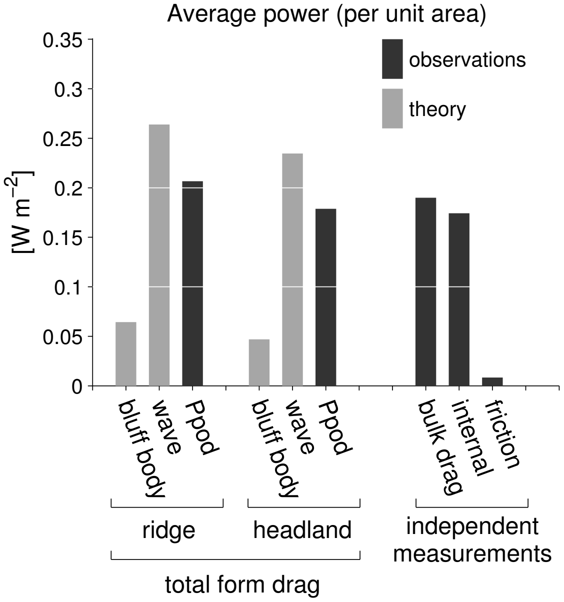

Figure 3.16: Average power that has been calculated in many ways throughout this paper. The two theoretical powers (gray) are from the bluff body drag law (Eq. 3.11) and the linear wave drag law (Eq. 3.12). The observed powers (black) from the Ppod form drag along the ridge and headland transects compare a lot better to the wave drag than to the bluff body drag. The average power from the bulk drag, the internal drag along the ridge transect, and bottom friction are also shown.

excursion distance or shape of TTP. Instead, it is simply that a wave drag law is a more appropriate parameterization than a bluff body drag law since the flow at TTP is stratified and internal waves are generated.

The under-prediction of the form drag at TTP by the bluff body drag law can also be seen when comparing tidally-averaged power along the two transects (Fig. 3.16). Bluff body drag only accounts for about a third of the power measured by the Ppods. The wave drag does a much better job. It over-estimates the power measured by the Ppods by about 25 percent. This over-estimation is due largely to error at low velocities rather than at high velocities when drag is larger.

In addition to comparing the the Ppod power to theories, it can be compared to independent measurements such as the bulk drag power (section 3.4.2) and internal drag power (section 3.5). The bulk drag has an average power of 0.19 W m $^{-2}$, which compares well with the average Ppod power along the ridge (0.21 W m $^{-2}$) and headland transects (0.18 W m $^{-2}$). The internal power is about 80 percent of the total form drag power along the ridge line. Since the pressure from the Ppods contains internal, external and nonhydrostatic pressure, we would expect that the internal form drag would be smaller than the total form drag. In a numerical model of the region, there is evidence that along the ridge transect the total form drag is mostly made of internal form drag whereas closer to shore, the external form drag begins to play a much larger role (chapter 4 of thesis). Finally, the energy loss due to bottom friction (0.008 W m $^{-2}$) pales in comparison to the losses due to form drag. This further justifies the fact that models which only use a frictional drag coefficient to parameterize drag in regions of rough topography are going to miss a large part of the drag and energy loss.

3.10 Conclusion

There were three goals of this project. First, to assess whether form drag can be measured directly using seafloor pressure sensors. Second, to parameterize the form drag using existing theory. Third, to describe the flow field at TTP, so that the mechanisms that create drag can be more fully understood.

We were able to measure the form drag on TTP with bottom pressure sensors. The form drag from the Ppods was confirmed by comparing it to drag derived from the shallow water momentum equation ("bulk" drag). Both methods find an average power loss due to form drag of about 0.2 W m^{-2}. Furthermore, both methods showed that the form drag and power have their biggest magnitude during the strong flood tides due to the asymmetry of the strength of the tides (floods are faster than ebbs) and to the asymmetry of the topography (the south side is steeper than the north).

For the second goal, it was shown that the form drag is 30 times larger than the frictional drag. Furthermore, due the stratification and ridge-like properties of TTP, a bluff body drag law with an $O(1)$ drag coefficient drastically underestimates the form drag. A linear wave drag law gives a much better prediction of the form drag and power. It was also shown that the inertial drag was much smaller than the total form drag which is different from what was predicted by WM09 for headlands with vertical side walls.

For the third goal, physical mechanisms associated with form drag generation were observed: eddies were seen in the velocity data, internal waves in the potential density data, and elevated levels of turbulent kinetic energy dissipation rates in the microstructure data. The power losses due to the internal form drag were 80 percent as big as those from the total form drag. Maximum values of the spatially-averaged dissipation were 25-50 percent as big as the form drag power during strong flood tides.

Overall, even though TTP only accounts for a very small percentage of the energy dissipation in Puget Sound or the world's oceans, the form drag power losses at TTP are 30 times larger than frictional losses over a equivalent flat area. Therefore, it is important that form drag — not just frictional drag — is taken into consideration in larger scale numerical models. Furthermore, form drag causes energy dissipation throughout the water column, not just in the bottom boundary layer. So simply increasing the bottom friction in numerical models to account for topographic form drag may not lead to momentum and energy losses in the correct locations.

3.11 Appendix A: Error analysis

3.11.1 Ppod pressure errors

In section 3.3, it was explained how the bottom pressure anomalies are calculated from the total Ppod pressure. There are a few sources of error involved in this calculation that need to be elaborated upon.

First, it is possible that removing the shifts (section 3.3) resulted in errors because aligning the pressure anomalies before and after each sink was done visually. However, these would not be larger than a few Pa, and therefore not likely to affect the form drag integral substantially.

A second source of error is due to drifting clocks. This is what rendered the pressure from Lander 7 unusable. It is essential that the clocks are all aligned and keep accurate time because even small differences in timing can result in falsely large pressure anomalies when the background tidal height is subtracted. As an example, if the clock on a Ppod is off by 20 seconds, due simply to the rate of change of $\rho_0 g\bar{\eta}$, the pressure anomalies can be incorrect by 50 Pa. This is the same order of magnitude as the pressure anomalies that create form drag and therefore a very serious problem. All of the other Ppods had newer software than L7 and therefore not prone to this problem. However, it is something that one must be very careful about when measuring form drag in locations where tidal height changes rapidly.

In section 3.3.2, the mean and standard deviation of the bottom pressure anomaly from each Ppod at different points in the tidal cycle was shown in Fig. 3.6. There is a fair amount of variability from one tidal cycle to the next, which is due in part to natural variability of the maximum tidal velocity during each flood and ebb. However, there is still statistically significant along channel pressure slope during the strong floods and ebbs, which shows that despite this variability, the pressure signals are robust enough to trust our form drag calculations.

3.11.2 Three form drag integration methods

Since Ppods were only located at a few distinct locations along the two transects, multiple ways of calculating form drag with Eq. 3.1 were attempted to see how much sensitivity there is to integration method.

The first method was the simplest: one Ppod from each side of the topography was used. On the ridge transect, the Ppods used were L2 on the north and P8 on the south. The slope was estimated as a constant value of $s = 0.23$ which was taken as positive on the north and negative on the south. A constant x-distance was of $l = 500$ m was also used for each side. Essentially this method assumes that TTP is shaped like an isosceles triangle with a bottom length of 1000 m and height of 115 m. The form drag was integrated as:

$$D_{\text{form (average)}} = -\left[p_{L2} s l + p_{P8}(-s) l\right]. \tag{3.13}$$

Along the headland transect, the Ppod on the north was P5 and on the south was L6. The average slope and x-distance were 0.165 and 750 m, respectively.

The second method involved piecewise integration across the topography. To do this, discrete sections which traced the shape of the topography were used (Fig. 3.17). The average slope (s_1, s_2, etc.) of each section was multiplied by the bottom pressure anomaly from the Ppod located within each section and then summed along the length of the transect (l_1, l_2, etc.). Along the ridge transect, three sections were used and along the headland transect, four sections were used (Fig. 3.17). It is essential that the form drag integral start and end at the same depth (MacCready et al., 2003). The end depth was chosen to be 200 m on the ridge transect and 150 m on the headland transect. For this method, the form drag along the ridge transect was integrated as:

$$D_{\text{form (piecewise)}} = -\left[p_{P6} s_1 l_1 + p_{L2} s_2 l_2 + 0.5(p_{P8} + p_{L7}) s_3 l_3\right]. \tag{3.14}$$

There were three caveats to this method. First, along the ridge transect, the average pressure from P7 and P8 was used in a single section because they sat so close to each other. Second, along the headland transect, P7 failed, so P5 was used instead. Third, the pressures from P2, L3, L4, and P3 were not used because they sat in regions with near-zero topographic slope.

The third method for calculating form drag involved a more continuous integration along the transects. The ridge was broken into 80 points spaced about 25 m apart. The pressure was linearly interpolated from the two Ppods closest to every point:

$$p_{\text{interp}} = p_{\text{up}} \frac{l_{\text{down}}}{l_{\text{up}} + l_{\text{down}}} + p_{\text{down}} \frac{l_{\text{up}}}{l_{\text{up}} + l_{\text{down}}}. \tag{3.15}$$

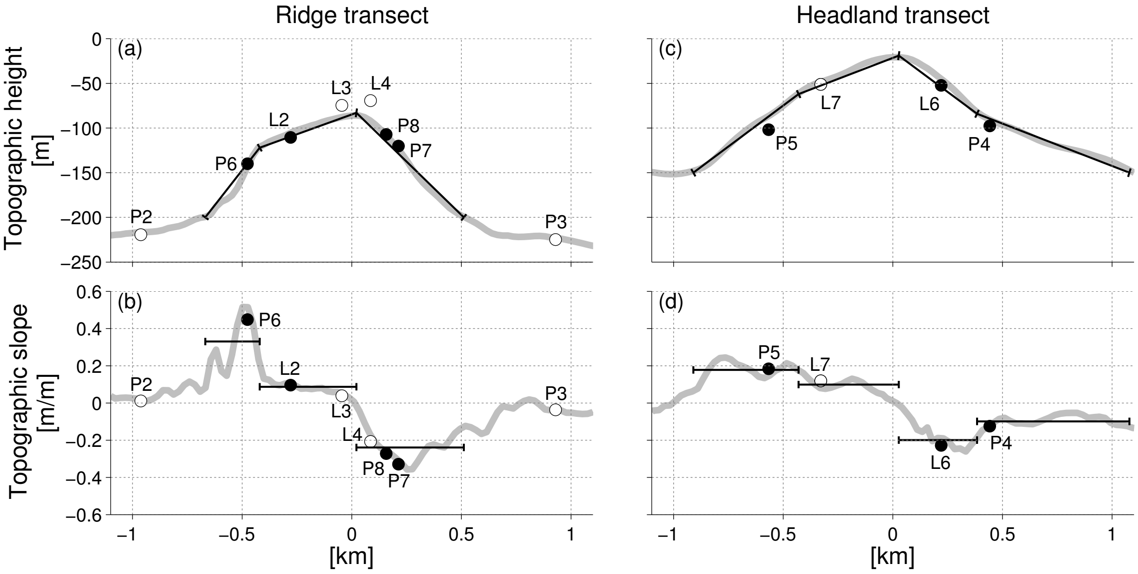

Figure 3.17: The locations of the Ppods along the topography on the ridge (a) and headland (c) transects, and the corresponding slopes (b,d). The segments that were used to calculate form drag (thin black lines) were chosen to match the topographic height and slope (thick gray lines) as best as possible. Black dots indicate Ppods that were used in the form drag calculation and white dots indicate Ppods that were not used in form drag calculations.

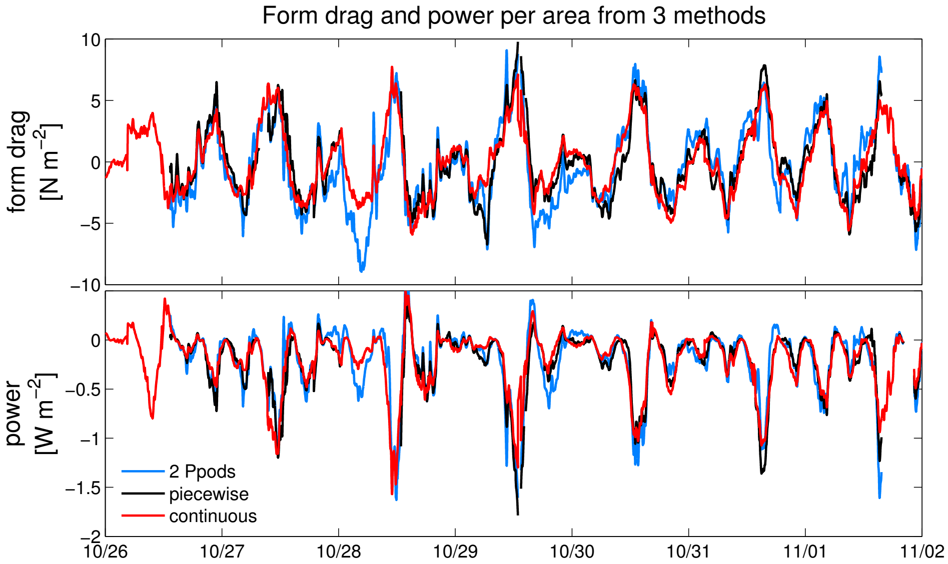

Figure 3.18: Form drag and power calculated using three different methods of integration of bottom pressure and slope across the topography. The 2 Ppods method takes the pressure and slope from each side of the topography. The piecewise method breaks the topography into discrete sections each containing one Ppod. The continuous method linearly interpolates the pressure along the transect before integrating.

Here, p_{up} and p_{down} are the pressures at the upstream and downstream Ppods located closest to a given point and l_{up} and l_{down} are the distances from that point to the upstream and downstream Ppods, respectively. The slope was calculated from the shipboard ADCP bottom-track depth. Once the pressure and slope were calculated at each point along the transect, Eq. 3.1 could be used directly.

Overall, these three methods give very consistent results for form drag and power (Fig. 3.18). In Fig. 3.18, the form drag and power have been divided by the transect length because the transect length differs slightly between the three methods. The average power for the three methods calculated over the same time period are also nearly the same at 0.216 W m^{-2}, 0.219 W m^{-2}, and 0.211 W m^{-2} for the 2 Ppod, piecewise, and continuous methods, respectively.

The consistency between the three methods shows that no matter how form drag is integrated, the calculation is robust. It is possible that the location of the Ppods missed some "hot spots" of form drag generation, which would lead to an underestimate of form drag. However, due to the similarity between the three methods of form drag integration that used either 2, 4, or 8 Ppods, it also shows that most likely there were enough Ppods deployed across the topography to get an accurate estimate of form drag. Throughout the paper, the piecewise method will be used.

Chapter 4

THE DYNAMICS OF PRESSURE AND FORM DRAG ON A SLOPING HEADLAND: INTERNAL WAVES VERSUS EDDIES

In the ocean, topography that generates internal waves and topography that generates eddies are usually studied separately. Here, a numerical model is used to understand the dynamics that occur as tidal currents flow around Three Tree Point, a 1 km long, 200 m deep, sloping headland that generates both internal lee waves and eddies. Bottom pressure anomalies due to isopycnal and sea surface perturbations are calculated. These are known as the internal and external pressure anomalies, respectively, and their sum is known as the dynamic pressure anomaly. From the pressure anomalies, form drag and energy conversion from the barotopic tides can be calculated. The internal lee wave create internal pressure anomalies of -66 Pa during maximum flood tide. The corresponding external pressure anomalies are near-zero. For the eddy, an external pressure anomaly of -129 Pa is created by a sea surface depression that balances the centripetal force of the eddy's currents. A corresponding internal pressure anomaly of 122 Pa is created as isopycnals are lifted to counteract the sea surface depression. Therefore, the dynamic pressure anomaly of the eddy is near-zero except in regions shallower than 50 m where the isopycnals cannot adjust to counteract the sea surface depression. There, the external pressure is -61 Pa. Even though the magnitude of the internal and external pressure anomalies from the eddy are twice as big as those from the internal lee waves, due to canceling within the eddy, the dynamic pressure anomalies across the topography are between 50 and

75 Pa, and the internal waves and eddies do similar amounts of work on the flow. Topography like Three Tree Point is common in high-latitude, coastal regions, and therefore the finding here have implications for drag parameterizations in large scale numerical models.

4.1 Introduction

Form drag is an important process that is known to dissipate energy and momentum as tidal currents flow over rough topography. It is especially relevant in coastal regions where tides are relatively fast and rough topography is abundant. Unlike frictional drag which is well parameterized within numerical models, form drag is still not fully understood.

This study explores the bottom pressure and form drag that result as tidal currents flow over and around Three Tree Point (TTP), a headland in Puget Sound, WA that is typical of topography found in high latitude regions. The sloping nature of TTP gives rise to both eddies and internal waves, which are two processes that have traditionally been studied separately. Topographically generated eddies have been observed (Pingree and Maddock, 1979; Geyer and Signell, 1990; Li et al., 2006; White and Wolanski, 2008), modeled (Black and Gay, 1987; Signell and Geyer, 1991; Warner and MacCready, 2009; Callendar et al., 2011), and studied in the laboratory (Boyer and Tao, 1987; Klinger, 1994; Cenedese and Whitehead, 1999; Pawlak and MacCready, 2002) in cases where eddies are created in the absence of internal waves. A wide range of topographically generated internal waves are described by Baines (1995), who details steady theory, and by Garrett and Kunze (2007), who review internal tide generation in the deep ocean. TTP differs from these due to the relatively shallow water depth compared to the topographic height and the time-dependent currents which have a tidal excursion distance that is nearly the same as the topographic length. Studies of internal waves that are most comparable to TTP include numerical models of tidal flow over topography (Nakamura et al., 2000; Legg and Huijts, 2006) and observations of hydraulically controlled tidal flow over Knight Inlet (Farmer and Armi, 1999a,b; Klymak and Gregg, 2001, 2003). In particular, at Knight Inlet, Klymak and Gregg (2001) show that the interaction between recirculating flow on the lee side of Knight Inlet can enhance the internal waves. However, due to the hydraulically controlled flow and cross-sill density gradients, the circulation at Knight Inlet is different from what is observed at TTP which has Froude numbers below 1 and a background stratification that is spatially constant within the domain.

TTP is chosen for this study because it is typical of topography found in high-latitude coastal regions, it is subjected to predictable tidal currents, and it has been researched extensively in the past. Edwards et al. (2004) measured density fields over the ridge-like part of TTP and quantified the internal form drag, which is the part of the total form drag that arises from isopycnal height anomalies. McCabe et al. (2006) measured the velocity field surrounding TTP from which they inferred the sea surface height and quantified the external form drag, which is the part due to sea surface height anomalies. In chapter 3 of this thesis, an array of bottom pressure sensors was used to measure the total form drag, which includes both the internal and external form drags. The dynamics at TTP have also been investigated theoretically. MacCready and Pawlak (2001) developed a theory for form drag generated by steady, stratified flow over an idealized ridge on a sloping side wall. Warner and MacCready (2009) developed a theory for tidal flow past headlands that explains why form drag can be very large in oscillatory flow situations. The tilted headland eddy that is created in the lee of TTP has been explored by Pawlak et al. (2003), who details its time evolution, and by Canals et al. (2009), who describe the isopycnal structure resulting from the eddy tilt. Overall, TTP generates significant amounts of form drag. It is much larger than frictional drag over a flat bottom of equivalent area (Edwards et al., 2004). Even the form drag itself has been found to be bigger than what is predicted by a quadratic drag law with an $O(1)$ drag coefficient acting on the projected frontal area (chapter 3).

A lot of known about the dynamics at TTP, however, because observations cannot map the entire flow field, it is not fully understood how the complex interaction of the internal lee waves and the tilted eddy generate form drag as tidal currents flow over and around this sloping headland. In this study, a numerical model of TTP was used to dissect the pressure field into the parts relevant to form drag to understand how internal lee waves and eddies create form drag and to determine which creates larger pressure anomalies and more form drag.

The model and the theoretical description of how the pressure field is dissected is presented in section 4.2. In section 4.3, the internal waves and eddies are described using maps of bottom pressure anomalies. Finally, in section 4.4, the form drag due to the internal waves and eddies is quantified and discussed. A conclusion follows in section 4.5.

4.2 Methods

4.2.1 Model setup

The TTP model was developed using the Regional Ocean Modeling System (ROMS) (Shchepetkin and McWilliams, 2005), a free-surface, hydrostatic, primitive equation numerical model. It covers an area of the Main Basin of Puget Sound, which encompasses the channel where TTP is located (Fig. 4.1c). The model has 100 m horizontal resolution throughout the domain and 20 terrain-following vertical levels that are unevenly spaced with higher resolution near the surface and bottom. The minimum depth was set to be 3 m to avoid wetting and drying of cells. Bathymetric height was collected during a shipboard survey with a side-scanning multibeam echosounder which provided 5 m resolution of the region close to TTP. Further afield, the bathymetry was from the Puget Sound gridded 27 m bathymetry (Finlayson, 2005). The bathymetry was smoothed to avoid excessively steep slopes (Fig. 4.1e).

The TTP model was one-way nested within the 2006 MoSSea Model (Sutherland et al., 2011), a regional model of the Salish Sea and the Oregon, Washington, and British Columbia coasts (Fig. 4.1a). The TTP model was run from October 24, 2006 to October 31, 2006, which is at the same time of year as a 2010 companion field study (chapter 3) so stratification was expected to be similar (Appendix A). Tidal currents were also predicted to be nearly the same during the two time periods by a tidal model of Puget Sound (Lavelle et al., 1988). During both the observation and model periods, the tidal regime is shifting from spring to neap, and the tides are mixed semidiurnal (Appendix A). The initial condition and boundary conditions for the TTP model were taken from hourly output of the MoSSea Model and interpolated to the TTP model grid. This provided tidal forcing and stratification of incoming water to the TTP model. No atmospheric forcing was used in the TTP model. Turbulence closure was set to be the k–ϵ version of the generic length scale mixing formulation (Umlauf and Burchard, 2003) with Canuto-A stability (Canuto et al., 2001). A quadratic drag law with $C_D = 3 \times 10^{-3}$ was used to parameterize bottom stress, and free-slip conditions were used on the vertical walls. At the open boundaries, the free-surface used Chapman boundary conditions (Chapman, 1985), the depth-averaged momentum used Flather boundary conditions (Flather, 1976), and all other fields used radiation boundary conditions. All of these parameters were chosen to match what was used in the MoSSea Model (Sutherland et al., 2011). The six rows of grid points closest to the open boundaries were nudged to background values with a time scale of 0.1 days for salinity and temperature and 0.5 days for momentum to avoid

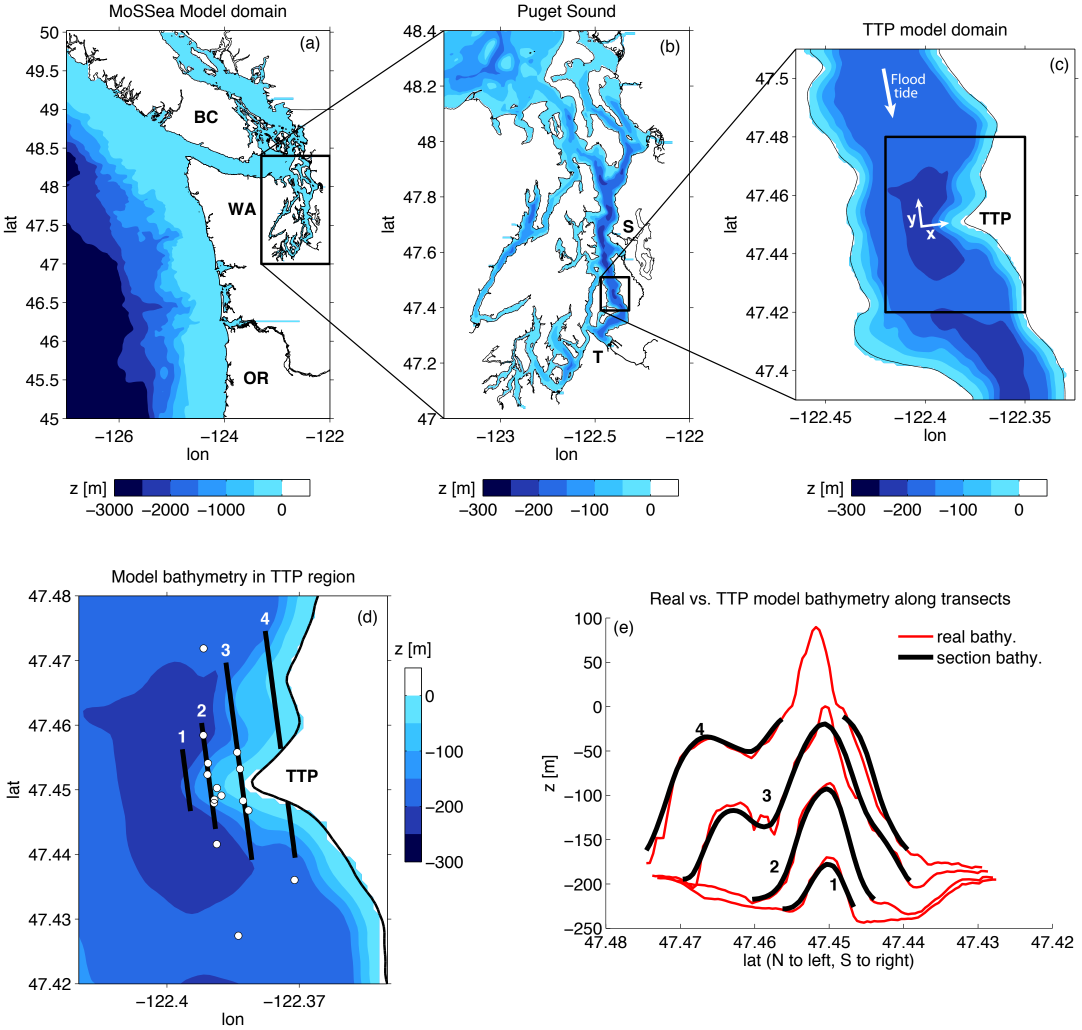

Figure 4.1: (a) MoSSea Model domain and bathymetry. (b) Puget Sound. TTP is located about half way between the cities of Seattle (S) and Tacoma (T). (c) TTP model domain and bathymetry. The x-y coordinate axes are aligned with the across- and along-channel directions. (d) TTP model bathymetry with the four analysis transects. The locations of the bottom pressure sensors (white dots) used in the field study (chapter 3). (e) Bathymetric height along the four transects viewed as if looking from the center of the channel toward shore with north to the left, showing real bathymetry (red) and model bathymetry (black).

reflection of waves off of the open boundaries. Snapshots of the flow field were saved every 15 minutes of model time.

4.2.2 Pressure decomposition

The pressure within the model can be divided into parts that do and do not contribute to form drag. ROMS is a hydrostatic model, so to decompose the pressure, we begin with the hydrostatic equation:

$$\frac{\partial p}{\partial z} = -\rho g \tag{4.1}$$

where $p = p(\mathbf{x}, t)$ is pressure, $\rho = \rho(\mathbf{x}, t)$ is density, g is gravity, $\mathbf{x} = (x, y, z)$, and t is time. The coordinates are oriented along the channel, with positive y in the ebb direction and z positive up (Fig. 4.1c). The density can be divided into three parts, $\rho(\mathbf{x}, t) = \rho_0 + \overline{\rho}(z, t) + \rho'(\mathbf{x}, t)$, where ρ_0 is a constant background density, $\overline{\rho}(z, t)$ is the spatially-averaged stratification at every time step, and $\rho'(\mathbf{x}, t)$ is the residual. Substituting the density decomposition into Eq. 4.1 and integrating from a vertical position, z, to the surface height η gives:

$$p(\mathbf{x}, t) = g\rho_0\eta - g\rho_0 z + g\int_z^\eta \overline{\rho}(z, t)\, dz + g\int_z^\eta \rho'(\mathbf{x}, t)\, dz. \tag{4.2}$$

The sea surface height can also be decomposed:

$$\eta(x, y, t) = \overline{\eta}(t) + \eta_{inertial}(y, t) + \eta_{KW}(x, t) + \eta'(x, y, t). \tag{4.3}$$

Here, $\overline{\eta}(t)$ is the domain-averaged sea surface height that varies with the tides. $\eta_{inertial}(y, t)$ is an along-channel sea surface height gradient that causes the acceleration of the tides,

$$\eta_{inertial}(y, t) = \frac{1}{g}\frac{\partial v_0}{\partial t}(y - y_0), \tag{4.4}$$

where y_0 is a reference location at the center of the channel and y is the along-channel distance from the reference location. The tidal velocity, v_0, flows in the along-channel direction and was calculated from a spatial average of currents from regions about a km to the north and south of TTP. $\eta_{inertial}(y,t)$ is largest at slack tide and is nearly zero at maximum flood and ebb tides. It is included as a separate term because Warner and MacCready (2009) show that this background tilting of the sea surface can account for form drag that has a large amplitude, but does not do tidally-averaged work on the flow because its phase is in quadrature with the velocity. $\eta_{KW}(x,t)$ is a cross-channel tilt of the sea surface that arises as the tidal wave propagates downstream along the channel banks as a Kelvin wave (approximated with a linear tilt because the channel is much narrower than the barotropic Rossby radius):

$$\eta_{KW}(x,t) = \frac{f}{g} v_0 (x - x_0). \tag{4.5}$$

Here, f is the Coriolis frequency and x_0 is a reference location in the center of the channel. It cannot affect form drag because it varies perpendicularly to the flow. However, it is included as a separate term to isolate the dynamically active part of the sea surface height field, $\eta'(x,y,t)$.

By substituting Eq. 4.3 into 4.2, the following expression for pressure is obtained:

$$p = \underbrace{g\rho_0\overline{\eta}}_{\text{tides}} + \underbrace{g\rho_0\eta_{inertial}}_{\text{*inertial}} + \underbrace{g\rho_0\eta_{KW}}_{\text{Kelvin wave}} + \underbrace{g\rho_0\eta'}_{\text{**external}} - \underbrace{\rho_0 g z}_{\text{depth}} + \underbrace{g\int_z^{\eta} \overline{\rho}\, dz}_{\text{backgr. strat.}} + \underbrace{g\int_z^{\eta} \rho'\, dz}_{\text{**internal}}\,. \tag{4.6}$$

In this equation, only the starred terms contribute to form drag. The sum of the internal and external pressures (double stars) will be called the dynamic pressure because it is the part of the pressure field that does work on the flow and is associated with internal waves and eddies. The dynamic pressure from the model and field study (chapter 3) show similar patterns with respect to the tidal currents (Appendix A).

4.2.3 Calculating form drag

Form drag is the spatial integral of seafloor pressure times topographic slope,

$$D_{\text{form}} = -\int_{A_0} p'_{bot}\,\zeta_y\,dA_0 \tag{4.7}$$

where A_0 is the bottom area, ζ is the topographic height, and ζ_y is the topographic slope in the along-channel direction. The bottom pressure anomaly, p'_{bot}, includes the parts of Eq. 4.6 that contribute to form drag, evaluated at the sea floor. The form drag can also be calculated with any individual parts of the bottom pressure anomaly to get the "inertial drag," "external drag," "internal drag," and "dynamic drag." The power extracted from the tides by the form drag is simply the product of the form drag and the tidal velocity,

$$P = D_{\text{form}} v_0 \tag{4.8}$$

Four transects that run parallel to the channel were chosen on which to calculate form drag and perform detailed analysis (Fig. 4.1d). The transects were specifically chosen to encompass the parts of topography with non-zero slopes and to end at equal depths (Fig. 4.1e). They are numbered 1 through 4 from offshore to onshore. Transect 2 and 3 correspond to the ridge and headland transects in the observations, respectively (chapter 3). The form drag and power from the model and observations along transect 2 exhibit similar patterns of largest energy conversion during strong flood tides (Appendix A). Form drag is integrated using the pressure and slope at every grid box along each transect. In the observations (chapter 3), pressure was only measured at discrete locations. In Appendix B, we show that form drag calculated from a full integral and from discrete locations gives similar results.

4.3 Dissecting the pressure field: Physical mechanisms that create form drag

As discussed in section 4.2.2, the bottom pressure anomaly can be divided into the internal, external, dynamic, inertial, Kelvin wave, and total pressures, all of which have different physical relevance (Figs. 4.2, 4.3). The goal of this section is to dissect the pressure fields to calculate where and how the internal and external pressures act in tandem or against each other and do determine which physical processes are most important in the creation of form drag.

There are consistent patterns of pressure seen at TTP. During flood tide (Fig. 4.2), there are large internal, external and dynamic bottom pressure anomalies. The inertial bottom pressure is zero and the Kelvin wave pressure has its maximum across-channel gradient. Similar, but reversed, patterns are seen during ebb tide. However, since ebb currents are so much weaker than flood currents, this analysis focuses on the flood tide. During slack tide (Fig. 4.3), there are still large internal and external pressure anomalies in the domain due to the persistence of an eddy that was created during the previous flood tide. At this time, the internal pressure field has its largest along-channel gradient and the Kelvin wave pressure is zero.

4.3.1 Eddies

Eddies are an obvious feature in the vicinity of TTP, most easily seen by patches of high relative vorticity (Fig. 4.2g). During flood tide, vorticity is shedding off the tip of TTP, and is advected southward by the tidal currents. This patch of strong positive vorticity carries with it a much-weaker patch of negative vorticity that was left from the previous ebb tide.

Due to the fact that the eddies are being created by sloping topography, the eddies themselves are tilted (Canals et al., 2009). The position of the eddy can be

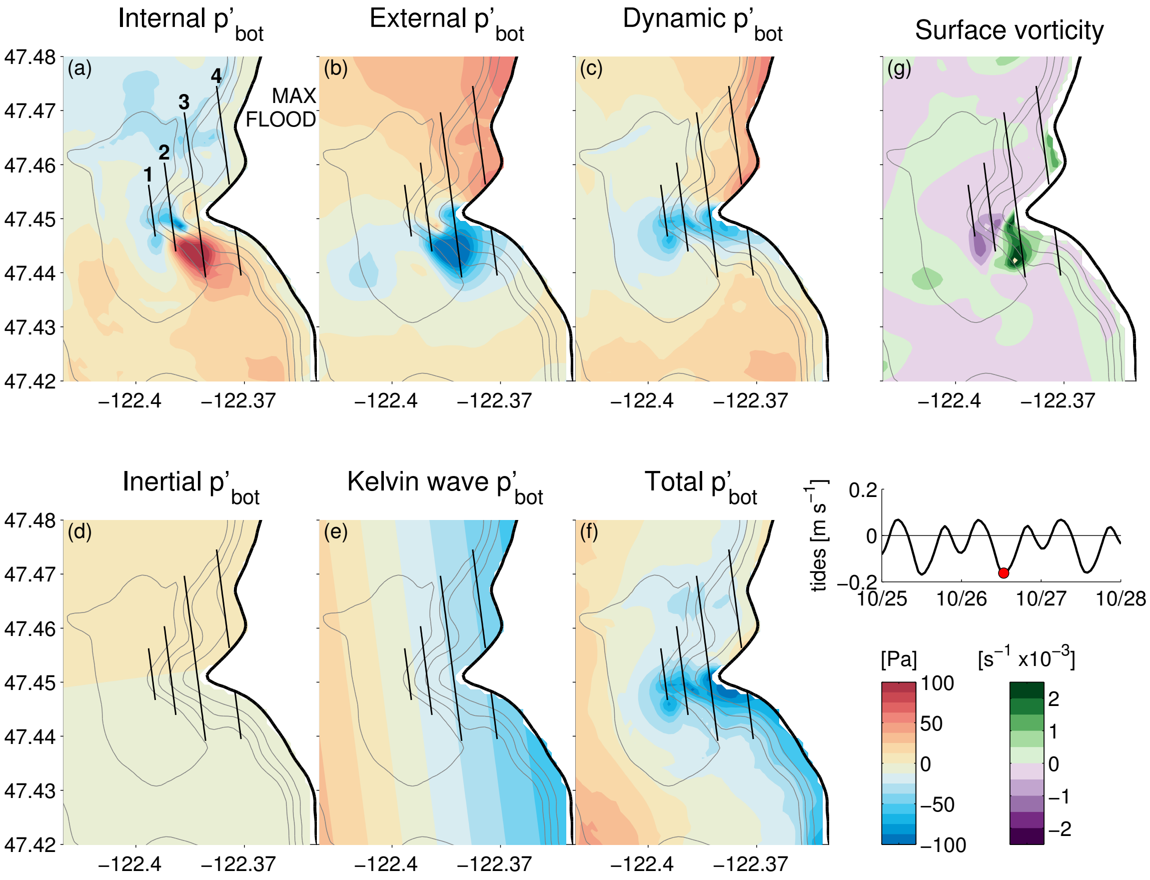

Figure 4.2: Bottom pressure anomalies (a-f) and vorticity (g) at maximum flood tide. The pressure anomaly has been broken up into internal (a), external (b), dynamic (c), inertial (d), and cross-channel Kelvin wave (e), and total (f) bottom pressure anomalies. Depth contours every 50 m. Four analysis transects are labeled in (a).

tracked through time (Fig. 4.4) by finding the maximum vorticity at the surface and at the bottom as shown with maps of surface and bottom vorticity in Fig. 4.5c. The eddy begins to form about two hours before maximum flood tide. Even at this early stage, the vorticity maximum at the surface is located much closer to the shore than the vorticity maximum at depth. As the tide gains strength, the eddy is stretched further due to velocity shear, eventually reaching its maximum horizontal

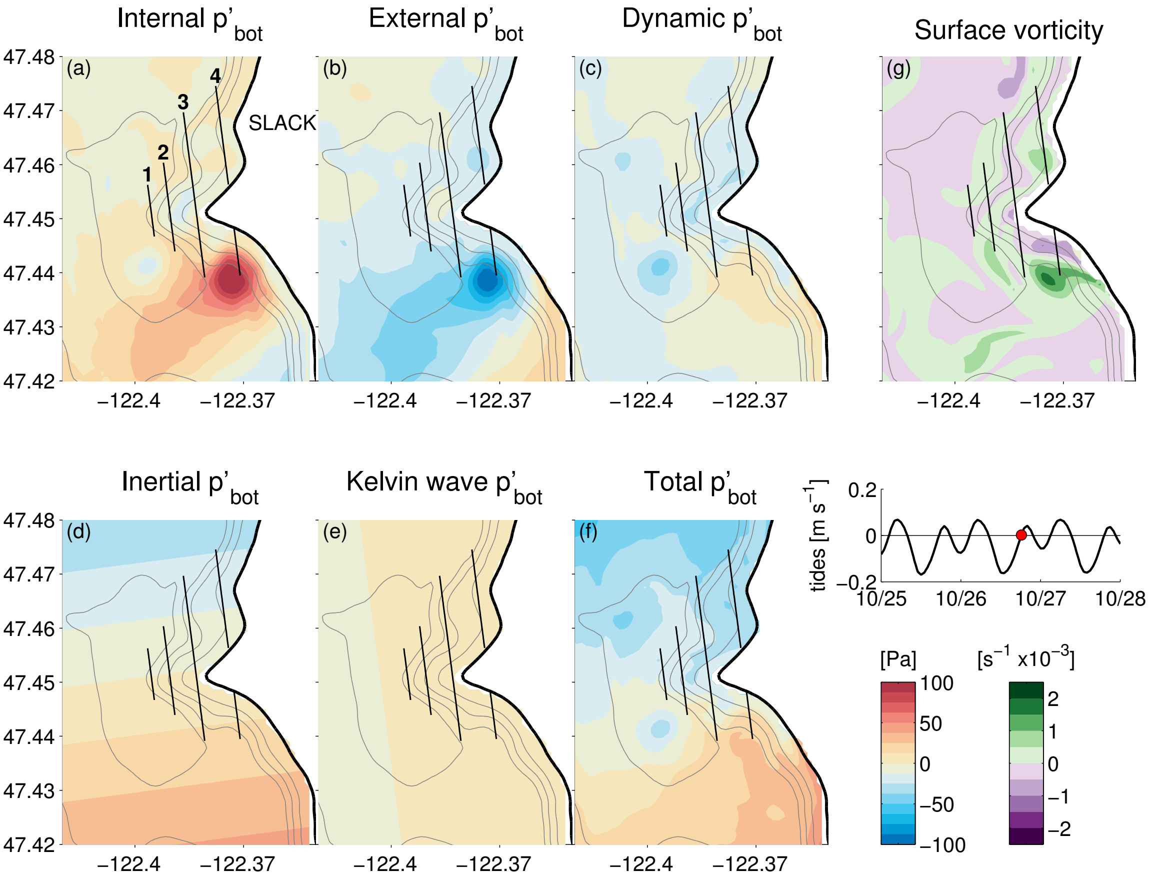

Figure 4.3: Bottom pressure anomalies (a-f) and vorticity (g) at slack tide.

displacement between surface and bottom of 1.7 km — equivalent to 3 eddy diameters — about 4 hours following the peak of flood tide. With this separation between surface and bottom, the eddy has a slope of about 1:7 (rise:run). This is even more stretched than the eddies described by Canals et al. (2009) who saw maximum eddy slope of 1:5. The eddy remains stretched throughout its lifespan even once it is advected by currents away from the headland. Despite this baroclinic nature of the density field, Canals et al. (2009) shows that the velocity remains almost entirely horizontal.

The tilt of the eddy leads to different isopycnal structure and bottom pressure

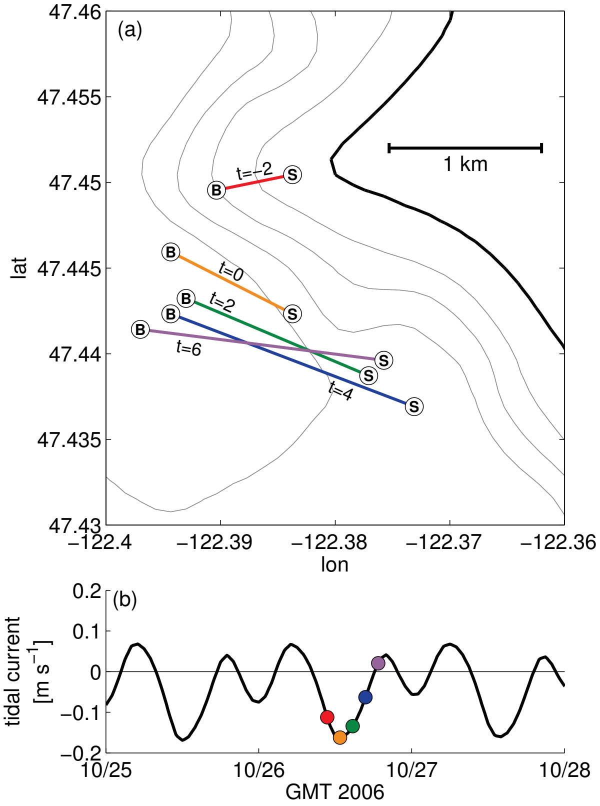

Figure 4.4: (a) The location of the surface (S) and bottom (B) of a lee eddy during a single flood tide plotted every 2 hours starting 2 hours before maximum flood tide and ending 6 hours after maximum flood tide. The colors of the lines correspond to the colors of the dots shown with the tidal current in (b). Depth contours every 50 m.

anomalies than are found in a vertical eddy. A vertical section that goes through the eddy (Fig. 4.5c), shows isopycnal contours that are depressed over the bottom half of the eddy and elevated in the top half. At the surface, there is a balance between the centripetal force of the currents and a radial pressure gradient, which can be written with the frictionless, steady shallow-water momentum equation in polar coordinates

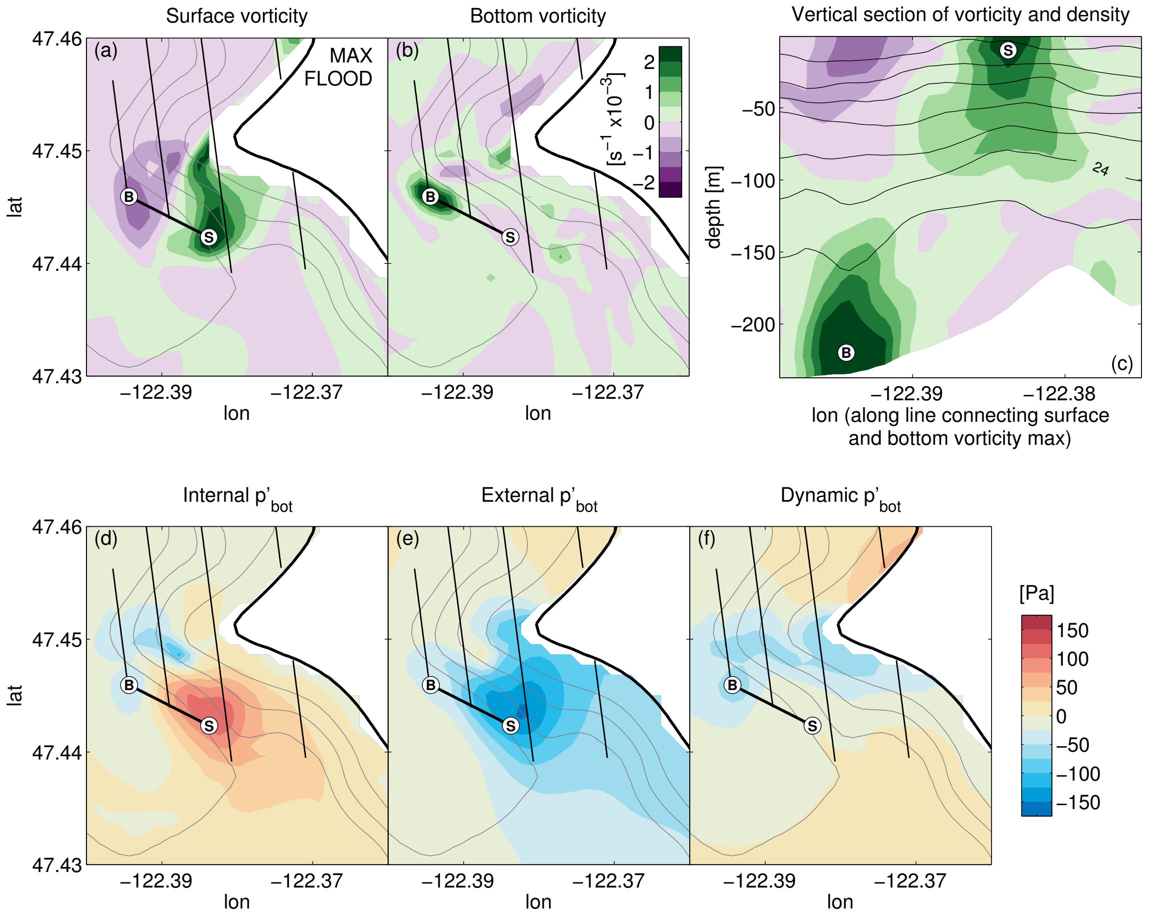

Figure 4.5: (a) Surface vorticity on the south side of TTP at maximum flood tide. Depth contours every 50 m in gray. Four analysis transects in black. (b) Vorticity in the bottom grid cells. The locations of the maximum surface vorticity (S) and the maximum bottom vorticity (B) are labeled in every subplot. (c) Vertical section of vorticity (color contours) overlaid with potential density contours (black) along a straight line that runs the surface and bottom vorticity maxima. Potential density contours are shown every 0.1 kg m^{-3} and the 1024 kg m^{-3} isopycnal is labeled. (d) Internal bottom pressure anomaly. (e) External bottom pressure anomaly. (f) Dynamic bottom pressure anomaly.

as,

$$-\frac{u_\theta^2}{r} - fu_\theta = -g\frac{\partial \eta}{\partial r} \tag{4.9}$$

where u_θ is the angular velocity and r is the radial coordinate. The Coriolis acceleration is an order of magnitude smaller than the centripetal acceleration. The angular currents of the eddy create a depression of the sea surface. Below this surface depression, there is upward heaving of the isopycnals to balance the low surface pressure. Integrated to the bottom, there is a strong negative external pressure of -129 Pa and a strong positive internal pressure of 122 Pa at this location (Fig. 4.5d,e). However, even though the internal and external pressure anomalies are large, the dynamic pressure anomaly is nearly zero (Fig. 4.5f). Only close to shore, in water shallower than 50 m where isopycnals cannot be raised enough to compensate for the low external pressure is there a non-zero dynamic pressure anomaly that has a magnitude greater than -50 Pa.

In the bottom half of the eddy, perturbations of the sea surface do not play a role like they do in the top half of the eddy. Here, there is a local balance of the centripetal force of the currents and the internal pressure field, which causes isopycnals to be drawn down. Therefore, both internal and external pressure anomalies are negative and they combine to a dynamic pressure of -61 Pa. The opposing forces that pull isopycnals up in the top half of the eddy and down in the bottom half can lead to vertical isopycnal excursions of 50 m as seen for the 1024.1 kg m^{-3} isopycnal (Fig. 4.5c).

Canals et al. (2009) develop an analytical model for the pressure field within a tilted eddy. They assume a constant slope of the eddy's core and balance the centripetal force with radial and hydrostatic pressure gradients. They show that the isopycnals are raised on the landward side of the eddy and depressed on the side farther from shore. The core of the eddies that are observed in our model do not have a constant slope. Instead, the eddy core is nearly vertical near the top and bottom and very sloping in the middle of the water column where the vorticity is lowest. Therefore, more complete compensation between the internal and external pressures in the top half of the eddy is observed than predicted with the analytical model of Canals et al. (2009).

Similar patterns of pressure anomalies occur at other times too. During slack tide (Fig. 4.3), the eddy from the previous flood has the strongest pressure signal within the domain. There is opposition between the internal and external pressures leading to zero dynamic pressure in the top half of the eddy. To the south of section 1, where the bottom of the eddy is located, there is a small patch of negative internal pressure that is not compensated by positive external pressure. Therefore, the biggest dynamic pressure anomaly within the domain is located not at the surface, but at the bottom of the eddy.

To summarize, due to to the tilted nature of the eddies at TTP, the isopycnals in the upper half of the eddy deviate upward to counteract the negative pressure anomaly at the surface. In the lower half of the eddy, the isopycnals deviate downward. Therefore, the eddy only contributes to form drag at its base where the external pressure does not counteract the internal pressure and in regions that are too shallow for the isopycnal excursions to counteract the external pressure. The internal and external pressures associated with an eddy have much larger magnitudes than the dynamic bottom pressure. Therefore, the external form drag measured by McCabe et al. (2006) should not be assumed to be the same size as the total form drag which is most likely much smaller.

4.3.2 Internal waves

Internal lee waves are a consistent feature at TTP (Edwards et al., 2004). The structure of the internal wave can be investigated by looking at vertical slices of density and bottom pressure along the 4 transects (Fig. 4.6). During flood tide along section 1, there is a lee waves on the south side of the topography that has a negative internal pressure anomaly (Fig. 4.6a,e). Qualitatively, this wave has a structure similar to the internal waves created by small, isolated ridges in infinite depth fluid described by Baines (1995, section 5.2). Unlike a classical mode 1 internal waves where the surface perturbations are in the opposite direction as the isopycnal perturbations, here, the external and internal pressures are both negative.

To more fully understand the pressure anomalies associated with the internal wave, the evolution of the internal wave can be investigated throughout a flood tide along section 1 (Fig. 4.7). Starting hour 1 which is shortly after slack tide, there are no perturbations of the density surfaces. One hour later, a low internal pressure anomaly begins to form on the south side of the topography. It grows in strength over the next hour, reaching its maximum perturbation of -63 Pa at hour 4 which is one hour before maximum flood tide. For the next three hours (t=5–7), there are large isopycnal perturbations within the lee wave. The structure of the internal pressure anomaly changes as the internal wave develops multiple peaks. By time 7, the negative internal pressure anomaly is nearly gone and there is even a small positive peak right on the south side of the topography. At time 8, the tide has slackened enough that the lee wave is released from the topography and begins to travel upstream to the north. It travels about 400 m northward and weakens significantly within the next hour.

Throughout the course of the flood tide, the external pressure does not have a consistent relationship to the internal pressure. As the tide is accelerating (t=2–4), the

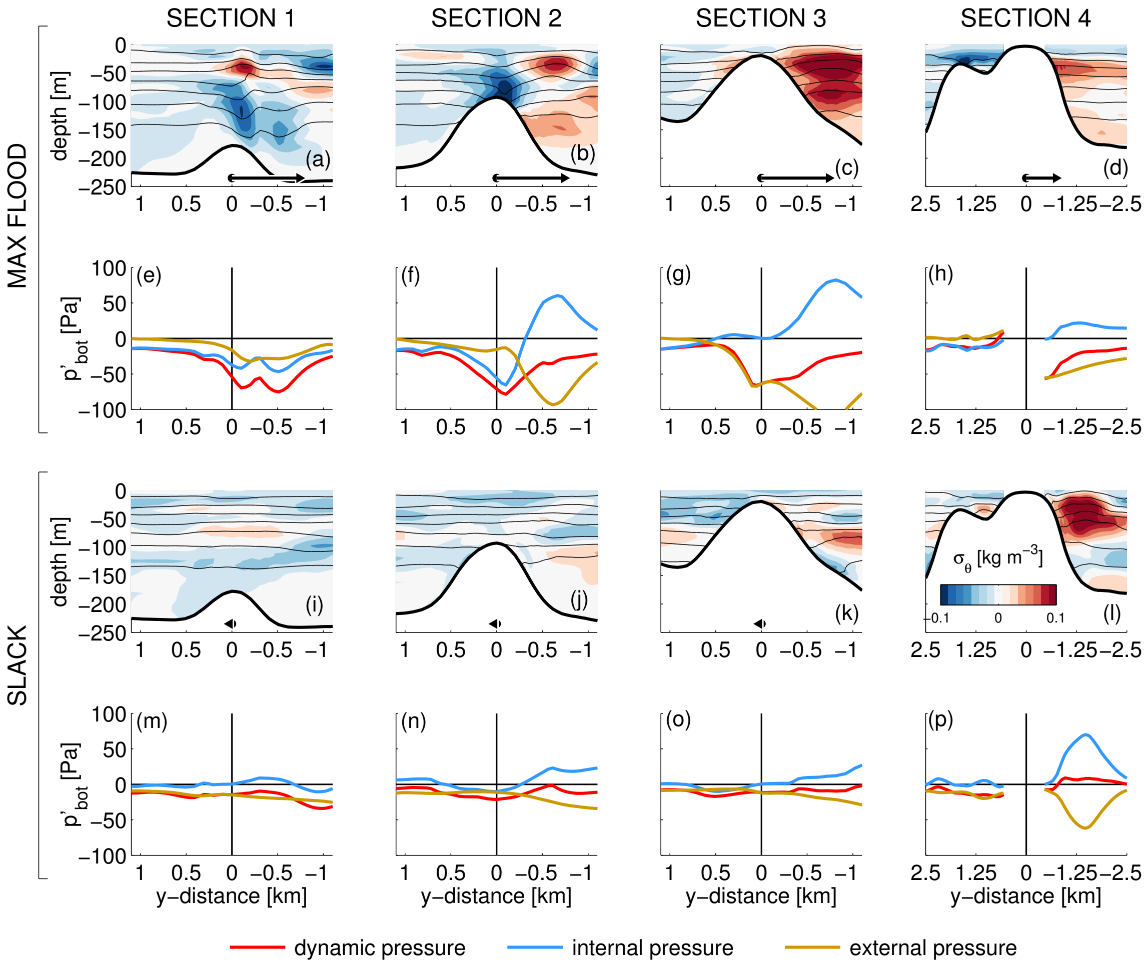

Figure 4.6: Density anomaly overlaid with contours of isopycnal height (a-d, i-l) during flood tide (a-h) and slack tide (i-p) along 4 transects. Density contours every 0.1 kg m^{-3}. Internal, external and dynamic bottom pressure anomalies (e-h, m-p). Note the difference in x-axis scale along transect 4.

external pressure is zero. While the tide is at its peak (t=5–7), the external pressure is mostly negative reaching a maximum of -33 Pa, and augmenting the negative internal pressure. As the tide decelerates (t=8–9), the external and internal pressures have opposite signs and mostly counteract each other. This pressure structure is

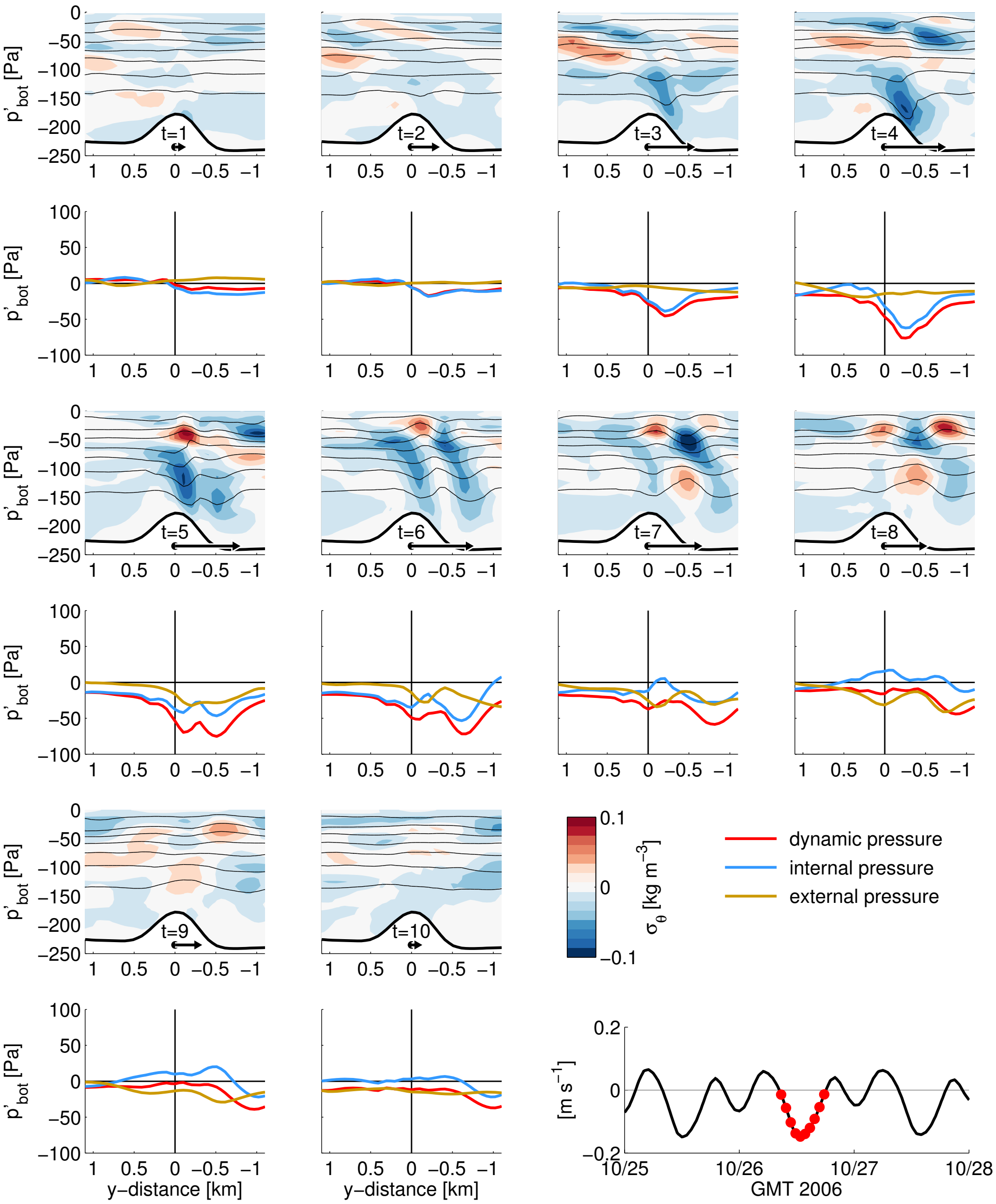

Figure 4.7: Density anomalies (colors), density contours (every 0.1 kg m^{-3}), and bottom pressure along section 1 every hour throughout a flood tide.

quite different from the nonlinear internal waves seen on the Oregon shelf by Moum and Smyth (2006), which consistently have opposite signs for internal and external pressures.

Along section 2 during flood tide, there is also an internal wave visible on the crest of the topography (Fig. 4.6b,f). There is negative internal pressure both upstream and downstream of the topographic crest, but the signal has a greater magnitude on the lee side of -66 Pa. Just like with the internal wave on section 1 during maximum flood tide, the external pressure does not counteract the internal pressure. This internal wave along section 2, however, is dwarfed by the a positive internal pressure of 59 Pa and negative external pressure of -92 Pa located farther downstream. This is due to the eddy that is mostly situated on transect 3 but impinges on the very south end of transect 2 (Fig. 4.2a-b).

The presence of both internal waves and eddies is what makes the dynamics at TTP complicated. Along transects 1 and 2, it is assumed that internal waves are the dominant mechanism, however, at times, eddies also cross these transects. At Knight Inlet, Klymak and Gregg (2001, 2003) describe a situation where internal lee waves are affected by lateral recirculation. The recirculation can account for 25 percent of the flow thereby increasing the size of the internal lee waves. The flow at TTP is different from this. Unlike the internal lee waves at Knight Inlet, we do not suspect that the flow here is hydraulically controlled. The Froude number stays well within the subcritical range along section 1 ($Fr = v_0/(N(H - h_0)/\pi) \leq 0.54$). Furthermore, at Knight Inlet, the recirculation is located in a layer of fluid directly on top of the internal wave (Klymak and Gregg, 2001). At TTP, the eddies only periodically interact with the internal waves, intersecting only when the eddies grow large enough to reach the internal lee wave. When the eddy does impinge upon the internal wave, it alters the pressure field because the pressure perturbation from the eddy is often much larger than the pressure anomaly from the internal waves. We also suspect that the eddies may confine the internal waves to a shorter down-stream extent. Along transect 1, where the eddy is not present, the internal wave impacts the pressure anomalies as far as 750 m downstream. Along transect 2, the internal wave can only depress isopycnals as far as 200 m beyond the topographic crest because the eddy is located just downstream. Therefore, unlike Klymak and Gregg (2003) who suggest that the recirculation strengthens the internal wave, here we conclude that the eddy may impede the formation of the internal wave.

Along sections 3 (Fig. 4.6c,g) and 4 (Fig. 4.6d,h), the topography is too tall with respect to the water column depth to create internal waves.

During slack tide, pressure anomalies are all small except along section 4 and the very southern ends of sections 2 and 3 where there is an eddy that has been pushed back into the domain (Fig. 4.6i-p).

In summary, internal lee waves are generated during flood tides on the more ridge-like part of TTP. They start to form about two hours before maximum flood tide and remain attached to the topography until the tidal currents slacken sufficiently to release the wave, which occurs about 3 hours after maximum flood. The lee waves create a negative internal pressure on the lee side of the topography. At the beginning of the flood tide, the external pressure remains zero. Further into the tide, it sometimes acts to counteract the internal pressure and sometimes acts in concert with it. When eddies are present along the ridge transects, they can drastically change the pressure field and confine the internal wave to a smaller extent along the transect.

4.4 Implications for form drag and power

By examining the form drag and power along the four sections (Fig. 4.8), more insight can be gained about how the dynamics at TTP work. Here, form drag and power

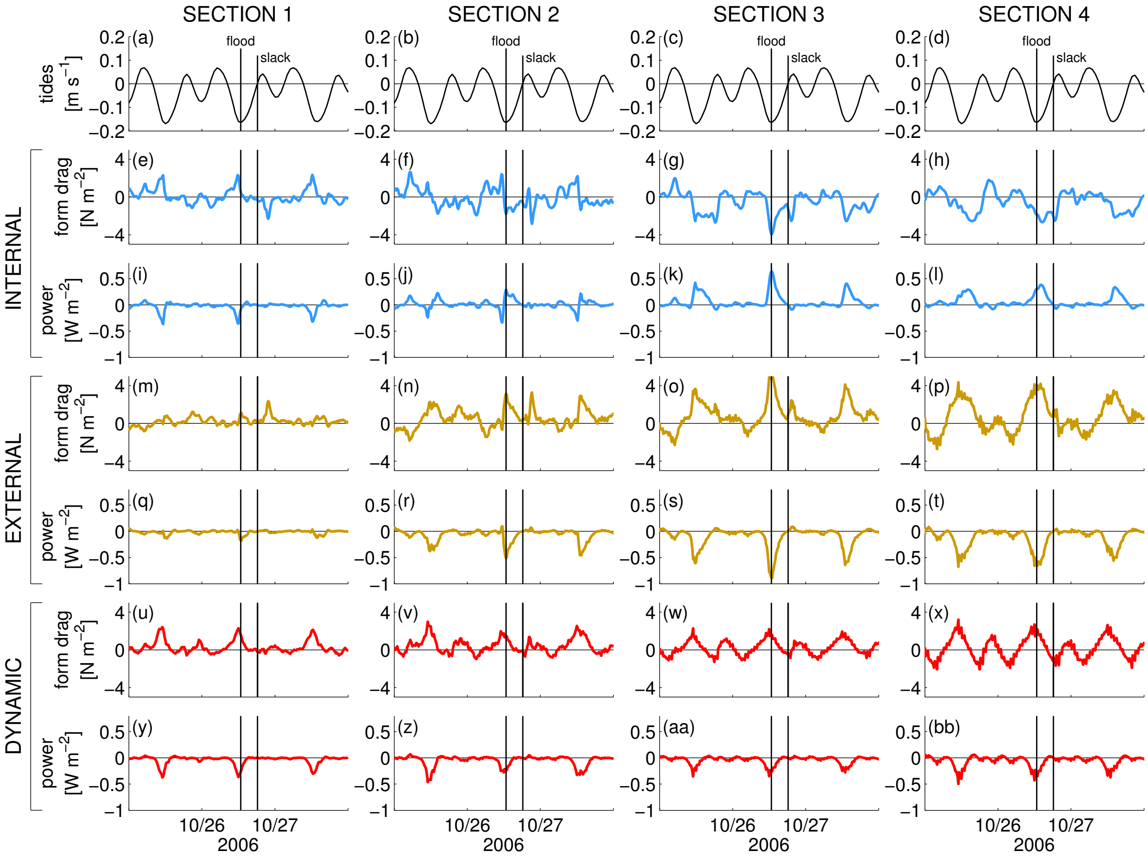

Figure 4.8: Time series of tidal currents (a-d), internal form drag (e-h), internal power (i-l), external form drag (m-p), external power (q-t), dynamic form drag (u-x), and dynamic power (y-bb) along the four analysis sections. The form drag and power has been divided by transect length and are reported in N m^{-2} and W m^{-2}, respectively. The flood and slack tides in Figs. 4.2 and 4.3 are marked. Only part of the time series is shown in order to see the details.

are in units of N m^{-2} and W m^{-2}, respectively. The integrated form drag and power along each transect line has been divided by the length of the transect line to get units per meter squared.

The internal form drag and power behave quite dissimilarly in different regions of the topography. Along section 1, the internal form drag (Fig. 4.8e) is generally positive during flood tides and close to zero at other times, leading to distinct negative peaks in internal power during flood tide (Fig. 4.8i). In contrast, along sections 3 and 4, the internal form drag tends to be negative during flood tides (Fig. 4.8g,h), and the internal power is positive (Fig. 4.8k,l). Transect 2 seems to be a combination of the two (Fig. 4.8f,j). It has positive form drag in the first half of the flood tide and negative form drag in the second half. This is because during the first half of flood tide, the dynamics are governed by an internal lee wave. Then, during the second half of flood tide, an eddy moves onto the transect dominating the signal of the internal wave. This interaction of internal waves and eddies leads to internal power that changes sign throughout the tide along transect 2.

In general, the external form drag is positive along all four transects leading to distinct negative peaks in power during flood tides. The external form drag is much more important for the eddy than it is for the internal wave, and therefore it has bigger amplitudes along transects 3 and 4 than along transects 1 and 2.

Despite the differences in internal and external form drag and power between the transects, the dynamic form drag and power have surprisingly similar signals, both in shape and size. Along all four transects, peaks in power of -0.4 W m^{-2} occur during large flood tides and the power is close to zero at other times. Along transect 1, the internal and external power have the same sign and augment each other. Along transects 3 and 4, the internal and external powers have larger magnitudes than along transect 1, but the signs are opposite, and the dynamic power ends up having nearly the same size as it does along transect 1. Overall, in regions where internal waves dominate, the internal and external powers act together, whereas in regions where the eddy dominates, they act against each other.

The internal, external and dynamic powers can be time-averaged to get an overall picture of the energy conversion at TTP (Fig. 4.9). The internal power is negative along section 1 and increases to be positive along section 4. Its sign reverses as the dominance of internal waves is overcome by eddies toward shore. The external power is negative along all four transects, its magnitude increasing toward shore. Due to the opposite trends of the internal and external average powers, the dynamic power actually remains nearly constant across the topography at -0.044 ± 0.008 W m^{-2}. Scaled to account for the slower velocity within the model than in reality (Appendex A), the average power is -0.11 W m^{-2}, which is probably still somewhat small because the model topography has also been smoothed. Our power estimates can be compared to time-averaged barotropic-to-baroclinic conversion rates in other locations. In a model of Monterey Bay Canyon, Kang and Fringer (2012) find spatial peaks of 0.2 W m^{-2} and in a model of the Hawaiian Ridge, Carter et al. (2008) finds spatial peaks of 3 W m^{-2}.

In chapter 3, it was found that the internal power made up 80 percent of the total power along the ridge transect. In the model, it was found that the internal power makes up less than 10 percent of the dynamic power along transect 2 which is in the same location as the ridge transect in the observations. The physical reason that there is not as much internal drag along transect 2 is because the eddy often encroaches on the southern end of the transect during flood tides. Due to smoothing of the topography within the model, it is possible that the eddy takes a slightly different path in the model than it does in reality. Since the eddy carries such a large pressure anomaly, it is possible that section 2 in the model is much more influenced by the eddy than the ridge transect was in the observations. Along transect 1, the internal power makes up 60 percent of the dynamic power which is much closer to what was observed along the ridge transect in chapter 3.

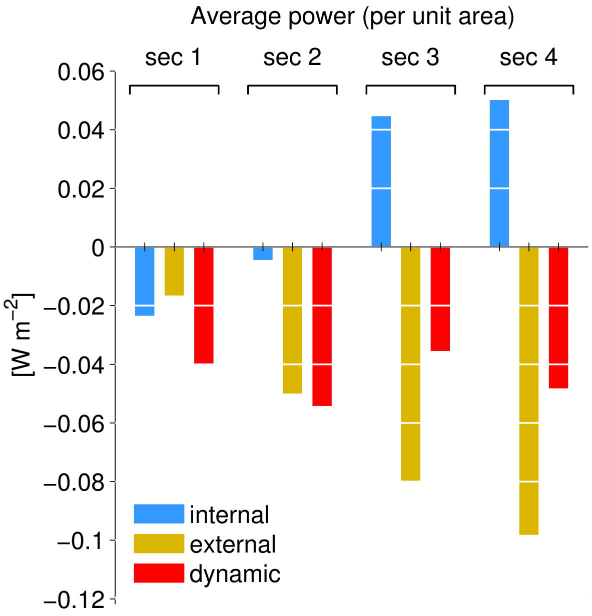

Figure 4.9: Time averaged internal, external and dynamic powers along the 4 transects.

4.5 Conclusions

In this study, a numerical model of Three Tree Point was used to gain insight into the physical mechanisms that create form drag across this sloping headland. The part of the bottom pressure field that contributes to form drag was divided into the internal and external pressures so the eddies and internal waves could be identified. It was found that internal waves are the dominant mechanism along the ridge-like part of the topography and eddies are the dominant mechanism along the headland-like part of the topography. Both the internal waves and eddies are largest during strong flood tides and much weaker during the small flood or ebb tides.

In regions where internal waves dominate, internal and external pressure work in concert to create dynamic pressure that is larger than either individual part. The average dynamic power is made up of 60 percent internal power and 40 percent external power. The dynamics are complicated in the internal wave regime when eddies are pushed into this part of the domain which affects the bottom pressure anomalies and can confine the eddy to a smaller region along the topography.

The tilted nature of the eddies leads to a complicated pattern of internal and external pressures. In the top half of the eddy, the external pressure is negative and the internal pressure is positive, which leads to a dynamic bottom pressure that is nearly zero except right next to the shore where the internal pressure cannot compensate. In the bottom half of the eddy, which can be located nearly 2 km from the surface of the eddy, both the internal and external pressures tend to be negative. However, the bottom of the eddy is often located over flat parts of topography and does not contribute significantly to form drag. Overall, in the regions where eddies dominate, the internal power tends to be positive and the external power tends to be negative. Together, they lead to a dynamic power that is also negative but only about half as big as the external power.

Even though the internal and external pressure anomalies of the eddy have much bigger magnitudes than the pressure anomalies from the internal wave, both processes do similar amounts of work. The dynamic power loss has peaks of 0.4 W m^{-2} across the topography which equivalent to a time average of 0.04 W m^{-2}. Scaled to account for the slower velocity in the model than at the real TTP gives a time-averaged power loss of 0.11 W m^{-2}. This is much larger than losses due to friction.

Overall, this study shows the complicated dynamics that occur when both internal waves and eddies are created by sloping topography. The eddies are tilted and have a pressure anomaly structure that is different from vertical eddies. The internal waves are only created on the ridge-like part of the topography and can be suppressed by the presence of an eddy. Therefore, when parameterizing drag, TTP cannot be treated simply as a headland or a ridge that only generates a eddy or an internal wave. Topography that is similar to TTP is abundant in high latitude, coastal regions, and understanding the dynamics here is a step towards better form drag parameterizations that can be used in larger scale models.

4.6 Appendix A: Model compared to observations

The goal of this paper is not to directly compare the TTP model to the field observations that are detailed in chapter 3, but instead to gain insight into the physical mechanisms that create form drag. Differences are expected between the model and observations simply because they cover different time periods (model: October 24 – October 31, 2006, observations: October 26 – Novermber 2, 2010). Furthermore, the model bathymetry had to be smoothed (Fig. 4.1e). Despite this, we compare the model to the observations so we know what the model does and does not do well.

4.6.1 Density

The model is too salty by about 1 psu (Fig. 4.10a), which is a known defect of the MoSSea model (Sutherland et al., 2011). This leads to potential density within the model that is about 0.75 kg m^{-3} too high (Fig. 4.10c). The potential temperature in the model is similar to the observed (Fig. 4.10b). Despite the differences in salinity and density, the buoyancy frequency is generally the same (Fig. 4.10d). Differences in stratification could affect how easy it is for water to flow over versus around the topography. As the buoyancy frequency increases, it is more likely for the flow to be around the topography than over it (MacCready and Pawlak, 2001).

4.6.2 Tidal currents

The time period of the model was chosen to match the tides from the observations as closely as possible, however, there are some differences between the two, most notably in their amplitude (Fig. 4.11a,h). The maximum velocity during flood tides in the model and observations are 0.17 m s^{-1} and 0.23 m s^{-1}, respectively. The reason for this disparity is due to the weak M2 tidal currents in the MoSSea Model (Sutherland et al., 2011). Due to weaker tides, it is expected that the form drag and power will

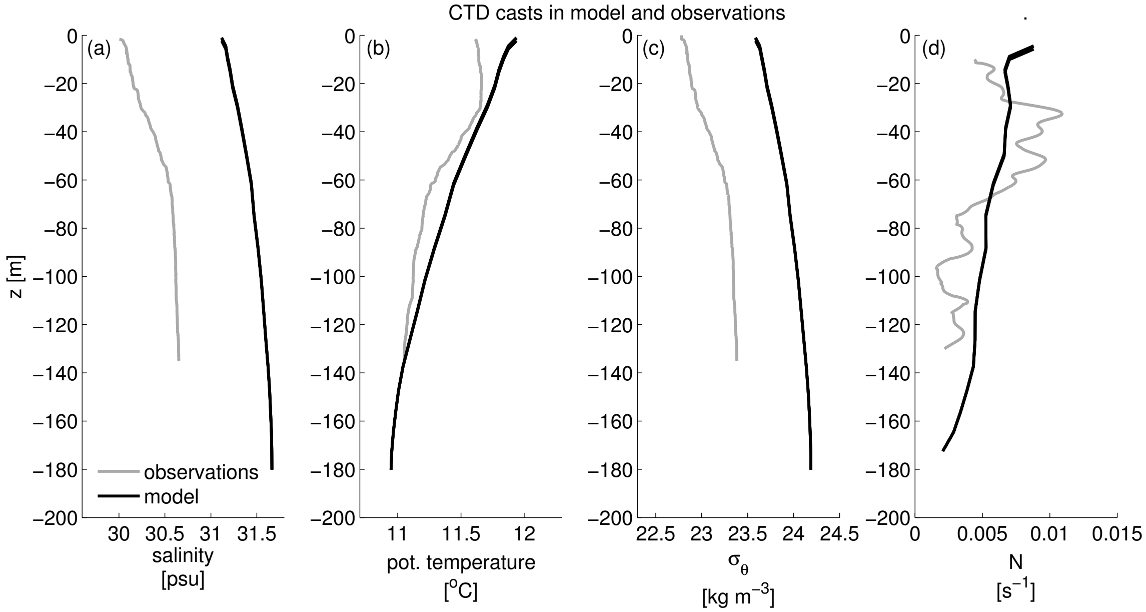

Figure 4.10: (a) Salinity from the observations averaged over the time period of the cruise in 2010 (gray) and from model averaged over the week in 2006 during which the model was run (black). (b) Potential temperature. (c) Potential density. (d) Buoyancy frequency.

not be as big as the observations. Nonetheless, the form drag is still many times greater than the frictional drag.

4.6.3 Bottom pressure anomalies

Bottom pressure anomalies from the model and observations can be compared at the locations of the pressure sensors (Ppods) from the field study (Fig. 4.11). There are similar patterns between the two. The pressure anomalies on the north side of TTP (Fig. 4.11b-c, i-j) are smaller than the pressure anomalies on the crest (Fig. 4.11d-e, k-l) and south side (Fig. 4.11f-g, m-n). The magnitude of the bottom pressure anomalies on the south side during strong flood tides are quite large, whereas during ebb and

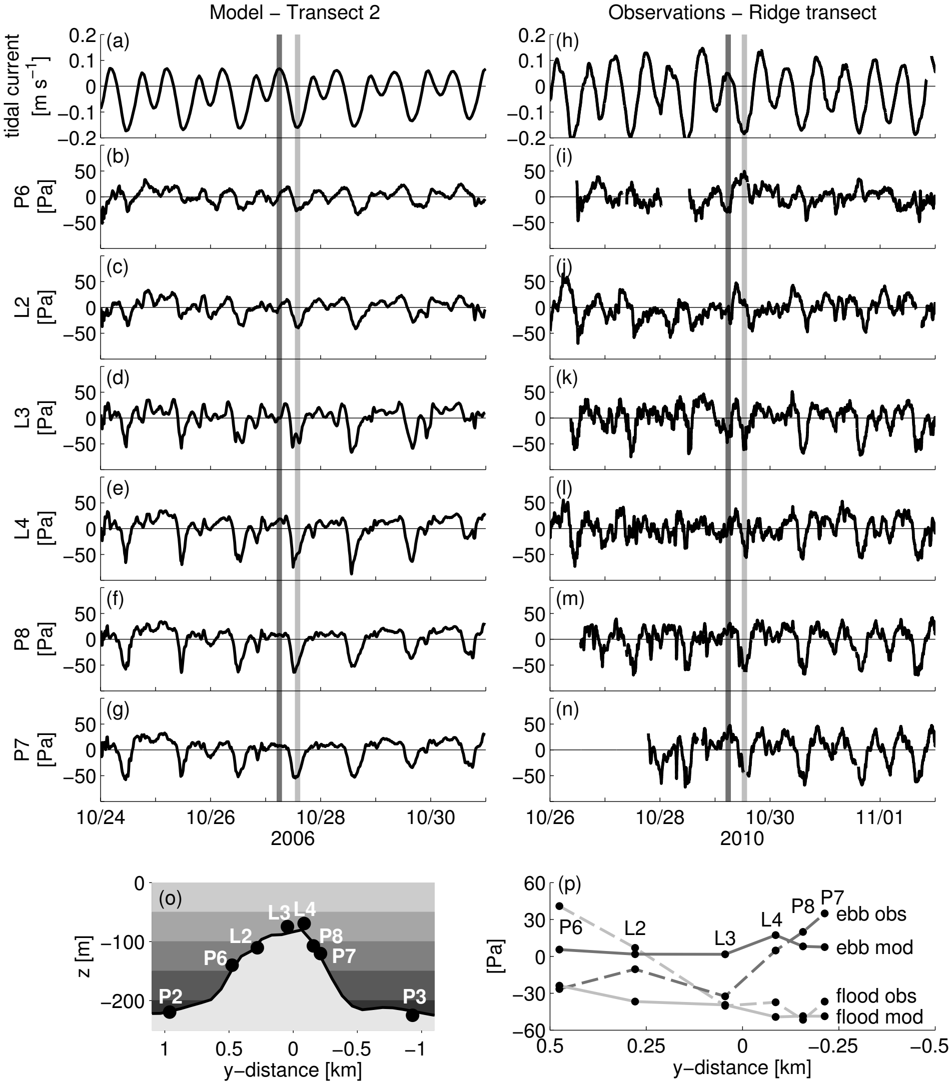

Figure 4.11: (a) Model tides. Vertical bars highlight two hours spanning maximum flood (light gray) and maximum ebb (dark gray). (b-g) Bottom pressure anomalies from the model on transect 2. Locations in (o). (h) Observed tides. (i-n) Bottom pressure anomalies from the Ppods. (p) Average bottom pressure anomalies plotted with respect to distance from the topographic crest during ebb (dark gray) and flood (light gray) for both the model (solid lines) and the observations (dashed lines).

weak flood tides, the signal is much smaller. In both the model and observations, the bottom pressure anomaly decreased from north to south during flood tides (Fig. 4.11o). However, that decrease is about four times greater in the observations (change of 100 Pa) than in the model (change of 25 Pa). During ebb tides, the pressure increased from north to south in the observations (change of 60 Pa), whereas, in the model, there is only a slight increase in pressure anomalies across the topography during ebb tide. Overall, the amplitude of the bottom pressure anomalies are too small in the model, but the patterns of high and low pressure are similar between the model and observations.

4.6.4 Form drag and power

Both the observations and model (Fig. 4.12) show largest peaks of form drag (Eq. 4.7) and power (Eq. 4.8) at maximum flood tides and much smaller peaks during ebbs and weak floods. The observed amplitude is larger than the modeled. The average observed power is 248 W m^{-1} and the average model power is 100 W m^{-1}. Based on the differences between modeled and observed tidal velocities, and a form drag that varies as v_0^2, we would predict that the model would only account for 40 percent of the observed power.

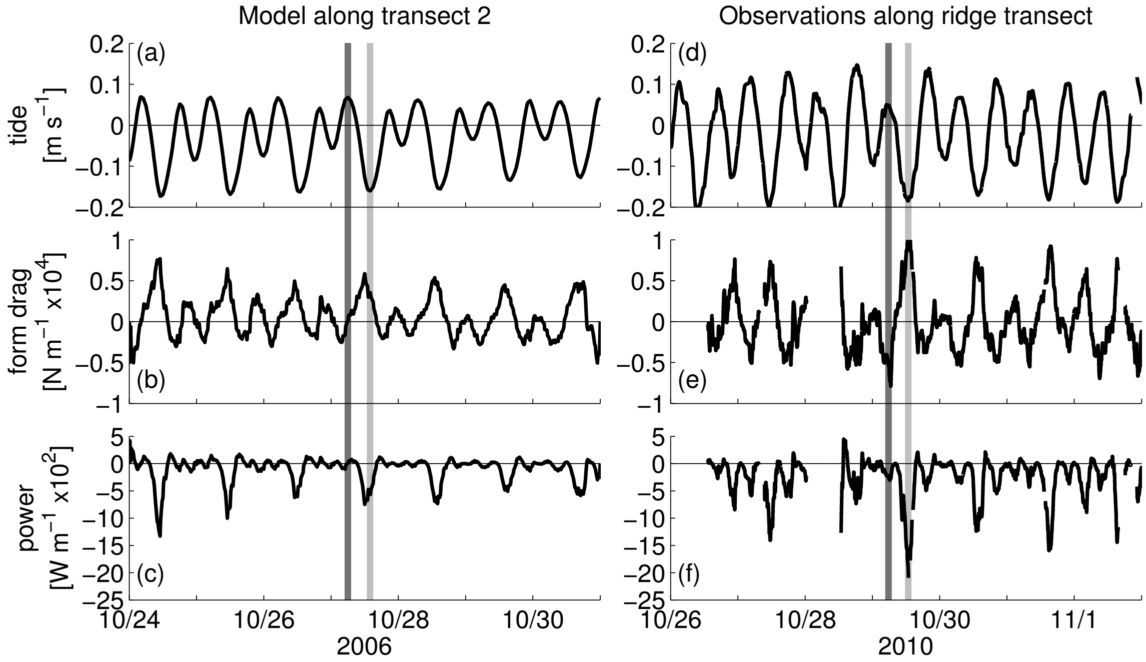

Figure 4.12: (a) Tidal currents from the model. Vertical bars indicate one hour before to one hour after max flood (light gray) and max ebb (dark gray). Form drag (b) and power (c) from transect 2 in the model. (d) Tidal currents from the observations. Form drag (e) and power (f) calculated with Ppods.

4.7 Appendix B: Ppod abundance

One of the biggest unanswered questions from the observations at TTP was whether or not enough Ppods were used to measure the form drag. To test this, form drag and power were calculated from model pressure at different locations along each transect (Fig. 4.13). First, the locations of the 4 Ppods used to calculate observed form drag along transect 2 were used (Fig. 4.13a red dot). An average power of -0.054 W m^{-2} was found. Then, different numbers of evenly spaced bottom pressure measurements along transect 2 were used (Fig. 4.13a blue dots). It was found that with 4 or more pressure measurements the average power was essentially the same at -0.056 ± 0.002 W m^{-2}. Randomly placed pressure measurements were also tested (Fig. 4.13a black dots). There was a lot more variability with this test because it was possible for all of the pressure measurements to be grouped together or in some other unfortunate distribution. It was found that with 8 random pressure measurements the average power was -0.041 ± 0.037 W m^{-2}. With any fewer measurements, the standard deviation was larger than the average. With 16 random pressure measurements that average power was -0.045 ± 0.019 W m^{-2}, which is an improvement over 8 measurements. In general, with a random distribution of pressure measurements, the average power loss is underestimated compared to an even distribution of pressure measurements, and a lot more pressure sensors are needed.

The tests were also run along transect 3 (Fig. 4.13b). Here it was found that the average power calculated at the Ppod locations (-0.059 W m^{-2}) is an over-estimate of the average power found with six or more pressure measurements (-0.040 ± 0.005 W m^{-2}). Since this transect is longer than transect 2, it was found that more pressure measurements were needed to get an accurate estimate of the average power.

Overall, it is important that pressure sensors are evenly distributed and placed in key locations to ensure an accurate estimate of form drag. It is best to have at least 2

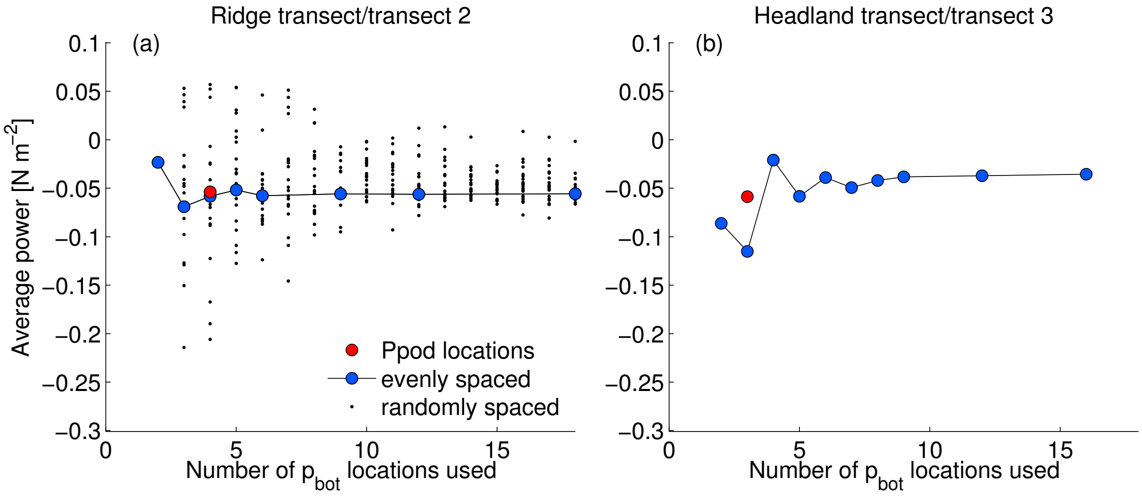

Figure 4.13: Test of how many Ppods are necessary to measure form drag on topography. The number of pressure measurements used in each case (x-axis) are plotted versus the average power (y-axis). Three different calculations of average power were made: using model pressure at the Ppods locations (red dot), using evenly spaced pressure measurements (blue dots), and using randomly spaced pressure measurements (black dots). (a) Tests run along the transect 2 (ridge transect). (b) Tests run along the transect 3 (headland transect).

— more if possible — pressure measurements on both the up- and downstream sides of the topography. In the TTP experiment, there were only 2 Ppods on each side of the topography along transect 2 that were used to calculate form drag, but the placement was careful enough that the estimate for average power from the Ppod locations is quite close to the average power calculated with many more pressure measurements. On transect 3, where there were only 3 Ppods on the entire transect line, it is possible that the form drag and associated power estimates were inaccurate.

Chapter 5

CONCLUSIONS

This thesis aims to understand the processes that convert tidal energy into internal waves and eddies as currents flow past Three Tree Point (TTP), a headland in Puget Sound, Washington. Both numerical models and observations are used to dissect the pressure field at TTP into the parts that can and cannot create form drag and the parts associated with internal lee waves versus eddies.

In chapter 2, it is shown that there is a part of the form drag that is due simply to the oscillatory nature of the flow: inertial form drag. This part of the form drag was first discovered by engineers who were concerned with the forces exerted by waves on offshore structures. We prove here that the same theory also holds in much larger contexts when tidal currents flow past vertical-walled headlands. At slack tides, there is an along-channel pressure gradient that accelerates the flow. This pressure gradient creates form drag around a headland. However, since this pressure gradient has its maximum amplitude at slack tides, it cannot do tidally averaged work on the flow because its phase is in quadrature with the tidal velocity. Therefore, even though the inertial drag can have an amplitude that is as big as the form drag created by internal waves or eddies, the inertial drag does not extract energy from the flow.

In chapter 3, an array of very sensitive seafloor pressure gauges (Ppods) are deployed across TTP to measure the form drag that is created as tidal currents flow past this sloping headland. The Ppods measure pressure perturbations due both to isopycnal and sea surface height anomalies. It is shown that form drag is much larger than frictional drag. Not only that, frictional drag only does work in the bottom boundary layer, whereas form drag can affect the fluid throughout the water column as seen with sections of density and microstructure measured with a shipboard profiler. The form drag is estimated to convert 0.2 W m^{-2} of tidally averaged power away from the barotropic tides. It is shown that a linear wave drag law does a better job of parameterizing the form drag than a bluff body drag law. This is due to the stratified nature of the flow that creates both internal waves and eddies.

In chapter 4, a high-resolution numerical model of TTP is used to determine whether internal waves or eddies do more work on the flow. The pressure field is divided into the internal pressure which is due to changes in isopycnal height, the external pressure which is due to perturbations of the sea surface, and the dynamic pressure which is the sum of the internal and external pressures. It is shown that the pressure perturbations due to the eddies are much larger than the pressure perturbations due to the internal lee waves. However, in the eddy, the low external pressure created by a sea surface depression is always balanced by high internal pressure due to raised isopycnals. This means that the dynamic pressure in the eddy has a much smaller magnitude than either the internal or external pressures alone. Therefore, both internal waves and eddies do similar amounts of work on the flow with the internal lee wave acting on the more ridge-like part of the topography and the eddy acting closer to shore.

Through this thesis, we gain a deeper understanding of how form drag works on sloping topography. Even though TTP only dissipates a fraction of the energy that is put into the world's oceans as tides, topography like TTP is common in high latitude coastal regions. At places like these, the form drag is a much more important process for dissipating energy than frictional drag. We hope the work here can lead to better drag parameterizations in larger numerical models that do not resolve the scales important to form drag.

BIBLIOGRAPHY

Armi, L., 1986: The hydraulics of two flowing layers with different densities. *J. Fluid Mech.*, **163**, 27–58.

Baines, P. G., 1995: *Topographic Effects in Stratified Flows*. Cambridge University Press.

Balmforth, N. J., G. R. Ierley, and W. R. Young, 2002: Tidal conversion by subcritical topography. *J. Phys. Oceanogr.*, **32**, 2900–2914.

Batchelor, G. K., 1967: *An Introduction to Fluid Dynamics*. Cambridge University Press, Cambridge.

Bearman, P. W., M. J. Downie, J. M. R. Graham, and E. D. Obasaju, 1985: Forces on cylinders in viscous oscillatory flow at low Keulegan-Carpenter numbers. *J. Fluid Mech.*, **154**, 337–356.

Bell, T. H., 1975a: Lee waves in stratified flows with simple harmonic time dependence. *J. Fluid Mech.*, **67**, 705–722.

Bell, T. H., 1975b: Topographically generated internal waves in the open ocean. *J. Geophys. Res.*, **80**, 320–327.

Black, K. P. and S. L. Gay, 1987: Eddy formation in unsteady flows. *J. Geophys. Res.*, **92 (C9)**, 9514–9522.

Bougeault, P., et al., 1993: The atmospheric momentum budget over a major mountain range: first results of the pyrex field program. *Ann. Geophys.*, **11**, 395–418.

Boyer, D. L. and L. Tao, 1987: On the motion of linearly stratified rotating fluids past capes. *J. Fluid Mech.*, **180**, 429–449.

Bretschneider, D. E., G. A. Cannon, J. R. Holbrook, and D. J. Pashinski, 1985: Variability of subtidal current structure in a fjord estuary: Puget Sound, Washington. *J. Geophys. Res.*, **90 (C6)**, 11 949–11 958.

Callendar, W., J. M. Klymak, and M. G. G. Foreman, 2011: Tidal generation of large sub-mesoscale eddy dipoles. *Ocean Science*, **7 (4)**, 487–502, doi:10.5194/os-7-487-2011.

Canals, M., G. Pawlak, and P. MacCready, 2009: Tilted baroclinic tidal vortices. *J. Phys. Oceanogr.*, **39 (2)**, 333–350.

Canuto, V. M., A. Howard, Y. Cheng, and M. S. Dubovikov, 2001: Ocean turbulence. Part I: One-point closure model—Momentum and heat vertical diffusivities. *J. Phys. Oceanogr.*, **31**, 1413—1426.

Carter, G. S., et al., 2008: Energetics of M_2 barotropic-to-baroclinic tidal conversion at the Hawaiian Islands. *J. Phys. Oceanogr.*, **38**, 2205–2223, doi: 10.1175/2008JPO3860.1.

Cenedese, C. and J. A. Whitehead, 1999: Eddy shedding from a boundary current around a cape over a sloping bottom. *J. Phys. Oceanogr.*, **30**, 1514–1521.

Chapman, D. C., 1985: Numerical treatment of cross-shelf open boundaries in a barotropic coastal ocean model. *J. Phys. Oceanogr.*, **15**, 1060—1075.

Dean, R. G. and R. A. Dalrymple, 1984: *Water wave mechanics for Engineers and Scientists*. Prentice-Hall, Inc., Englewood Cliffs, NJ.

Donner, L. J. and W. G. Large, 2008: Climate modeling. *Annu. Rev. Fluid Mech.*, **33**, 1–17.

Edwards, K. A., P. MacCready, J. N. Moum, G. Pawlak, J. Klymak, and A. Perlin, 2004: Form drag and mixing due to tidal flow past a sharp point. *J. Phys. Oceanogr.*, **34**, 1297–1312.

Emery, W. J. and R. E. Thomson, 2004: *Data Analysis Methods in Physical Oceanography.* 2d ed., Elsevier Inc.

Faltinsen, O. M., 1990: *Sea loads on ships and offshore structures.* Cambridge University Press, Cambridge.

Farmer, D. and L. Armi, 1999a: The generation and trapping of solitary waves over topography. *Science*, **283 (5398)**, 188–190.

Farmer, D. M. and L. Armi, 1999b: Stratified flow over topography: the role of small-scale entrainment and mixing in flow establishment. *Proc. Roy. Soc. Lond.*, **455**, 3221–3258.

Finlayson, D. P., 2005: Combined bathymetry and topography of the Puget Lowland, Washington State, University of Washington (http://www.ocean.washington.edu/data/pugetsound/psdem2005.html).

Flather, R. A., 1976: A tidal model of the northwest European continental shelf. *Mem. Soc. Roy. Sci. Liege*, **10**, 141—164.

Fox, R. W. and A. T. McDonald, 1998: *Introduction to Fluid Mechanics.* 5th ed., John Wiley & Sons, Inc., New York, NY.

Freeland, H. J., 1990: The flow of a coastal current past a blunt headland. *Atmosphere-Ocean*, **28**, 288–302.

Garner, S. T., 2005: A topographic drag closure built on an analytical base flux. *J. Atmos. Sci.*, **62**, 2302—2315, doi:http://dx.doi.org/10.1175/JAS3496.1.

Garrett, C. and E. Kunze, 2007: Internal tide generation in the deep ocean. *Annu. Rev. Fluid Mech.*, **39 (1)**, 57–87.

Geyer, W. R., 1993: Three-dimensional tidal flow around headlands. *J. Geophys. Res.*, **98 (C1)**, 955–966.

Geyer, W. R. and R. Signell, 1990: Measurements of tidal flow around a headland with a shipboard acoustic Doppler current profiler. *J. Geophys. Res.*, **95 (C3)**, 3189–3197.

Gill, A. E., 1982: *Atmosphere-Ocean Dynamics*. Academic Press, San Diego, CA.

Hoerner, S. F., 1965: *Fluid-Dynamic Drag: Information on Aerodynamic Drag and Hydrodynamic Resistance*. Hoerner Fluid Dynamics, Bakersfield, CA.

Jayne, S. R. and L. C. St. Laurent, 2001: Parameterizing tidal dissipation over rough topography. *Geophys. Res. Lett.*, **28 (5)**, 811–814.

Jones, G. W., J. J. Cincotta, and R. W. Walker, 1979: Aerodynamic forces on a stationary and oscillating circular cylinder at high Reynolds numbers. Tech. Rep. TR T-300, NASA, Washington, D.C.

Justesen, P., 1991: A numerical study of oscillating flow around a cylinder. *J. Fluid Mech.*, **222**, 157–196.

Kang, D. and O. Fringer, 2012: Energetics of barotropic and baroclinic tides in the Monterey Bay area. *J. Phys. Oceanogr.*, **42**, 272–290.

Khatiwala, S., 2003: Generation of internal tides in an ocean of finite depth: Analytical and numerical calculations. *Deep-Sea Res. I*, **50**, 3–21.

Kim, Y.-J., S. D. Eckermann, and H.-Y. Chun, 2003: An overview of the past, present and future of gravity-wave drag parameterization for numerical climate and weather prediction models: Survey article. *Atmosphere-Ocean*, **41 (1)**, 65–98.

Klinger, B. A., 1994: Baroclinic eddy generation at a sharp corner in a rotating system. *J. Geophys. Res.*, **99 (C6)**, 12 515–12 531.

Klymak, J. M. and M. C. Gregg, 2001: Three-dimensional nature of flow near a sill. *J. Geophys. Res.*, **106 (C10)**, 22,295–22,311.

Klymak, J. M. and M. C. Gregg, 2003: The role of upstream waves and a downstream density pool in the growth of lee waves: Stratified flow over the Knight Inlet Sill. *J. Phys. Oceanogr.*, **33**, 1446–1461.

Klymak, J. M. and M. C. Gregg, 2004: Tidally generated turbulence over the knight inlet sill. *J. Phys. Oceanogr.*, **34**, 1135.

Kundu, P. K. and I. M. Cohen, 2004: *Fluid Mechanics*. 4th ed., Elsevier Academic Press, San Diego, CA, 759 pp.

Kunze, E., L. K. Rosenfeld, G. S. Carter, and M. C. Gregg, 2002: Internal waves in Monterey Submarine Canyon. *J. Phys. Oceanogr.*, **32**, 1890–1913.

Lamb, H., 1945: *Hydrodynamics*. 6th ed., Dover publications, New York.

Lavelle, J. W., H. O. Mofjeld, E. Lempriere-Doggett, G. A. Cannon, D. J. Pashinski, E. D. Cokelet, L. Lytle, and S. Gill, 1988: A multiply-connected channel model of tides and tidal currents in Puget Sound, Washington and a comparison with updated observations. Tech. Rep. ERL PMEL-84, NOAA Pacific Marine Environmental Laboratory, 103 pp., Seattle, Washington.

Legg, S. and K. M. H. Huijts, 2006: Preliminary simulations of internal waves and mixing generated by finite amplitude tidal flow over isolated topography. *Deep-Sea Res. II.*, **53**, 140–156.

Li, C., S. Armstrong, and D. Williams, 2006: Residual eddies in a tidal channel. *Estuaries and Coasts*, **29 (1)**, 147–158.

Llewellyn Smith, S. G. and W. R. Young, 2003: Tidal conversion at a very steep ridge. *J. Fluid Mech.*, **495**, 175–191.

Long, R. R., 1955: Some aspects of the flow of stratified fluids III. Continuous density gradients. *Tellus*, **7**, 341–357.

Lott, F. and M. J. Miller, 1997: A new subgrid-scale orographic drag parameterization: Its formulation and testing. *Q. J. R. Meteorol. Soc.*, **123**, 101–127.

Lowe, R. J., J. R. Koseff, and S. G. Monismith, 2005: Oscillatory flow through submerged canopies: 1. Velocity structure. *J. Geophys. Res.*, **110 (C10016)**, doi: 10.1029/2004JC002788.

MacCready, P. and G. Pawlak, 2001: Stratified flow along a rough slope: Separation drag and wave drag. *J. Phys. Oceanogr.*, **31**, 2824–2839.

MacCready, P., G. Pawlak, K. A. Edwards, and R. McCabe, 2003: Form drag on ocean flows. *Near-Boundary Processes and Their Parameterization: Proc. 13th 'Aha Huliko'a Hawaiian Winter Workshop*, Honolulu, HI, University of Hawaii at Manoa, 119–130.

Magaldi, M., T. Özgökmena, A. Griffa, E. Chassignet, M. Iskandarani, and H. Peters, 2008: Turbulent flow regimes behind a coastal cape in a stratified and rotating environment. *Ocean Modelling*, **25**, 65–82, doi:10.1016/j.ocemod.2008.06.006.

Marchesiello, P., J. C. McWilliams, and A. Shchepetkin, 2001: Open boundary conditions for long-term integration of regional oceanic models. *Ocean Modelling*, **3**, 1–20.

McCabe, R., P. MacCready, and G. Pawlak, 2006: Form drag due to flow separation at a headland. *J. Phys. Oceanogr.*, **36**, 2136–2152.

Morison, J. R., M. P. O'Brien, J. W. Johnson, and S. A. Schaaf, 1950: Ther force exerted by surface waves on piles. *Petrol. Trans., AIME*, **189**.

Moum, J. N., M. C. Gregg, R. C. Lien, and M. E. Carr, 1995: Comparison of turbulence kinetic energy dissipation rate estimates from two ocean microstructure profilers. *J. Atmos. Oceanic Technol.*, **12**, 346–366.

Moum, J. N. and J. D. Nash, 2000: Topographically induced drag and mixing at a small bank on the continental shelf. *J. Phys. Oceanogr.*, **30**, 2049–2054.

Moum, J. N. and J. D. Nash, 2008: Seafloor pressure measurements of nonlinear internal waves. *J. Phys. Oceanogr.*, **38**, 481–491.

Moum, J. N. and W. D. Smyth, 2006: The pressure disturbance of a nonlinear internal wave train. *J. Fluid Mech.*, **558**, 153–177, doi:10.1017/S0022112006000036.

Munk, W. H. and C. Wunsch, 1998: Abyssal Recipes II: Energetics of tidal and wind mixing. *Deep-Sea Res. I*, **45**, 1977–2010.

Nakamura, T., T. Awaji, T. Hatayama, K. Akitomo, and T. Takizawa, 2000: The generation of large-amplitude unsteady lee waves by subinertial K1 tidal flow: A possible vertical mixing mechanism in the Kuril Straits. *J. Phys. Oceanogr.*, **30**, 1601–1621.

Nash, J. D. and J. N. Moum, 2001: Internal hydraulic flows on the continental shelf: High drag states over a small bank. *J. Geophys. Res.*, **106 (C3)**, 4592–4612.

Nikurashin, M. and R. Ferrari, 2011: Global energy conversion rate from geostropic flows into internal lee waves in the deep ocean. *Geophys. Res. Lett.*, **38**.

Obasaju, E. D., P. W. Bearman, and J. M. R. Graham, 1988: A study of forces, circulation and vortex patterns around a circular cylinder in oscillating flow. *J. Fluid Mech.*, **196**, 467–494.

Officer, C. B., 1976: *Physical Oceanography of Estuaries (and Associated Coastal Waters)*. John Wiley & Sons, Inc., New York.

Oke, P. R., J. S. Allen, R. N. Miller, G. D. Egbert, and P. M. Kosro, 2002: Assimilation of surface velocity data into a primitive equation coastal ocean model. *J. Geophys. Res.*, **107 (C9)**, 3122–3147.

Pawlak, G. and P. MacCready, 2002: Oscillatory flow across an irregular boundary. *J. Geophys. Res.*, **107**, 4–1 to 4–7.

Pawlak, G., P. MacCready, K. A. Edwards, and R. McCabe, 2003: Observations on the evolution of tidal vorticiy at a stratified deep water headland. *Geophys. Res. Lett.*, **30 (24)**, 2234.

Pétrélis, F., S. G. Llewellyn Smith, and W. R. Young, 2006: Tidal conversion at a submarine ridge. *J. Phys. Oceanogr.*, **36**, 1053–1071.

Pingree, R. D. and L. Maddock, 1979: The tidal physics of headland flows and offshore tidal bank formation. *Marine Geology*, **32**, 269–289.

Polzin, K. L., J. M. Toole, J. R. Ledwell, and R. W. Schmitt, 1997: Spatial variability of turbulent mixing in the abyssal ocean. *Science*, **276 (5309)**, 93–96.

Rudnick, D. L., et al., 2003: From tides to mixing along the Hawaiian Ridge. *Science*, **301 (5631)**, 355–357.

Shchepetkin, A. F. and J. C. McWilliams, 2005: The Regional Oceanic Modeling System (ROMS): a split-explicit, free-surface, topography-following-coordinate oceanic model. *Ocean Modelling*, **9**, 347–404.

Signell, R. P. and W. R. Geyer, 1991: Transient eddy formation around headlands. *J. Geophys. Res.*, **96 (C2)**, 2561–2575.

St. Laurent, L., S. Stringer, C. Garrett, and D. Perrault-Joncas, 2003: The generation of internal tides at abrupt topography. *Deep-Sea Res. I*, **50**, 987–1003.

Stöber, U. and J. N. Moum, 2011: On the potential for automated realtime detection of nonlinear internal waves from seafloor pressure measurements. *Applied Ocean Res.*, **33 (4)**, 275 – 285.

Sutherland, D. A., P. MacCready, N. S. Banas, and L. F. Smedstad, 2011: A model study of the Salish Sea estuarine circulation. *J. Phys. Oceanogr.*, **41 (6)**, 1125–1143.

Thorpe, S. A., 1992: The generation of internal waves by flow over the rough topography of a continental slope. *Proceedings: Mathematical and Physical Sciences*, **439 (1905)**, 115–130.

Thorpe, S. A., 1996: The cross-slope transport of momentum by internal waves generated by alongshore currents over topography. *J. Phys. Oceanogr.*, **26**, 191–204.

Umlauf, L. and H. Burchard, 2003: A generic length-scale equation for geophysical turbulence models. *J. Mar. Res.*, **61**, 235–265.

Vallis, G. K., 2006: *Atmospheric and Oceanic Fluid Dynamics*. Cambridge University Press, Cambridge, U.K., 745 pp.

Vlasenko, V., N. Stashchuk, and K. Hutter, 2005: *Baroclinic tides: Theoretical modeling and observational evidence*. Cambridge University Press, New York.

Wang, C.-Y., 1968: On high-frequency oscillatory viscous flows. *J. Fluid Mech.*, **32**, 55–68.

Warner, S. J. and P. MacCready, 2009: Dissecting the pressure field in tidal flow past a headland: When is form drag "real"? *J. Phys. Oceanogr.*, **39 (11)**, 2971–2984.

Waterhouse, A. F., et al., 2012: Global patterns of mixing from direct and indirect measurements of dissipation. *submitted to Geophys. Res. Lett.*

White, L. and E. Wolanski, 2008: Flow separation and vertical motions ina tidal flow interacting with a shallow-water island. *Estuarine, Coastal and Shelf Science*, **77**, 457–466.

Wolanski, E., J. Imberger, and M. L. Heron, 1984: Island wakes in shallow coastal waters. *J. Geophys. Res.*, **89 (C6)**, 10 553–10 569.

Wood, N., A. R. Brown, and F. E. Hewer, 2001: Parameterizing the effects of orography on the boundary layer: An alternative to effective roughness lengths. *Q. J. R. Meteorol. Soc.*, **127**, 759–777.

Wunsch, C. and R. Ferrari, 2004: Vertical mixing, energy, and the general circulation of the oceans. *Annu. Rev. Fluid Mech.*, **36**, 281.

Wurtele, M. G., R. D. Sharman, and A. Datta, 1996: Atmospheric lee waves. *Annu. Rev. Fluid Mech.*, **28**, 429–476.

VITA

Sally J. Warner was born and grew up in New Jersey. She earned a bachelor's degree in Mechanical Engineering from McGill University in Montreal, Quebec, Canada in 2004. At the University of Washington in Seattle, she earned a MS in Physical Oceanography in 2008 and a MS in Applied Mathematics in 2010. In 2012, she earned a Doctor of Philosophy in Physical Oceanography.